

**Data assimilation for subsidence analysis of the Groningen region
A multi-scale study with importance sampling**

Kim, S.S.R.

DOI

[10.4233/uuid:610bb429-08c8-4870-8194-72b0ea1c7c97](https://doi.org/10.4233/uuid:610bb429-08c8-4870-8194-72b0ea1c7c97)

Publication date

2025

Document Version

Final published version

Citation (APA)

Kim, S. S. R. (2025). *Data assimilation for subsidence analysis of the Groningen region: A multi-scale study with importance sampling*. [Dissertation (TU Delft), Delft University of Technology].
<https://doi.org/10.4233/uuid:610bb429-08c8-4870-8194-72b0ea1c7c97>

Important note

To cite this publication, please use the final published version (if applicable).
Please check the document version above.

Copyright

Other than for strictly personal use, it is not permitted to download, forward or distribute the text or part of it, without the consent of the author(s) and/or copyright holder(s), unless the work is under an open content license such as Creative Commons.

Takedown policy

Please contact us and provide details if you believe this document breaches copyrights.
We will remove access to the work immediately and investigate your claim.

DATA ASSIMILATION FOR SUBSIDENCE ANALYSIS OF THE GRONINGEN REGION

A MULTI-SCALE STUDY WITH IMPORTANCE SAMPLING

DATA ASSIMILATION FOR SUBSIDENCE ANALYSIS OF THE GRONINGEN REGION

A MULTI-SCALE STUDY WITH IMPORTANCE SAMPLING

Dissertation

for the purpose of obtaining the degree of doctor
at Delft University of Technology,
by the authority of the Rector Magnificus Prof.dr.ir. T.H.J.J. van der Hagen,
chair of the Board for Doctorates,
to be defended publicly on
Monday, 3 March 2025 at 15:00 hours

by

Samantha Shirley Rachel KIM

Master of Science in Physics, Strasbourg University, France
Master of Science in Geosciences, Strasbourg University, France

This dissertation has been approved by the promotor:

Prof. dr. ir. F.C. Vossepoel
Prof. dr. ir. R.F. Hanssen

composition of the doctoral committee:

Rector Magnificus,	chairman
Prof. dr. ir. F.C. Vossepoel	Delft University of Technology, promotor
Prof. dr. ir. R.F. Hanssen	Delft University of Technology, promotor

Independent committee members:

Prof.dr. G. Evensen	NORCE, Norway
Prof. dr. P.J. Vardon	Delft University of Technology
Prof. dr. J.D. van Wees	Utrecht University/TNO
Dr. ir. M. Korff	Delft University of Technology/Deltares
Dr. ir. V.B.H. Ketelaar	NAM/Shell Exploration and Production B.V.
Dr. ir. E.C. Slob	Delft University of Technology, reservemember



Keywords: Subsidence, data assimilation, particle filter, subsidence estimation, InSAR, reservoir compaction, shallow subsurface
Printed by: Printerpro.nl.

Copyright © 2025 by S.S.R. Kim

ISBN 978-94-6518-022-9

An electronic version of this dissertation is available at
<http://repository.tudelft.nl/>.

À ma Mère,

*Suis le jour dans le ciel, suis l'ombre sur la terre ;
Dans les plaines de l'air vole avec l'aiglon ;
Avec le doux rayon de l'astre du mystère
Glisse à travers les bois dans l'ombre du vallon.*

Alphonse de Lamartine

CONTENTS

Summary	xi
Samenvatting	xv
Résumé	xvii
1 Introduction	1
1.1 Subsidence in the Groningen region	2
1.1.1 Deep-driven subsidence	4
1.1.2 Shallow-driven subsidence	5
1.1.3 Infrastructure and settlement	8
1.2 Subsidence estimation with geodetic techniques	8
1.2.1 Optical leveling	8
1.2.2 InSAR	9
1.2.3 Contextualization of the InSAR estimates	12
1.3 Modeling subsidence processes.	15
1.3.1 Subsidence caused by a compacting reservoir	15
1.3.2 Subsidence caused by soil motion	18
1.4 Data assimilation	23
1.4.1 Representing a physical process	24
1.4.2 Bayesian inference.	24
1.4.3 Importance sampling	25
1.5 Research objectives	28
2 Effect of spatially correlated subsidence signal in subsidence estimation with importance sampling	31
2.1 Introduction	33
2.2 Importance sampling method	35
2.2.1 Background on importance sampling	35
2.2.2 Weight collapse in the particle method.	36
2.3 Subsidence models	38
2.3.1 One-component model of subsidence	39
2.3.2 Multi-component model of subsidence	39
2.3.3 Synthetic experiments for subsidence models	40
2.4 Entropy and mutual information	41
2.5 Subsidence state estimation	45
2.5.1 Weight collapse and asymptotic limit for subsidence models	45
2.5.2 Entropy and mutual information for subsidence models.	48
2.5.3 Information content and efficiency	50

2.6	Discussion	52
2.7	Conclusion	54
3	Reducing weight collapse to assimilate geodetic datasets with importance sampling	55
3.1	Introduction	56
3.2	Standard particle filter	57
3.3	Proposal density in particle filter	58
3.3.1	Definition of a proposal density function	58
3.3.2	Optimal proposal applied in the subsidence problem	60
3.4	Verification on a compacting reservoir example.	62
3.4.1	Avoiding weight collapse with the optimal proposal	63
3.4.2	Testing the optimal proposal with Leveling	65
3.4.3	Testing the optimal proposal with InSAR.	68
3.5	Discussion	72
3.6	Conclusion	73
4	Multi-source subsidence estimation and forecasts using the particle filter method and InSAR	75
4.1	Introduction	76
4.2	Multi-sources subsidence model	77
4.3	InSAR dataset reduction for assimilation	80
4.4	Data assimilation methodology.	81
4.4.1	Importance sampling background	81
4.4.2	Assimilation of InSAR time series	82
4.4.3	Separation subsidence regimes	83
4.5	Proof of concept with synthetic experiments	86
4.5.1	Synthetic experiment set-up	86
4.5.2	Separation of deep- and shallow-driven subsidence	86
4.6	Application to the Groningen region with real geodetic datasets	90
4.6.1	Correlation of subsidence with soil water content	92
4.6.2	Correlation of subsidence with temperature	94
4.7	Discussion	96
4.8	Conclusions and recommendations	97
5	Conclusions and recommendations	99
5.1	Conclusions.	99
5.2	Recommendations for future research	101
5.2.1	On the use of importance sampling for the Groningen region	101
5.2.2	On alternative data assimilation methods	101
5.2.3	On the use of InSAR in data assimilation	102
5.2.4	On model refinement	102
5.3	Final thoughts	103

A	Supplement information for the posterior entropy calculation	105
B	Sensitivity tests for the entropy estimation	107
C	Supplement on the reservoir model geometry	109
D	Supplement on the InSAR dataset reduction	115
	Notation	117
	Curriculum Vitæ	133
	List of Publications	135

SUMMARY

The Groningen gas field has been compacting since the start of gas extraction in the 1960s because of pressure depletion in the reservoir, causing subsidence in the Groningen region. Geodetic techniques, such as optical leveling and satellite-borne Interferometric Synthetic Aperture Radar (InSAR), provide displacement estimates for subsidence monitoring. InSAR displacement estimates provide observation points with a higher spatial density and temporal sampling than leveling. Whereas identifying leveling benchmarks with subsidence caused by the compaction reservoir is possible, the InSAR's sensitivity to multiple subsidence sources (e.g., compacting reservoir, soil motion, and infrastructure instability) complicates the identification of subsidence-driving mechanisms in InSAR estimates. Combining physics-based subsurface models with InSAR estimates into data assimilation is an approach to estimating to what extent reservoir compaction and other subsurface processes contribute to the total subsidence.

In data assimilation, we consider the uncertainty in data and physical models to combine information and to find the most likely estimate of the model variables and their probability distributions. Whereas most data assimilation methods approximate the probability density function (PDF) of the model state and the observations with a Gaussian PDF and assume that the observed quantity is linearly dependent on the model quantity (i.e., linear observation operator), the importance sampling method I use in this thesis does not require these assumptions. This makes importance sampling a straightforward application of Bayes' theorem, but its application to systems with many observations is rarely explored because of its computational cost.

A core component of this study is to efficiently implement importance sampling for the Groningen region. In the importance sampling method, Monte Carlo simulations provide forward model realizations of subsidence. This ensemble of forward model realizations provides a prior distribution for the vertical displacement at a given location and time. Model realizations of subsidence are compared to geodetic estimates thereof and weighted according to the difference between the model and the geodetic estimates using Bayes' theorem. The weight of each forward model realization can be seen as a measure of its relative "importance" in correctly representing the modeled property (in this case, vertical displacement), hence the name "importance sampling". The ensemble of weighted model realizations provides the posterior PDF, and the weighted mean of this distribution is the resulting data assimilation analysis.

In the Groningen region, the observed subsidence field exhibits a typical subsidence bowl, which is spatially smooth at the scale of the Groningen region because the subsidence at one location is a function of the compaction of all other locations in the reservoir. Although the resulting subsidence field is smooth, it will also be spatially heterogeneous in the case of spatial variation in the reservoir properties and in the soil layers. Data assimilation experiments in which we take into account the expected spatial

correlation of the subsidence signal (resulting in varying smoothness in the observed field), demonstrate that more model realizations are necessary to obtain a meaningful PDF of the entire reservoir's compaction in the case of a spatially smooth observed field than without spatial correlation. I also evaluate the necessary number of model realizations for a given number of assimilated observation points on a compacting reservoir example. These experiments illustrate that two complicating factors must be considered when using the importance sampling method for subsidence estimation: the method requires an increasing number of model simulations when 1) subsidence at one location is a function of reservoir compaction in the entire reservoir, resulting in a smooth, or spatially correlated signal when 2) the number of model realizations is too little compared to the number of assimilated observations.

I propose an approach based on information theory to estimate the required number of model realizations in the case of spatial correlation for effective subsidence estimation with importance sampling. I show in synthetic tests with a reservoir model, and cumulative displacements simulated at a given time for 50 observation points that a minimum number of model realizations of 10^{13} is required to provide a similar performance of the data assimilation as in a model without spatial correlation and 10000 model realizations. While sampling 10000 model realizations is feasible in practical applications of importance sampling, using 10^{13} model realizations is impossible with our computational capacity. The number of model realizations required to deal with the contemporary number of geodetic observations and the smooth observed signal is currently impossible regarding computational cost.

To deal with the contemporary size of geodetic datasets and spatial correlation while limiting the number of model realizations, we use a specific implementation of importance sampling with a so-called *optimal proposal* for generating the prior distribution. We evaluate the optimal proposal importance sampling performance in the Groningen region with leveling and InSAR datasets. We find that the optimal proposal importance sampling with 1032 spatially Point Scatterers (PSs) sub-sampled randomly from the total number of PSs over a region of 50×50 km, can effectively estimate reservoir compaction associated with subsidence for 1000 model realizations, which is feasible with the computational capacity of most computers.

As a next step, we investigate how the optimal proposal importance sampling can be applied to identify *multiple* subsidence-driving mechanisms. We use a dynamical model involving deep and shallow subsidence drivers: reservoir compaction in the deep subsurface and soil response to precipitation and evaporation in the shallow subsurface. In this case study for subsidence caused by multiple subsurface mechanisms, we assimilate vertical cumulative displacements in the InSAR time series into this dynamical model. We obtain the data assimilation analysis of subsidence and identify long-term subsidence with variations over multiple years and shorter-term seasonal variations. We also demonstrate the method's forecasting skill for subsidence. Not unexpectedly, the model error, primarily due to an incomplete representation of the shallow subsurface processes in models, strongly influences the accuracy of the data-assimilation estimate of the seasonal variation in subsidence forecasts.

Overall, this research presents an implementation of importance sampling to assimilate leveling and InSAR datasets. On the scale of the Groningen gas field, the

optimal proposal importance sampling is effective in assimilating leveling datasets, with approximately 500 benchmarks, but its applicability to the assimilation of a full InSAR dataset with one million PSs requires further methodological development. With sufficient prior information on the subsurface processes, the optimal proposal importance sampling could theoretically serve as a basis for assimilating geodetic estimates into physics-based subsidence models to identify multiple subsidence-driving mechanisms. However, identifying multiple subsidence-driving mechanisms would require observations specific to the signals of interest, such as extensometer data for the shallow-driven subsidence and physical models with a more complete description of the processes in the various layers of the subsurface.

SAMENVATTING

De regio Groningen ervaart bodemdaling als gevolg van gaswinning vanaf de jaren 1960, waardoor van het gesteente in het gasreservoir op ongeveer drie kilometer diepte compacteert. Geodesie is een gebied van de geowetenschappen dat zich richt op de studie van de geometrie van het aardoppervlak. Geodetische technieken, zoals waterpassen en Interferometrische Synthetische Apertuur Radar (InSAR), maken het mogelijk om bodemdaling te schatten en te monitoren. De fysische mechanismen die eraan ten grondslag liggen, met name in hoeverre andere mechanismen dan reservoircompactie bijdragen aan de totale bodemdaling, zijn hier echter niet direct uit af te leiden. Door gebruik te maken van data-assimilatie, een techniek die ook wordt gebruikt om bijvoorbeeld het weer te voorspellen, is het mogelijk om de bodemdalingsschatting verkregen uit metingen te combineren met bodemdaling berekend met fysische modellen. Op deze manier wordt alle beschikbare informatie samengebracht om zowel de bodemdalingsschatting als ook de schatting van de oorzakelijke mechanismen te verbeteren en een bodemdalingsvoorspelling af te leiden.

Een kernonderdeel van deze studie is het efficiënt implementeren van importance sampling voor de regio Groningen. We gebruiken een data-assimilatiemethode op basis van importance sampling om grote hoeveelheden gegevens voor de regio Groningen efficiënt te assimileren. De importance sampling-methode is een data-assimilatiemethode waarbij simulaties van een voorwaarts model realisaties van bodemdalingsschattingen genereren om “a priori” waarden te creëren die de werkelijke bodemdaling benaderen. De gesimuleerde verzakkingswaarden worden vergeleken met geodetische verzakkings-schattingen en gewogen overeenkomstig het verschil tussen model en geodetische schattingen. Het gewicht dat aan elke modelsimulatie wordt toegekend is evenredig aan het vermogen van het model om de bodemdaling correct te simuleren. Importance sampling is een eenvoudige methode, met een minimaal aantal aannames die het theoretisch mogelijk maakt om de kansdichtheidsfunctie van alle simulaties nauwkeurig te bepalen.

Experimenten met data-assimilatie waarbij we rekening houden met de verwachte ruimtelijke correlatie van het bodemdalingssignaal (wat resulteert in een variërende gladheid in het waargenomen veld) laten zien dat er meer modelrealisaties nodig zijn om een zinvolle PDF van de verdichting van het gehele reservoir te verkrijgen in het geval van een ruimtelijk glad waargenomen veld dan zonder ruimtelijke correlatie. Ik demonstreer ook het benodigde aantal modelrealisaties voor een gegeven aantal geassimileerde waarnemingen op een verdichtend reservoirvoorbeeld. Deze experimenten illustreren dat er met twee complicerende factoren rekening moet worden gehouden bij het gebruik van de belangrijkheids-samplingmethode voor het schatten van de bodemdaling: de methode vereist een toenemend aantal modelsimulaties wanneer 1) de bodemdaling op één locatie een functie is van de verdichting van het reservoir in het hele reservoir, wat resulteert in een glad of ruimtelijk gecorreleerd signaal wanneer 2) het aantal

geassimileerde observatiepunten groter is dan de dimensie van het schattingsprobleem.

Om de modelrealisaties van beperkte grootte te behouden terwijl een groot aantal gegevens wordt geassimileerd in de aanwezigheid van ruimtelijke correlaties, kiezen we voor een aangepaste implementatie van belangrijkheidssampling met een zogenaamd optimaal voorstel. Hiermee tonen we aan dat het met optimale proposal importance sampling is om nivelleringsdatasets en een maximum aantal van 1032 PS-InSAR-punten over bodemdaling te assimileren met minder dan 1000 modelrealisaties.

We onderzoeken de toepassing van optimale voorstel-belangrijkheidssampling om de mechanismen die bodemdaling veroorzaken te identificeren en te kwantificeren. We nemen aan dat bodemdaling samenhangt met de “diepe” ondergrond (op reservoirniveau op drie km diepte) en de “ondiepe” ondergrond, meestal sedimentaire lagen zoals zand, klei en veen. Onze benadering maakt het mogelijk om de temporele evolutie van de bodemdaling te schatten. Door onze implementatie van optimal proposal importance sampling slagen we erin om seizoensgebonden variaties van de oppervlaktelagen van de bodem te bepalen, die in de winter uitzetten en in de zomer verdichten, afhankelijk van de bodemvochtigheid en temperatuur. Dit maakt het mogelijk om op basis van de combinatie van InSAR en meteorologische gegevens toekomstige bodemdaling correct te voorspellen, met of zonder seizoensvariatie.

De ontwikkeling van onze importance sampling methode voor de regio Groningen kan beschouwd worden als een stap voorwaarts in het gebruik van significantiebemonstering voor het schatten van bodemdaling, die waardevol kan zijn voor het schatten en beperken van bodemdaling door gebruik van de ondergrond.

RÉSUMÉ

La région de Groningue, aux Pays-Bas, subit un affaissement de la surface du sol, appelé subsidence due à l'extraction de gas naturel. L'exploitation du réservoir de gas de Groningue débuta dans les années 1960, et depuis a eu pour effet de compacter la roche au niveau du réservoir de gas, qui se situe à environ 3 km de profondeur. La compaction du réservoir agit telle un "ballon" réduisant de volume et crée proportionnellement un déplacement de la surface du sol; de la subsidence. La géodésie est un domaine des géosciences destiné à l'étude de la surface terrestre. Les techniques de géodesie, telles que le niveau optique et les techniques satellitales InSAR (Interferometric Synthetic Aperture Radar), permettent d'estimer et de monitorer la subsidence. Bien que ces méthodes permettent d'estimer la subsidence avec une précision de l'ordre du millimètre, elles ne permettent pas de déterminer les mécanismes physiques à son origine. Plus particulièrement d'estimer dans quelle mesure des mécanismes, autre que la compaction du réservoir, pourraient contribuer à la subsidence totale, observée en surface.

En utilisant l'assimilation de données, qui est une technique utilisée par exemple, pour estimer et prévoir la météo, il est possible d'estimer la subsidence à partir d'une comparaison entre 1) de déplacement de la surface du sol, obtenu via les techniques de géodésie et 2) la subsidence calculée via les modèles physiques. De cette manière, toute l'information disponible est combinée afin d'améliorer l'estimation de la subsidence, de ses mécanismes contributifs et d'en dériver une prévision temporelle.

Dans cette thèse de doctorat, nous utilisons une technique d'assimilation de données, basée sur la notion d'échantillonnage préférentiel. La méthode d'échantillonnage préférentiel est une approche probabilistique de l'assimilation de données, dans laquelle les simulations d'un modèle physique permettent de générer un échantillon de valeurs de subsidence. Cet échantillon permet de créer un ensemble de valeurs "à priori", qui approximent de manière statistique la subsidence réelle. Ces modèles simulés de subsidence sont comparés aux estimations géodésiques de subsidence et pondérés en fonction de la différence entre le modèle et les estimations géodésiques. Le poids attribué à chaque simulation de modèle est proportionnelle à la capacité du modèle à simuler correctement la subsidence réelle. L'échantillonnage préférentiel est une méthode avec un minimum d'approximations permettant, contrairement à la plupart des méthodes d'assimilation de données, de déterminer exactement la fonction de vraisemblance de l'ensemble des simulations.

Cependant, deux éléments rentrent en compte lors de l'estimation de la subsidence avec la méthode d'échantillonnage préférentiel. Premièrement, les techniques géodésiques produisent un très grand nombre de données, ce qui est difficilement assimilable avec les algorithmes actuels sans augmenter le nombre de simulations (i.e., taille de l'ensemble) de manière exponentielle. En plus de cela, la taille de l'ensemble augmente encore plus rapidement quand la subsidence est spatialement corrélée.

C'est-à-dire, quand la subsidence à un endroit est causée par la compaction du réservoir aux autres endroits du sous-sol. Ces deux facteurs influent fortement sur la taille de l'ensemble, qui en augmentant requière davantage de puissance de calcul, ce qui n'est pas toujours accessible.

En utilisant des données simulées, nous montrons dans cette étude quelle taille d'ensemble permet d'estimer efficacement la subsidence. Pour conserver un ensemble de taille limité tout en assimilant un grand nombre de données, particulièrement en présence de corrélation spatiales, nous optons pour une implémentation modifiée de l'échantillonnage préférentiel avec une "densité biaisée optimale". En utilisant certains concepts de la théorie de l'information (développée notamment durant la seconde guerre mondiale pour décrypter les messages secrets), nous parvenons à maximiser le contenu informatif des données assimilées en fonction du nombre de données sélectionnées pour l'assimilation. Ainsi, nous démontrons qu'il est possible d'assimiler jusqu'à 1032 données InSAR de subsidence avec une taille d'ensemble réduite à 1000, ce qui permet à présent l'utilisation des données InSAR dans une méthode d'échantillonnage préférentiel, spécifiquement dans la région de Groningue.

Pour aller plus loin dans l'application de l'échantillonnage préférentiel à densité optimale, nous explorons son potentiel à identifier et à quantifier les mécanismes induisant la subsidence. Dans notre cas, les mécanismes du sous-sol causant la subsidence se situent 1) au niveau du réservoir à 3 km de profondeur et 2) proche de la surface, typiquement au niveau des couches sédimentaires telles que sables, argiles et tourbes. En appliquant notre implémentation de l'échantillonnage préférentiel à densité optimale, nous parvenons à estimer les variations saisonnières des couches superficielles du sol, qui expandent en hiver et se compactent en été, ceci en fonction de l'humidité du sol. De plus, en utilisant cette méthode avec des données InSAR et météorologiques, nous démontrons qu'il est possible de prévoir correctement les variations saisonnières du sol.

Pour finir, cette étude de recherche présente une implémentation de l'échantillonnage préférentiel pour l'assimilation de données géodésiques, plus particulièrement InSAR, permettant d'étendre l'application de l'échantillonnage préférentiel à la région de Groningue. L'échantillonnage préférentiel à densité biaisée optimale ainsi développé pourra dans de futures recherches s'appliquer à des modèles physiques de plus haute complexité pour comprendre comment d'autres mécanismes, davantage complexes et non inclus dans cette étude, induisent de la subsidence. Ainsi, cette approche pourrait compléter des techniques géodésiques pour monitorer, et mitiger les effets de l'exploitation du sous-sol.

1

INTRODUCTION

Ambition, to me, has always seemed preferable to memories.

Gaston Rébuffat

The Groningen gas field is a large onshore gas reservoir in the northeastern part of the Netherlands, approximately 30 kilometers in diameter at a 3-kilometer depth. The reservoir is mainly composed of a semi-consolidated sandstone rock matrix and has been compacting since the start of production in the 1960s because of the pressure reduction. The reservoir compaction at several kilometers depth causes subsidence at the Earth's surface. Subsidence forecasts and monitoring techniques have been developed to prevent environmental, societal, and economic risks associated with hydrocarbon production. Measuring and modeling subsidence provide a better understanding of the processes causing subsidence above the Groningen gas field and help evaluate the subsidence effect of hydrocarbon production.

1.1. SUBSIDENCE IN THE GRONINGEN REGION

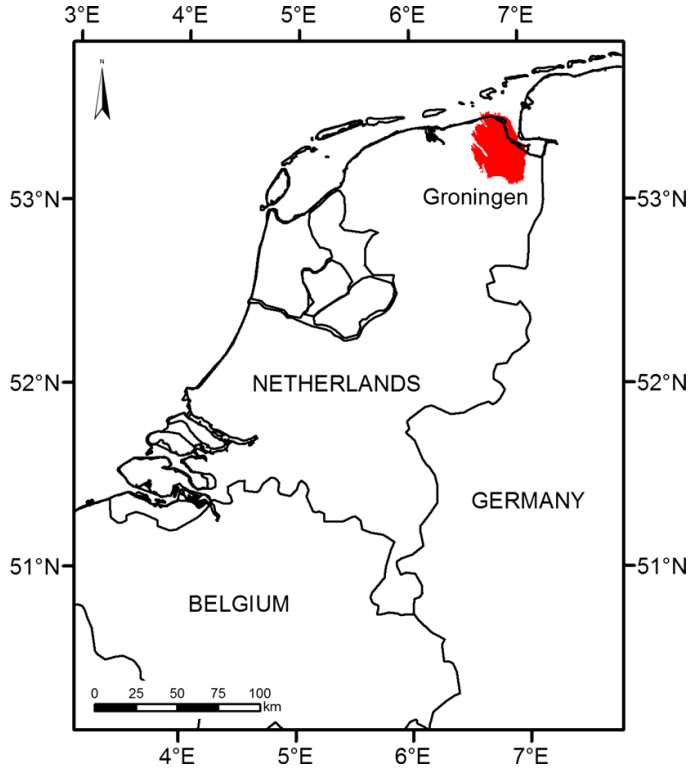


Figure 1.1: Geographical map of the Netherlands showing the location of the Groningen gas field in a red-shaded area (Kruiver et al., 2017).

THE Groningen gas field was discovered in 1959 and is located in the northern part of the Netherlands (Fig. 1.1). With approximately 30 km diameter, it is one of the largest onshore gas reservoirs in Europe. The reservoir is situated at a depth between 2750 to 2900 m with a varying thickness of 100 to 200 m from south to north. The reservoir layers are composed of the Rotliegend sandstone, which has a semi-consolidated rock matrix with a porosity between 15 to 20% (Geertsma, 1973; Hettema et al., 2000).

Gas production provided the primary source of Dutch energy and an alternative to coal mining. Because gas production causes pressure depletion in the reservoir, subsidence above the Groningen gas field occurs. Whereas subsidence model prognosis estimated an average displacement velocity of 10 mm/year in the center of the gas field in 2025 relative to the start of production (Gussinklo et al., 2001), the measurement registry of 2018 revealed a maximal displacement velocity of 0.6 mm/year (NAM, 2020). The legal obligation of the producer to monitor subsidence has led to the deployment of a leveling monitoring network over the Groningen gas field since the 1960s (Mijnbouwwet, 2003). Subsidence monitoring is essential for safety (infrastructure integrity) and environmental impact assessment. A recent subsidence prognosis, performed in

Prognose voor 2080

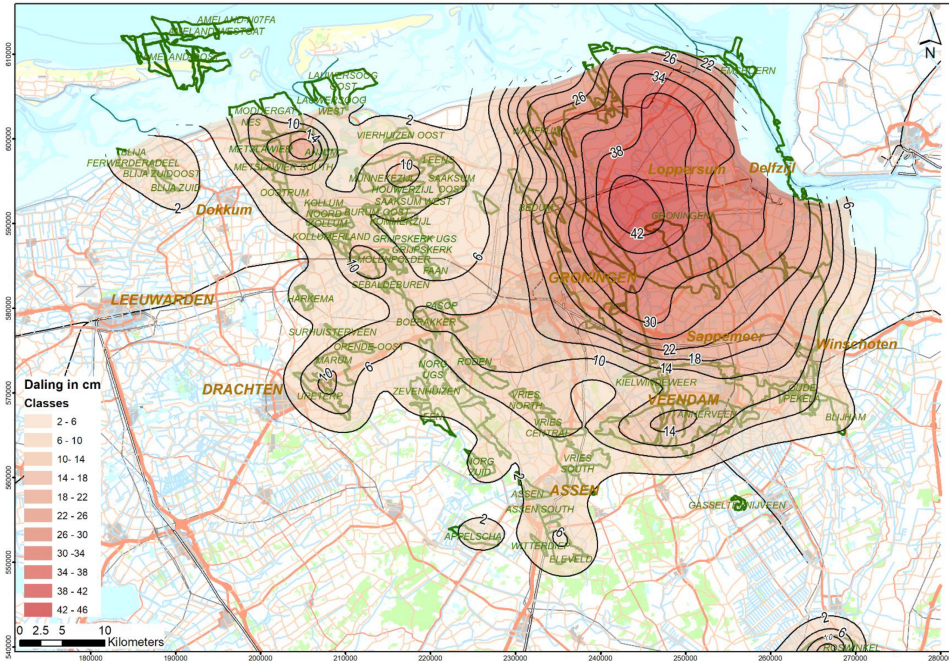


Figure 1.2: Modeled subsidence over the Groningen region showing a subsidence prognosis for 2080 with cumulative displacement in the center of the subsidence bowl of 42 cm relative to the start of production. (NAM, 2020)

2020 by the producer Nederlandse Aardolie Maatschappij (NAM), shows a cumulative displacement in 2080 relative to the start of the production (Fig. 1.2). The expected maximal subsidence above the Groningen gas field in 2080 is about 42 cm. Additionally to subsidence models, the development of InSAR (Interferometric Synthetic-Aperture Radar) provides a monitoring technique to estimate surface displacement with a higher spatial and temporal density of observation points compared to the leveling technique (Bierman et al., 2015; Ketelaar, 2009; van Elk et al., 2021; van Elk et al., 2022).

In 2012, due to a significant earthquake close to the town of Huizinge, a new risk assessment on induced seismicity and subsidence was made, and in 2014, the production was reduced to prevent risks (NAM, 2016). Induced seismicity and subsidence impact the population of the Groningen region in both the material and the psychological aspects (Hupkes et al., 2021). To prevent the downward effect of the subsurface exploitation and to better understand the subsurface in the Groningen region, many studies have been conducted on both induced seismicity (Bourne et al., 2014; Candela et al., 2019; Hettema et al., 2000; Smith et al., 2019) and on subsidence (Fokker et al., 2012; Hanssen, 2015; Kroon et al., 2009).

The compacting reservoir is the first cause of subsidence above the Groningen gas field. In this thesis, deep-driven subsidence can be attributed to compaction at the reservoir depth, but the total observed subsidence can have different interpretations

(Fokker et al., 2019; Ketelaar, 2009; Kroon et al., 2009). Shallow-driven subsidence is defined as the consequence of multiple processes occurring at a depth from 0 to 20 m (Mijnbouwwet, 2003). This section introduces the driving mechanisms of subsidence in the Groningen region.

1.1.1. DEEP-DRIVEN SUBSIDENCE

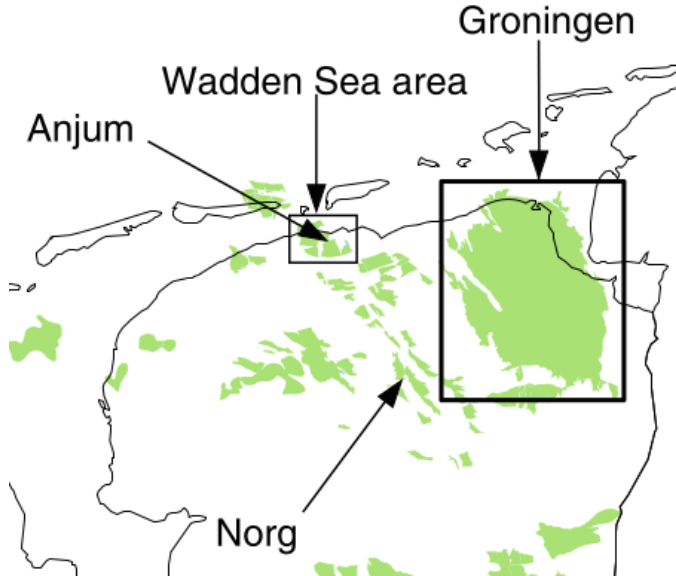


Figure 1.3: Map of the north of the Netherlands showing the producing gas fields (green areas) and illustrating the spatial extent of the Groningen gas field compared to the surrounding small gas fields.

During gas and oil production, the pore pressure in the reservoir rock decreases. This pore pressure reduction creates a stress increase, resulting in reservoir compaction. Consequently, the reservoir compaction occurring at approximately 2900 m creates subsidence at the Earth's surface, above the reservoir field indicated in green in Fig. 1.3. This subsidence field has a large extent over the entire Groningen area with a characteristic bowl-shaped subsidence profile since the start of production (Fig. 1.1(right) and Fig. 1.4). In comparison to small gas fields, for example, the Anjum gas field in the Wadden Sea area, which has a spatial extent less than 10 km, the compaction of the Groningen gas field has an effect on a very large part of the North of the Netherlands (Fig. 1.2 and Fig. 1.4).

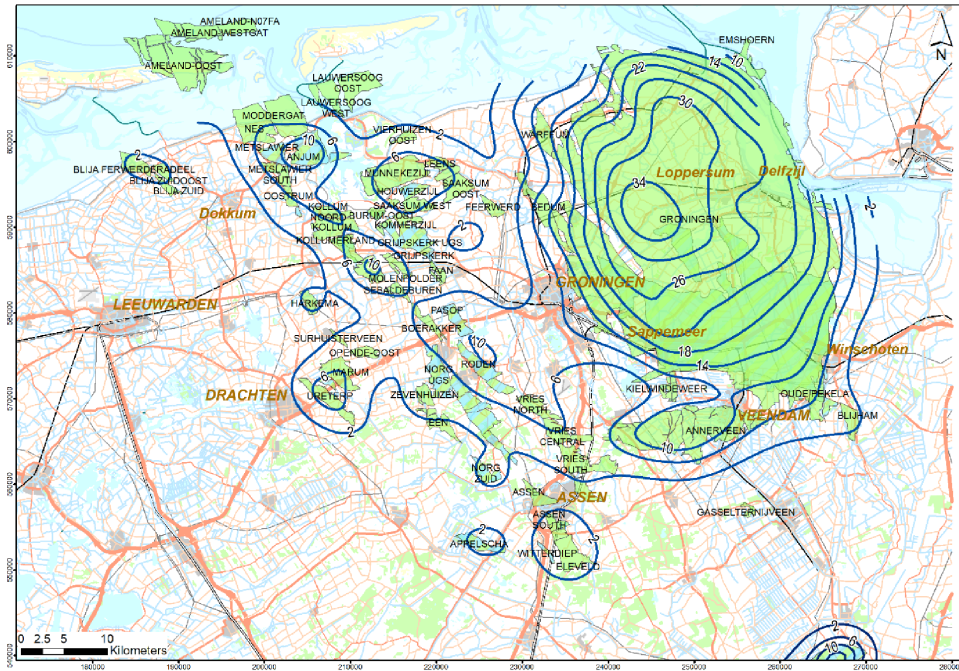


Figure 1.4: Displacement contour map of the north of the Netherlands from leveling the campaign of 1818, showing a cumulative displacement in 2018 relative to 1964. Subsidence is shown in cm. (NAM, 2020.)

1.1.2. SHALLOW-DRIVEN SUBSIDENCE

In addition to the deep-driven subsidence from the reservoir compaction, subsidence can arise from other processes shallower than the reservoir layer (Kroon et al., 2009). For example, other regions in the Netherlands have a subsidence rate of up to 10 mm/year caused by compaction of shallow layers, such as peat soil (Conroy et al., 2022; Fokker et al., 2016; Koster et al., 2018; van Asselen et al., 2018).

The first 20 m of the Dutch subsurface is characterized by a succession of sediment deposits varying with the geological Era (Fig. 1.5). The Pleistocene layer (2.58 - 0.0117 Ma ago) corresponds to deposits at approximately 20 m depth and is assumed to move with the reservoir overburden because deposits are settled and are thus not compacting. Layers above the Pleistocene correspond to the Holocene (11.7 - 0 ka ago) and have different deposit compositions, e.g., sediments, clay, and peat. Figure 1.5 shows the different compositions of the Pleistocene layer over the Netherlands. The Groningen region shows in the north an eroded Pleistocene layer due to marine systems along the coast (red areas in Fig. 1.5), the superposition of the Pleistocene layer and Holocene layers (green areas) and in the south, at the ground level Pleistocene sediments (yellow areas). The Holocene layers above the Groningen region correspond approximately to the 15 first meters (Bruna, 2020), with varying thicknesses over the region. Compaction in the Holocene layers causes what we refer to as “shallow subsidence”. Shallow geology for the Holocene layers (above the Pleistocene layer previously described) is

Top Pleistocene in the Netherlands (m, NAP)

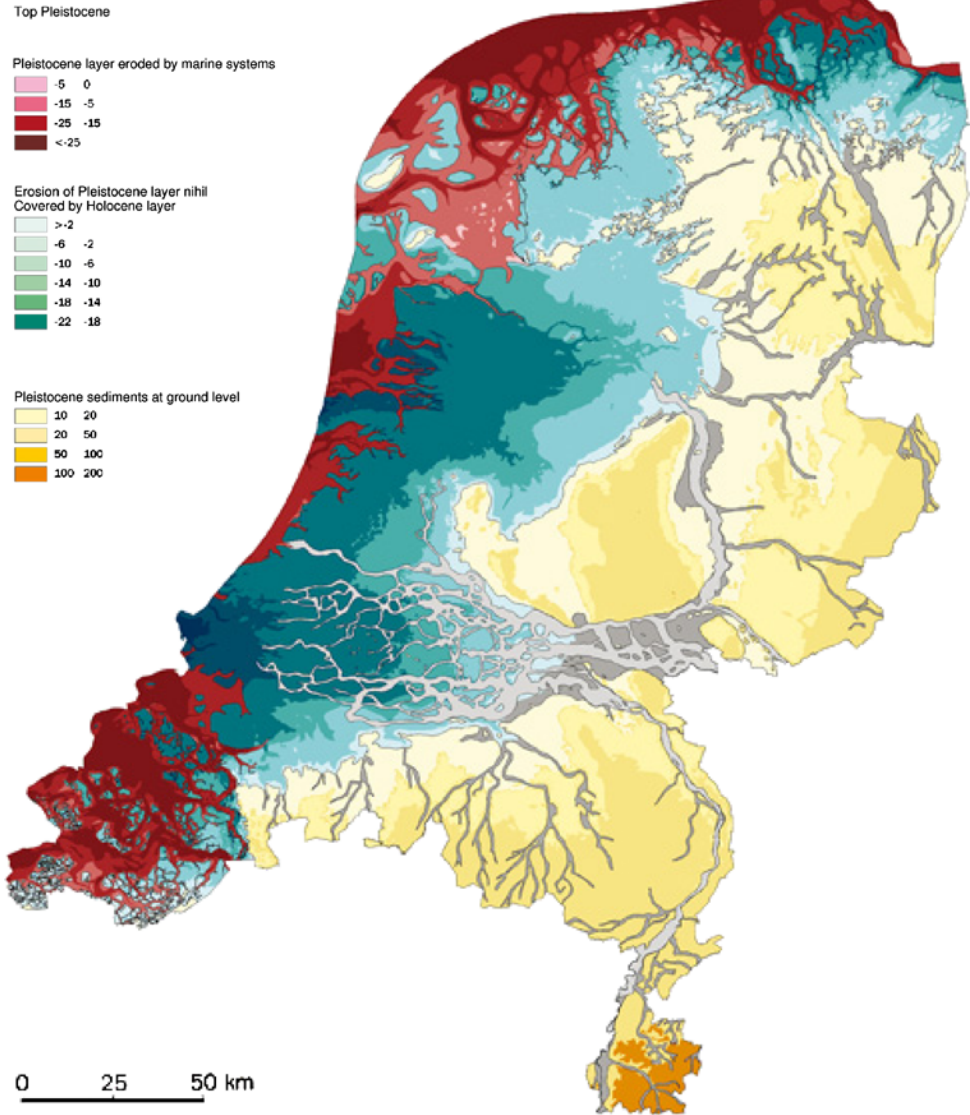


Figure 1.5: Geological map of the Netherlands showing the composition of the Pleistocene layer at different depths, indicated in the vertical datum Normaal Amsterdams Peil (Normal Amsterdam level) (NAP). The Pleistocene layer is composed of settled materials and is assumed to move proportionally to the reservoir compaction. Eroded Pleistocene layers are shown in red, a Pleistocene layer covered by the Holocene layer in green, and Pleistocene sediments at ground level in yellow, i.e., NAP > 0 m (DINO, 2008.). The Groningen region has the particularity to have these three kinds of geology.

approximated in this thesis with three soil types: clay, peat, and sand (Fig. 1.6). The thickness of clay soils in the north can vary due to the shrinkage of clay particles (Fig. 1.6 in green). Peat soils are susceptible to peat oxidation, which also creates thickness reduction of the Holocene layers containing peat (Fig. 1.6 in red). In sand areas in the south (Fig. 1.6 in yellow), sediments are assumed to be already settled (i.e., older layers with high deposit stiffness), and consequently, we do not expect shallow compaction in sand areas (Ketelaar, 2009). Compaction, oxidation, and consolidation in the shallow subsurface are processes that cause subsidence (Deltares, 2018):

- Compaction or compression refers to changes in the thickness of the soil layer changes caused by a pore pressure change, usually in response to external factors such as the load of new infrastructures and soil water content. Compaction can be positive or negative. A negative compaction refers to an expansion called soil swelling (Fokker et al., 2019).
- Consolidation is a temporal compaction process development driven by a pore pressure change in saturated soils.
- Oxidation occurs in peat layers as a biochemical process caused by soil exposure to oxygen. Oxidation is an irreversible phenomenon accelerated by anthropogenic factors, e.g., agriculture, in some regions of the Netherlands.

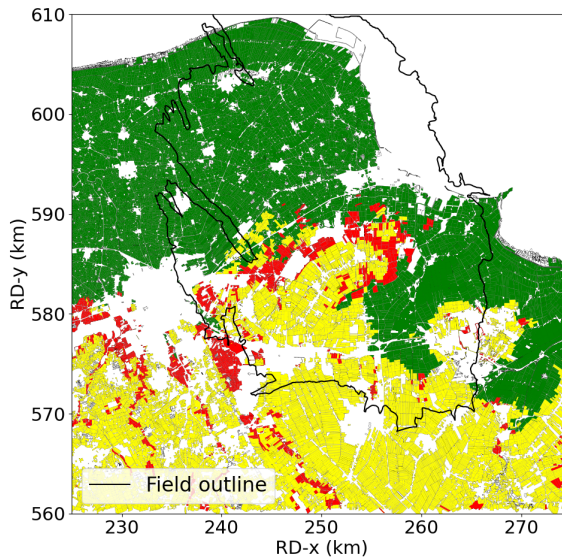


Figure 1.6: Map of the Groningen region showing a simplification of the geology of the first 1.20 meter below the surface. Soil types are attributed per parcel based on the soil map of the Netherlands (Bodemkaart van Nederland, schaal 1:50.000). The outline of the Groningen gas field is indicated with a black solid line, and the soil type per parcel is composed of clay in the north (green), sand in the south (yellow), and peat (red). Geographic coordinates are indicated in the Rijksdriehoek system.

These processes cause long-term and seasonal subsidence because of a change in pore pressure, which varies with water content and temperature. Extrapolating the behavior of soil displacement observed in other areas in the Netherlands (Conroy et al., 2022; van Asselen et al., 2018) to the Groningen region, we can expect, particularly in peat soil, upward soil motion in winter and subsidence in summer because of variation in the soil water content. We also expect shallow-driven subsidence to have higher spatial heterogeneity than deep-driven subsidence because of the spatial heterogeneity of the shallow-layer composition. This spatial heterogeneity causes the subsidence signal's relatively short spatial correlation scales.

1.1.3. INFRASTRUCTURE AND SETTLEMENT

Soil settlement and geotechnical instability are caused by the load of structures, such as buildings, roads, dikes, and building foundations, which can be positioned on a more or less stable subsurface layer (Fig. 1.12). Buildings with deep foundations in the Pleistocene layer are assumed stable, whereas shallow-founded infrastructures can experience subsidence due to shallow compaction. When measuring surface displacement with the InSAR technique, infrastructure expansion due to temperature change must be considered in addition to subsidence. Thermal variability in infrastructure materials causes a signal of several millimeters in InSAR vertical displacement estimate and has a seasonal variation (Bruna, 2020; Hanssen, 2015). We discuss this effect and give details in the following sections.

1.2. SUBSIDENCE ESTIMATION WITH GEODETIC TECHNIQUES

SINCE 1960, leveling campaigns have been performed to monitor subsidence above the Groningen gas field and, more recently, the InSAR technique provides displacement estimates (Hanssen, 2015; Ketelaar, 2009). The two methods provide different spatial and temporal resolutions of subsidence observations with signals of varying complexity in time and space. The following provides an overview of the leveling and the InSAR techniques.

1.2.1. OPTICAL LEVELING

The leveling network deployed above the Groningen region consists of more than 500 deep-founded benchmarks and is used for subsidence monitoring. Figure 1.7 shows the leveling network in the Groningen region and contour lines of cumulative displacement in 2003 relative to the start of the production in 1964, highlighting the bowl-shaped subsidence field caused by the compacting Groningen reservoir. Leveling benchmarks usually consist of metal pieces anchored on buildings, and measurement at their location provides displacement estimates, in this case, height differences relative to a station of reference at a specific epoch. Benchmarks located on deep-founded infrastructures provide displacement estimates assumed sensitive to deep-driven subsidence (Ketelaar, 2009). These benchmarks are typically on buildings with foundations in the Pleistocene layer (Fig. 1.5), assumed to be stable and to move because of reservoir compaction if an underlying reservoir is present. Posterior analysis of leveling data is necessary to remove outliers since leveling benchmarks

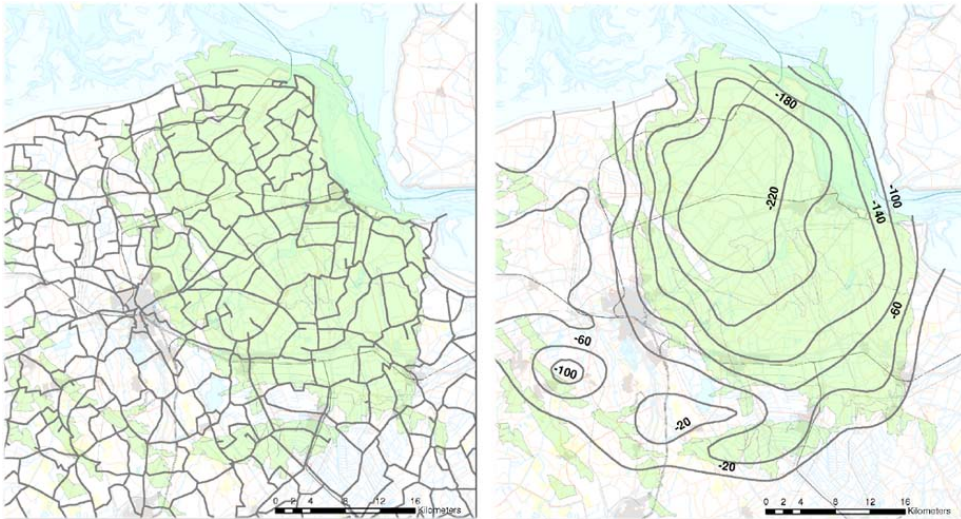


Figure 1.7: Map of the Groningen region showing (left) the leveling network and (right) the associated cumulative subsidence in millimeters in 2003 relative to the start of the production in 1964. Contour lines show the subsidence bowl caused by the compacting reservoir above the Groningen gas field and the surrounding small gas fields (green shaded area) (Ketelaar, 2009).

are sensitive to the deep-driven subsidence but also to other cause of motion. For example, leveling benchmarks can move because of building motions (e.g., sinking onto the ground because of their own weight), the compaction of the shallow subsurface, or the necessity to move the benchmark (e.g., work or renovation around the benchmark location). A space-time analysis of the leveling time series allows determining, considering uncertainties, which leveling benchmark are representative of the deep-driven subsidence. Then, they are classified in three categories 1) stable (“stabiël”), 2) partly stable (“deels stabiël”) and 3) not stable (“niet stabiël”). The stable leveling benchmark are assumed only sensitive to the deep-driven subsidence. The stability analysis is out of the scope for this thesis, and further details can be found in NAM, 2019.

1.2.2. INSAR

InSAR provides a high spatial coverage of Point Scatterer (PS) with higher spatial density than the leveling displacement estimates (Fig. 1.9). The principle of InSAR is based on the reflection of an electromagnetic wave on reflective surfaces on the Earth’s surface, such as buildings and roads. Figure 1.10 illustrates the principle of InSAR: a first satellite passing above the Earth sends a first electromagnetic wave and records the signal of this electromagnetic wave reflected on a surface. The same process is repeated when a second satellite passes at the same location. Based on the principle of optical interferometry (Bruhat and Kastler, 1965; Kampes, 2006), using the time difference in the reception of the signal with the first satellite and the second satellite, we can infer a distance difference in the travel of the electromagnetic waves in the acquisition of the

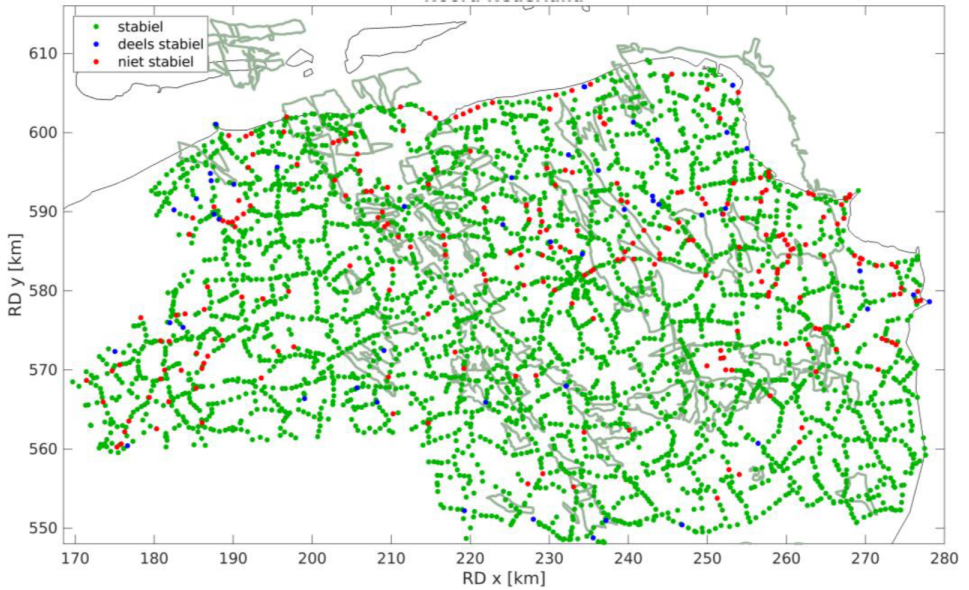


Figure 1.8: Leveling network for the measurement registry of the North Netherlands 2019, showing a re-actualization of the stability of the leveling benchmarks. Benchmark classified as “stable” are indicated in green and represent 93 % of the total number of benchmarks (NAM, 2019, 2020.)

first satellite and the second satellite. InSAR estimates are based on measuring this signal travel time difference and, consequently, on the phase difference of the electromagnetic waves, which, after an unwrapping process, gives a displacement estimate at each reflection point. The reflection point is called a PS and corresponds to a point at the Earth’s surface with high and time-coherent reflectivity. Figure 1.10 illustrates the passage of the two satellites on the same track, with *M* and *D* standing for *Mother* and *Daughter* and referring to the measurement of a phase signal by the first and the second satellite. Using these two phases, we obtain the phase difference, ϕ (Hanssen, 2001)

$$\phi = -2\pi\alpha + \phi_{flat} + \phi_{topo} + \phi_{defo} + \phi_{atmo} + \phi_{orb} + \phi_{scat} + \phi_{noise}, \quad (1.1)$$

with α the integer ambiguity, ϕ_{flat} , ϕ_{topo} and ϕ_{defo} are components of the interferometric range, and ϕ_{atmo} , ϕ_{orb} , ϕ_{scat} and ϕ_{noise} are errors caused by the variation in the atmosphere, the scattering properties and the noise between the two acquisitions. The deformation phase relates to the displacement in Line-of-Sight (LoS) of the Earth’s surface, d_{LoS} (Fig. 1.10) and is expressed as

$$\phi_{defo} = \frac{-4\pi}{\lambda} d_{LoS}, \quad (1.2)$$

where λ is the signal wavelength and d_{LoS} the displacement in the LoS, see Fig. 1.9. After processing the phase difference (Kampes, 2006), Φ , we obtain the deformation phase difference to evaluate the displacement in LoS. InSAR-based displacement estimates are sensitive in three directions: east, north, and up. The total displacement, with

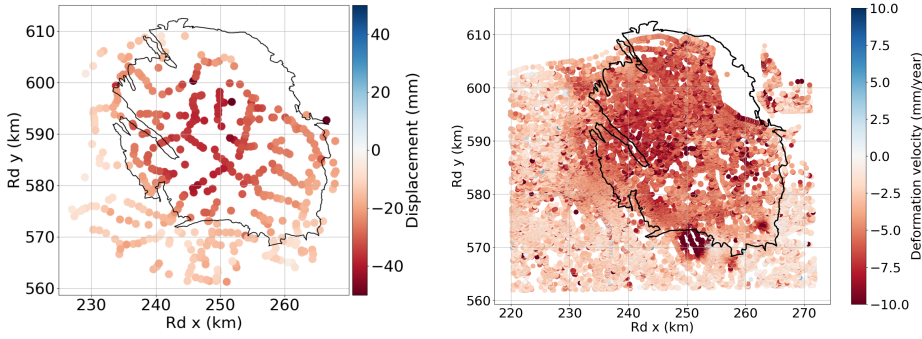


Figure 1.9: Comparison of the spatial distribution of leveling benchmarks and the PS-InSAR showing the higher spatial density of the PS-InSAR compared to the leveling benchmarks. In this example, (left) the leveling displacement estimates in 1987 relative to 1978 and (right) InSAR displacement velocity (linear interpolation of the cumulative displacement over the period 2015-2020). InSAR displacement estimates show more heterogeneity in the subsidence field than in leveling estimates. A typical subsidence bowl with leveling and InSAR is visible above the Groningen gas field.

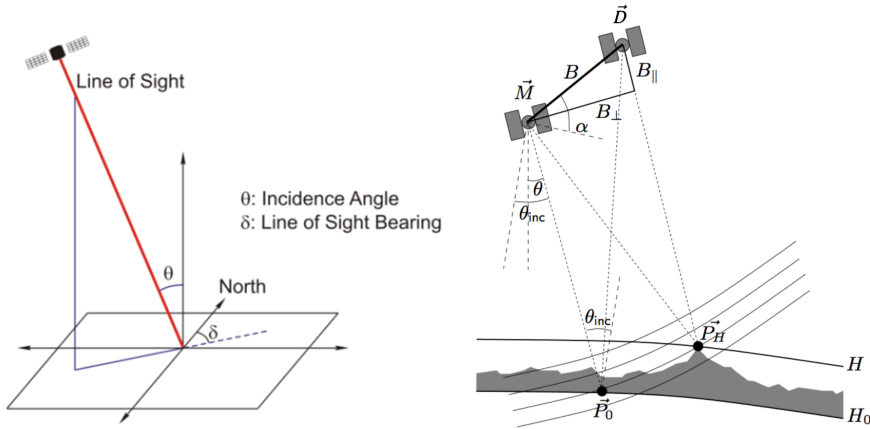


Figure 1.10: Schematic principle of the InSAR technique. (Left) Illustration of a satellite emitting an electromagnetic wave in the LoS direction to the Earth's surface (red solid line). (Right) Illustration of the interferometry principle between two satellite acquisitions: the first satellite (M) and the second satellite (D) pass on the same track and emit an electromagnetic wave; then a phase difference is observed if the observation point has moved between the acquisition of the satellite M and D (Source: CGG, 2022).

displacement vector d_{ENU} , can be projected in the LoS direction and expressed in Cartesian coordinates (E, N, U) (Brouwer and Hanssen, 2023; Hanssen, 2001). We define the projection in LoS d_{LoS} ,

$$d_{\text{LoS}} = [\sin(\theta) \sin(\alpha), \sin(\theta) \cos(\alpha), \cos(\theta)] \cdot (d_{\text{ENU}})^{\text{T}}, \quad (1.3)$$

where d_{ENU} is projected in the LoS given the incident angle θ and α the azimuth of the zero-Doppler plane. The InSAR dataset gives the incident angle θ , whereas the angle α

depends on the ascending or descending track of the satellite. The transformation from LoS to a three-component displacement vector, d_{ENU} , is provided given the availability of different tracks with different viewing geometry (Brouwer and Hanssen, 2023). InSAR displacement estimates involve a mathematical model (i.e., functional model) representing the terms in Eq. (1.1). Several sources of error deteriorate the displacement estimates, and a so-called *stochastic model* is necessary to describe those sources of errors in the unwrapping process. In this thesis, I use InSAR vertical displacements, which are already estimated in the InSAR datasets.

1.2.3. CONTEXTUALIZATION OF THE IN SAR ESTIMATES

To understand the spatial heterogeneity in the subsidence field in Fig. 1.11 compared to the smoother subsidence field in Fig. 1.9, which shows averaged velocities, Fig. 1.12 illustrates how a reflection occurs between the satellite and the Earth's surface. Infrastructures are reflective surfaces with low dispersion. By using the infrastructure reflection surfaces as PS, PS-InSAR provides a signal with high amplitude and good coherence in time. PS-InSAR with a simple reflection on deep-founded buildings (i.e., in the Pleistocene layer) is assumed to be mainly sensitive to deep-driven subsidence (Fig. 1.12). However, many infrastructures in the Groningen region do not have deep foundations, and PS-InSAR estimates exhibit spatio-temporal characteristics other than the deep-driven subsidence from the compaction reservoir. For example, a seasonal variation which suggests surface displacement from the shallow subsurface. The reflection can be more complex than a direct reflection and includes information about the shallow layer. In the case of complex reflection, it is difficult to evaluate the contribution of different driving mechanisms, such as shallow-driven and deep-driven subsidence and displacement, due to infrastructures that contribute to the total displacement. A schematic representation of the subsurface in Fig. 1.11 shows the total subsidence as a superposition of shallow and deep processes. Figure 1.12 illustrates a first case with geotechnical instability, a second with shallow compaction, and a third with deep compaction. The different processes result in total subsidence at the Earth's surface, which can be a nontrivial superposition of several processes, and the sensitivity of the measurement techniques to these processes can vary.

Moreover, Fig. 1.13 gives an overview of InSAR spatial coverage in the Netherlands with an InSAR dataset from Sentinel 1 ascending Track 15, showing the general coverage of PS-InSAR in both rural and urban areas. As previously explained in Fig. 1.11, the sensitivity of InSAR depends on the nature of the reflection. For example, InSAR estimates might be sensitive to deep-driven subsidence in urban areas with deep-founded buildings or deep and shallow-driven subsidence in rural areas with soils such as clay or peat.

To better understand the sensitivity of InSAR to the different processes causing subsidence, Bruna, 2020 contextualizes PS-InSAR as a function of soil type for the entire area of The Netherlands. In previous research, Bruna, 2020 attributes a subsidence-driving mechanism to PS as a function of the subsurface geology. We refer the reader to his work for more details on his methodology. The contextualization of PS-InSAR by Bruna, 2020 has suggested seasonal variation in InSAR displacement time series related to shallow-driven subsidence.

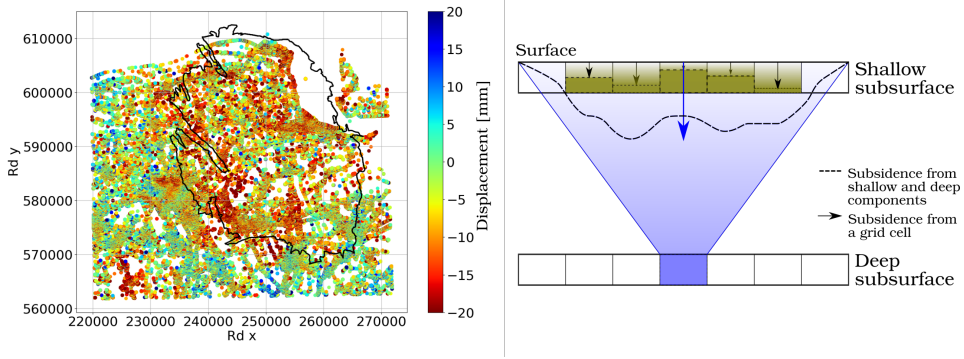


Figure 1.11: (Left) InSAR vertical cumulative displacement at a unique epoch in 2017 relative to 2015 (Sentinel 1 ascending Track 88), showing the spatial heterogeneity in subsidence above the Groningen gas field (black solid line) compared to the InSAR averaged displacement velocity (Fig. 1.9). InSAR vertical cumulative displacements considered at individual epochs show spatial heterogeneity on a kilometer scale. (Right) Scheme of the contribution of shallow-driven subsidence to the deep-driven subsidence illustrating the subsidence bowl and the possible shallow origin of the spatial heterogeneity of the subsidence field.

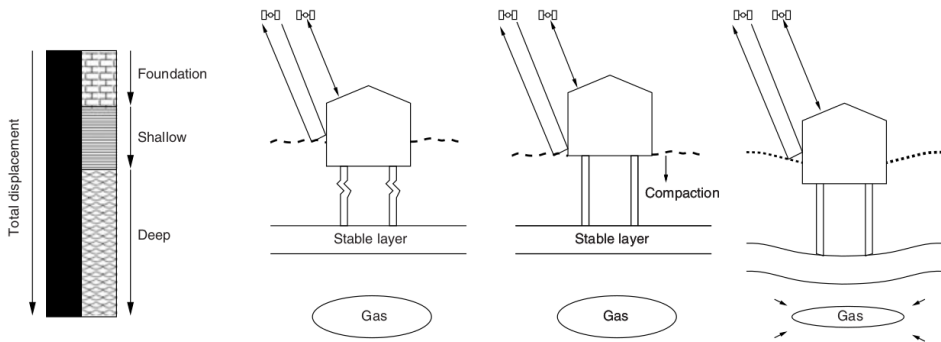


Figure 1.12: Schematic representation of an InSAR reflection illustrating how the sensitivity of InSAR to different subsidence-driving mechanisms varies depending on the reflective object. The three schematic houses show that the total displacement estimated with InSAR can be a superposition of displacements caused by the deep and shallow compaction and caused by foundation instability (Ketelaar, 2009).

Based on a classification of contextual information made by Bruna, 2020, we presented in Fig. 1.6 an approximation of the soil types for the Groningen region. In the next chapters, we will use this simplification of soil geology to further investigate the seasonal variation of the InSAR time series.

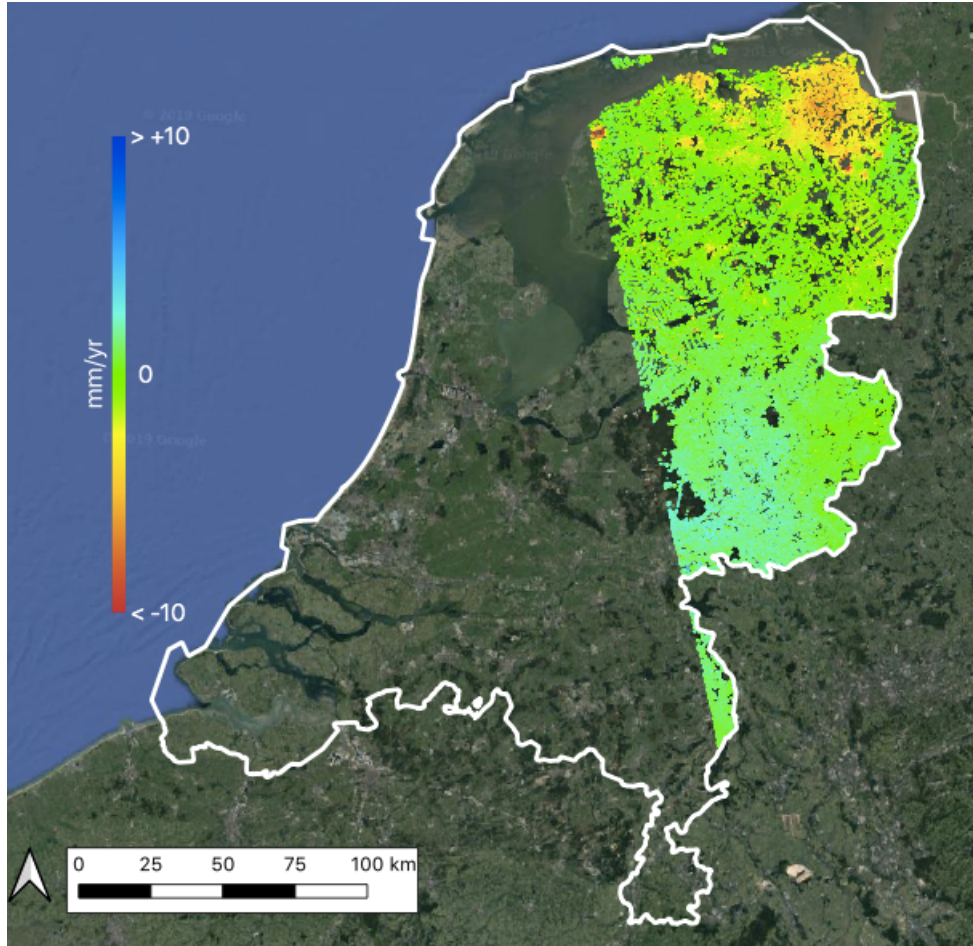


Figure 1.13: Map of the average displacement velocity (mm/year) for the satellite Sentinel-1 ascending track for the Netherlands showing that the InSAR observation points cover both rural and urban areas, despite a lower coverage in rural areas than urban areas. The type of areas has consequences on the sensitivity of InSAR to different processes causing subsidence and can help contextualize PS. Figure courtesy of Bruna, 2020.

1.3. MODELING SUBSIDENCE PROCESSES

In Section 1.1, I introduced subsidence processes occurring in the deep and shallow subsurface. I showed in Section 1.2 that deep- and shallow-driven subsidence estimated with geodetic techniques suggest these processes apply in the Groningen region. In the following section, I present an approach to modeling deep- and shallow-driven subsidence.

1.3.1. SUBSIDENCE CAUSED BY A COMPACTING RESERVOIR

Geertsma, 1973 and Geertsma and van Opstal, 1973 provide an approach to model reservoir compaction and associated subsidence. This approach, known as the nucleus of strain, is still considered the standard in operational subsidence modeling due to reservoir compaction (Bierman et al., 2015; Muñoz and Roehl, 2017; Tempone et al., 2010). In the following, I give the derivation of the solution for a subsidence field created by a compacting reservoir, detailed in Fjaer et al., 2008. We first introduce the solution of a displacement field caused by a depleting sphere, then develop the solution for a disk-shaped reservoir, and finally present the approximation with a set of strain nuclei.

DEPLETING SPHERE

We derive the solution of the displacement field with the differential equation of the displacement created by a depleting sphere, which can be expressed using the radial symmetry of the problem in the spherical coordinates (r, θ, Φ) . The equilibrium equation of the forces, with the stress, $\vec{\sigma}$ gives

$$\frac{d\sigma_r}{dr} + \frac{1}{r} (2\sigma_r - \sigma_\theta - \sigma_\Phi) = 0. \quad (1.4)$$

Using the symmetry $\sigma_\theta = \sigma_\Phi$, we obtain:

$$\frac{d\sigma_r}{dr} + \frac{2}{r} (\sigma_r - \sigma_\theta) = 0. \quad (1.5)$$

The stress is a function of the displacement field, and using Hooke's law, the differential equation of the displacement field is

$$\frac{d^2u}{dr^2} + \frac{2}{r} \frac{du}{dr} - \frac{2u}{r^2} + \frac{\alpha}{\lambda_i + 2G_i} \frac{dP_f}{dr} = 0. \quad (1.6)$$

Where λ_i and G_i are the first and second Lamé parameters at the start of the production, α , the Biot coefficient, and P_f , the final pore pressure at the end of the production. Assuming no fluid flow, the pore pressure remains constant, and $P_f = P_i$. Which gives the differential equation

$$\frac{d}{dr} \left(\frac{1}{r^2} \frac{d}{dr} (r^2 u) \right) = 0. \quad (1.7)$$

The general solution of the displacement field is

$$u(r) = C_1 \cdot r + \frac{C_2}{r^2}, \quad (1.8)$$

where, C_1 , and C_2 , are constants. We assume a spherical symmetry in r^2 , and using the boundary conditions and the continuity principle, we find the values of C_1 and C_2 . The boundary condition $\lim_{r \rightarrow \infty} u(r) = 0$ directly leads to $C_1 = 0$ and the continuity principle $u(r = R_0) = u_0$, gives $C_2 = R_0^2$. Then, the general solution can be expressed as

$$u(r) = u_0 \frac{R_0^2}{r^2}. \quad (1.9)$$

To understand the meaning of the "strength" of the source of strain, we can write u_0 as a function of the volume of the sphere $\Delta V = -4\pi R_0^2 u_0$, which gives $u_0 = -\frac{\Delta V}{4\pi R_0^2}$.

Using the volumetric strain $\epsilon_{vol} = -\alpha C_m \Delta P_f$ and its definition $\epsilon_{vol} = \vec{\nabla} \cdot \vec{u} = -\frac{dV}{V}$, where C_m is the compaction coefficient, the displacement field becomes

$$u(r) = -\frac{\alpha C_m V \Delta P_f}{4\pi R_0^2} \cdot \frac{R_0^2}{r^2}. \quad (1.10)$$

Finally, the expression of the displacement field outside the depleting sphere is

$$u(r) = -\frac{\alpha C_m V \Delta P_f}{4\pi} \cdot \frac{1}{r^2}. \quad (1.11)$$

The expression of the displacement field is valid under the assumption of a homogeneous and infinite medium. The displacement field's strength, or magnitude, is proportional to the product $V \cdot \Delta P_f$. The same is valid for a displacement field for a sphere of half the volume obtained for P_f twice larger. This solution gives the basis of the nucleus of strain approach but doesn't include the boundary condition of vertical stress of zero at the surface. Geertsma, 1966 give a correction of the initial nucleus of strain model of Mindlin and Cheng, 1950 to incorporate the boundary condition of a stress-free surface in the displacement field equations, which leads to the formulation of the current nucleus of strain approach.

NUCLEUS OF STRAIN SOLUTION

The nucleus of strain assumes a point source of subsidence (Fig. 1.14), and the displacement field created by a nucleus of strain in a homogeneous medium with a free surface is

$$\vec{u} = \frac{C_m}{4\pi} \left(\frac{\vec{R}_1}{R_1^3} + (3-4\nu) \frac{\vec{R}_2}{R_2^3} - 6z(z+D) \frac{\vec{R}_2}{R_2^5} + \frac{\vec{z}}{R_2^3} [(3-4\nu)(z+D) - z] \right) V \alpha P_f, \quad (1.12)$$

where the first term represents the depleting sphere in an infinite medium (Eq. (1.11)). Since we are interested in the displacement at the Earth's surface, we take $z = 0$ in the expression in Eq. (1.12):

$$\vec{u} = \frac{C_m \cdot (1-\nu)}{\pi} V \Delta P_f \frac{\vec{R}_1}{R_1^3}. \quad (1.13)$$

With $\alpha = 1$, Eq. (1.13) is the displacement field derived in Geertsma, 1973.

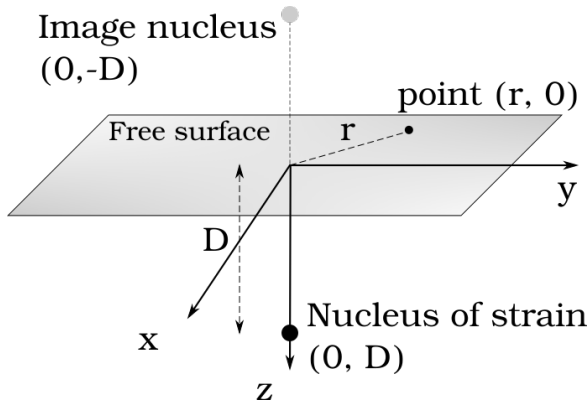


Figure 1.14: Schematic representation of the geometry in the nucleus of strain approach of Geertsma, 1973 illustrating a nucleus of strain at a depth D with the image nucleus to create the free surface that gives the condition of no stress at $z = 0$. The displacement caused by the nucleus of strain is calculated at a point coordinate $(r, 0)$.

DISK-SHAPED RESERVOIR

Since the reservoir is larger than a point source, to represent the subsidence resulting from the compaction of an entire reservoir, Geertsma, 1966, 1973 propose integrating the effect of a nucleus of strain over a disc. To derive the displacement field from a disk-shaped reservoir, we use the vertical component, u_z , of the field \vec{u} in Eq. (1.12) and integrate u_z over the reservoir volume. The same integration can be done with the radial component, u_r (Fig. 1.16). The solution of the displacement field at the surface, $z = 0$, then becomes

$$u_z(r, z = 0) = -2C_m(1 - \nu)\Delta P_f h A(\rho, \eta), \quad (1.14)$$

$$u_r(r, z = 0) = -2C_m(1 - \nu)\Delta P_f h B(\rho, \eta), \quad (1.15)$$

where ρ and η are dimensionless ratios, such as $\rho = \frac{r}{R}$ and $\eta = \frac{D}{R}$. A and B are Bessel's functions, which can be numerically computed.

A disk-shaped reservoir model is a first approximation of the reservoir geometry. Recent studies give examples of the nucleus of strain approach for reservoir models with arbitrary shapes (Muñoz and Roehl, 2017; Tempone et al., 2010). Any reservoir geometry can be approximated using a set of nuclei of strain that discretize the reservoir volume. In this discretization of the reservoir volume, in every grid cell of the model, a nucleus of strain creates stress, and the total strain is the superposition of the contributions of all nuclei of strain.

We can integrate the solution over the grid cell, which is equivalent to integrating the cell thickness from $D - h/2$ to $D + h/2$ only, where D is the depth of the center of the cell, considering the solution uniform in the direction (x, y) (Muñoz and Roehl, 2017). Another approach from Geertsma and van Opstal, 1973 is multiplying Eq. 1.13 by the cell volume. This method is used in recent reservoir models of the Groningen gas field and gives a good approximation of the subsidence field (Candela et al., 2019; van Elk et al., 2022). From model simulations, Fig. 1.15 (right) illustrates how local compaction in reservoirs

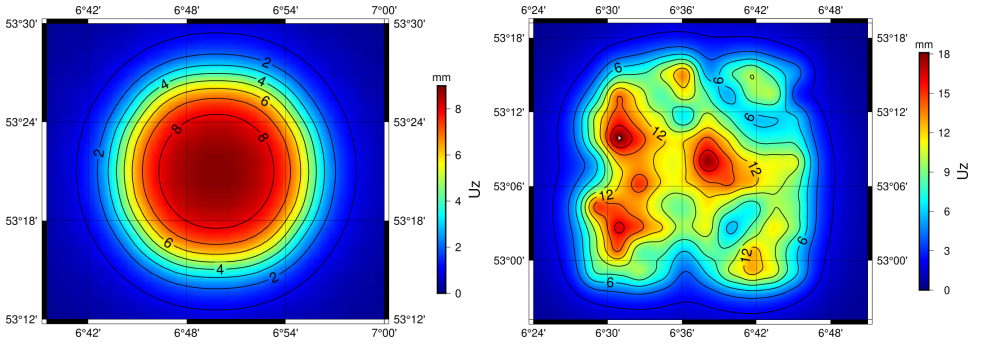


Figure 1.15: Modeled subsidence field of vertical displacements simulated from a compacting reservoir illustrating (left) the subsidence bowl caused by a homogeneously compacting reservoir and (right) a spatially heterogeneous subsidence field caused by a heterogeneous compacting reservoir.

can create local subsidence caused by, for example, compaction in multiple reservoir compartments that are not connected. van Elk et al., 2021 shows that the Groningen gas reservoir has, in fact, a slow pressure equilibration between reservoir compartments. Consequently, we can expect heterogeneity in the reservoir pressure and, thus, spatial heterogeneity in the subsidence field.

1.3.2. SUBSIDENCE CAUSED BY SOIL MOTION

In this section, I describe the subsidence caused by processes in soil layers and how it can be modeled. The Groningen region can be divided into three areas given the soil type: an area with predominantly clay soil in the north and an area with predominantly sand in the south (Fig. 1.6). In addition to the clay and sand, red areas in Fig. 1.6 show areas with peat soil. The first fifteen meters of the soil layers in this region can be highly heterogeneous, with several alternating layers of clay, sand, and peat (Koster et al., 2018). Consequently, modeling shallow subsurface processes in the Groningen area usually requires models with high spatial resolution and spatially varying physical processes (e.g., peat oxidation or clay shrinkage) and geomechanical properties (Fokker et al., 2019; Koster et al., 2018; van Asselen et al., 2018).

CORRELATION OF SUBSIDENCE WITH PRECIPITATION AND EVAPOTRANSPIRATION

Shallow layer motions vary with soil water content, mainly driven by precipitation and evapotranspiration. Conroy et al., 2023 propose an empirical subsidence model based on precipitation and evapotranspiration data. In my thesis, I assume that shallow-driven subsidence u_U^{shal} is a vertical displacement with a localized spatial influence on the total subsidence field due to the shallow depth at which the processes occur. The displacement u_U^{shal} is the sum of a so-called reversible component, R , and a so-called irreversible component, I , of subsidence

$$u_u^{\text{shal}}(\mathbf{x}, P(t), E(t)) = R(\mathbf{x}, P(t), E(t)) + I(\mathbf{x}, P(t), E(t)). \quad (1.16)$$

The reversible component $R(\mathbf{x}, P(t), E(t))$ is characteristic of the seasonal swelling of the soil and is expressed as the function of the precipitation, $P(t)$, and the

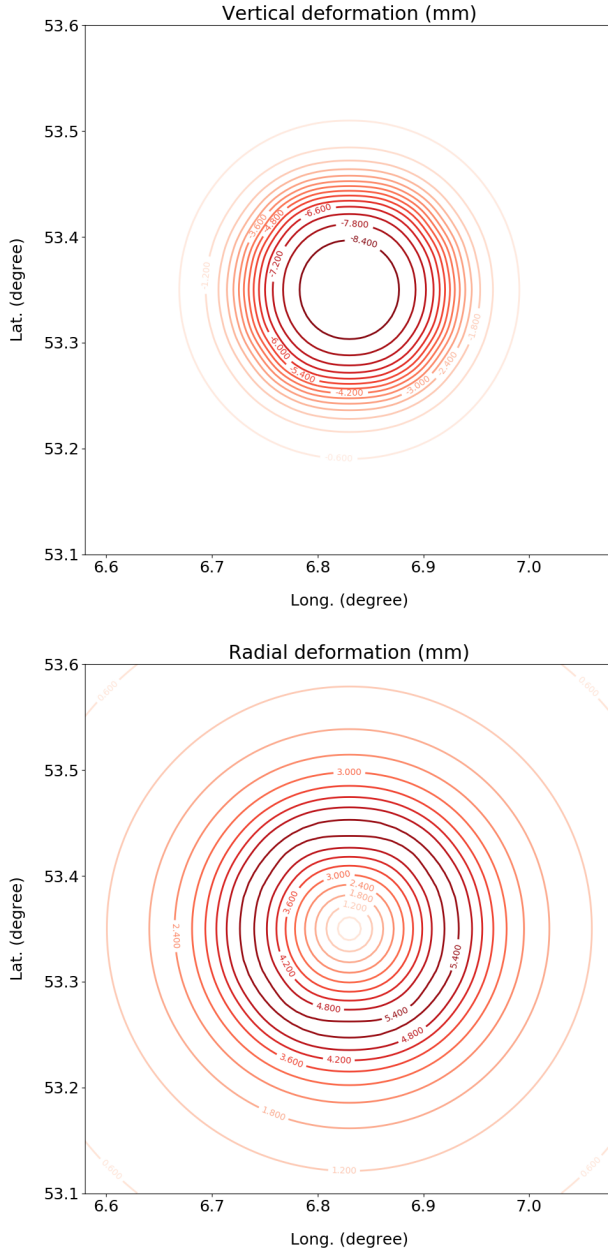


Figure 1.16: Modeled subsidence field from a simulation using a disk-shaped reservoir and homogeneous reservoir compaction, showing the contour lines of the subsidence bowl with (top) inward vertical and (bottom) radial displacement in millimeters. A set of nuclei of strain approximates the disk-shaped reservoir geometry, resulting in the bowl-shaped subsidence field.

evapotranspiration, $E(t)$, such as:

$$R(\mathbf{x}, P(t), E(t)) = \sum_{\tau} [x_P P(t) - x_E E(t),] \quad (1.17)$$

where the $\mathbf{x} = \{x_P, x_E\}$ are scaling factors that depend on the soil per location. The term τ is a characteristic time scale to account for the soil response to external factors such as precipitation and can be seen as memory/hysteresis of the system. Irreversible compaction can occur in soil due to peat oxidation, for example. The empirical derivation of the irreversible shallow subsidence $I(\mathbf{x}, P(t), E(t))$ in the SPAMS model shows good agreement with the extensometer time series of Conroy et al., 2023. $I(\mathbf{x}, P(t), E(t))$ is expressed as a function of a constant rate x_I and a step function f increasing at each time step when the difference between precipitation and evapotranspiration is negative, resulting in a water scarcity, such as

$$I(\mathbf{x}, P(t), E(t)) = \sum_{-\infty}^t x_I f(\mathbf{x}, P(t), E(t)), \quad (1.18)$$

where

$$f(\mathbf{x}, P(t), E(t)) = \begin{cases} 0, & \text{for } R(\mathbf{x}, P(t), E(t)) > 0 \text{ (water surplus)} \\ 1, & \text{for } R(\mathbf{x}, P(t), E(t)) \leq 0 \text{ (water scarcity)}. \end{cases} \quad (1.19)$$

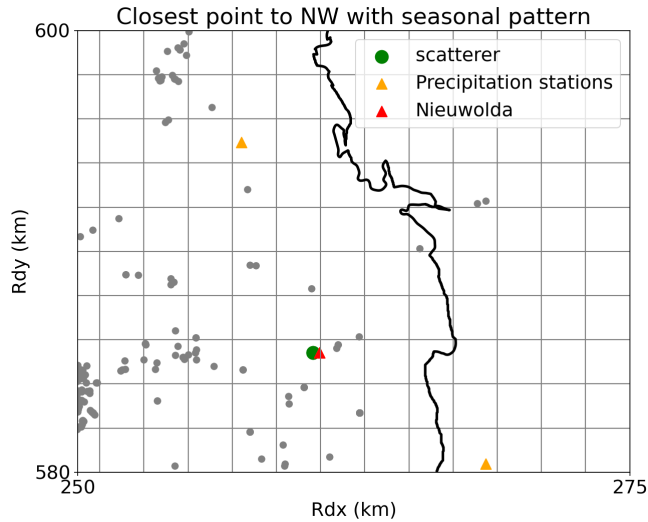


Figure 1.17: Map of the eastern part of the Groningen gas field, which outline is indicated with the black solid line, showing the meteorological station Nieuwolda (red triangle). Locations with subsidence observations from PS-InSAR averaged per parcels are indicated with grey dots, and the closest PS to the station Nieuwolda is indicated with a green dot. Meteorological data are provided by Koninklijk Nederlands Meteorologisch Instituut (KNMI).

In the Groningen gas field, 21 meteorological stations from KNMI provide daily precipitation. The station Nieuwolda (Fig. 1.17) provides daily precipitation, and another station, Nieuw Beerta, provides evapotranspiration data. The evapotranspiration is not recorded at all stations, and Nieuw Beerta is the closest station to Nieuwolda but outside the area represented in Fig. 1.17. I take the area around Nieuwolda as an example because extensometers are installed there to measure shallow-driven subsidence. Figure 1.17 shows a part of the Groningen gas field with some PS-InSAR selected for their time series, showing a seasonal pattern possibly representing a shallow-driven subsidence. Figure 1.18 illustrates the correlation

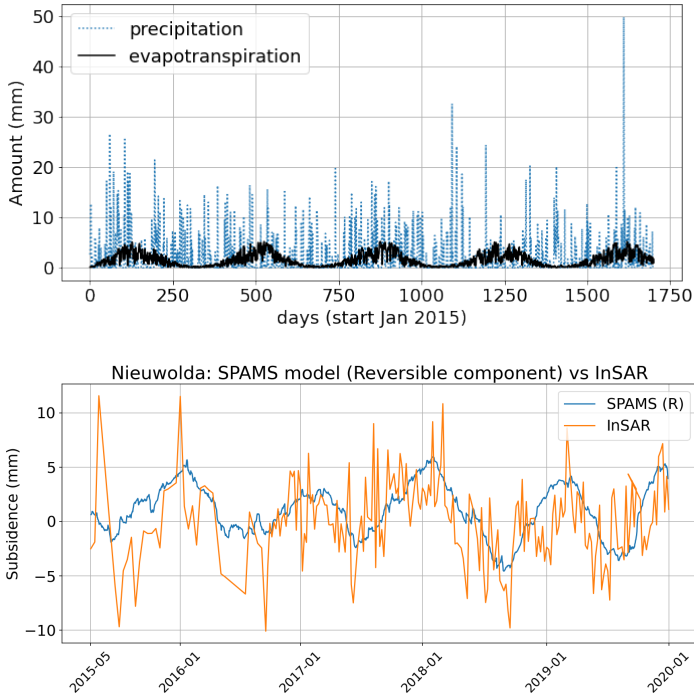


Figure 1.18: (Top) Daily precipitation data from the station Nieuwolda and evapotranspiration data from the Station Nieuw Beerta in millimeters from January 2015 to January 2020. (Bottom) Assimilation of the daily precipitation and evapotranspiration data in data assimilation provides the best fit of the SPAMS model (blue solid line) to the detrended InSAR time series (orange solid line), selected from the closest PS to the station Nieuwolda (Fig. 1.17).

between meteorological data and subsidence. For example, the detrended InSAR time series in Fig. 1.18 shows a subsidence pattern with seasonal variation. Soil motion has an uplift in winter and subsidence in summer, which correlates with soil expansion and shrinkage caused by the variation of soil water content. A preliminary test with the SPAMS model in fig. 1.18 suggests that a model based on meteorological data can represent the shallow-driven subsidence and could thus have value for shallow-subsidence modeling in the Groningen region.

CORRELATION OF SUBSIDENCE WITH ATMOSPHERIC TEMPERATURE

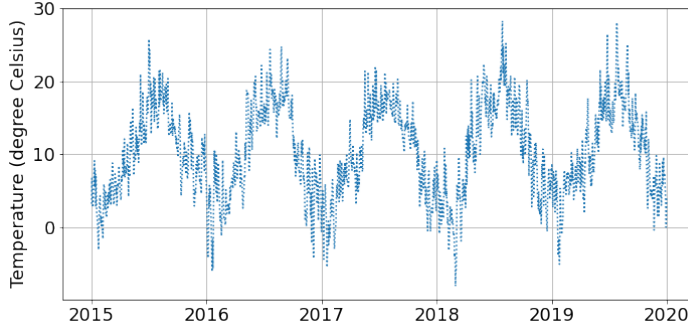


Figure 1.19: Daily averaged temperature in the Netherlands from January 2015 to January 2020 in degrees Celsius showing seasonal variation similar to the evapotranspiration data.

Like the approach of the SPAMS model, I reduced the number of model parameters using only the atmospheric temperature data. Similarly to precipitation and evapotranspiration, atmospheric temperature varies according to the weather with seasonal changes, thus correlating with seasonal soil motion. For example, the atmospheric (i.e., air) temperature directly affects the soil moisture in the first centimeter of soil below the surface (Jansson, 1998). We should note that seasonal change also correlates with other processes, such as thermal infrastructure expansion and increased hydrocarbon production in winter. This might complicate the interpretation of the seasonal variability in soil motion.

Similarly to the shallow displacement in Eq. 1.16, the displacement u_u^T is the total displacement and is defined as the sum of a reversible component R , and an irreversible component, I ,

$$u_u^T(\mathbf{x}, T(t)) = R(x_\theta, T(t)) + I(x_I, T(t)). \quad (1.20)$$

x_θ is the scale factor related to temperature changes, x_I relates to the irreversible deformation, and $R(x_\theta, T(t))$ is defined as the reversible component which relates to the subsidence caused by the seasonal processes:

$$R(x_\theta, T(t)) = x_\theta T(t). \quad (1.21)$$

The irreversible component is proportional to a step function $f(x_I, T(t))$

$$I(x_I, T(t)) = \sum_{-\infty}^t [x_I f(T(t))], \quad (1.22)$$

with

$$f(T(t)) = \begin{cases} 0, & \text{for } T(t) \leq \theta_{\text{thr}} \text{ (soil moisture increases)} \\ 1, & \text{for } T(t) > \theta_{\text{thr}} \text{ (soil moisture decreases)}, \end{cases} \quad (1.23)$$

where θ_{thr} is a temperature threshold. Equation 1.21 can be used to model the long-term subsidence, similar to the subsidence in the SPAMS model, which assumes increasing

long-term subsidence when the evaporation is higher than the precipitation. The same applies to a temperature above a certain threshold. For example, soil water content data (5 cm depth) starts decreasing when the average air temperature is 15 degrees Celsius (Alvenäs and Jansson, 1997). Similarly, soil models correlating soil water content with temperature show that soil water content decreases when the air temperature reaches 10 to 15 degrees Celsius (Jansson, 1998).

1.4. DATA ASSIMILATION

IT can be difficult to describe a system when physical processes are not observable. This is particularly true for processes in the subsurface where measurements are punctual or impossible. We build models and compare their outputs with observations to improve our knowledge of these processes. For example, we cannot directly observe reservoir compaction, but we can observe subsidence caused by reservoir compaction.

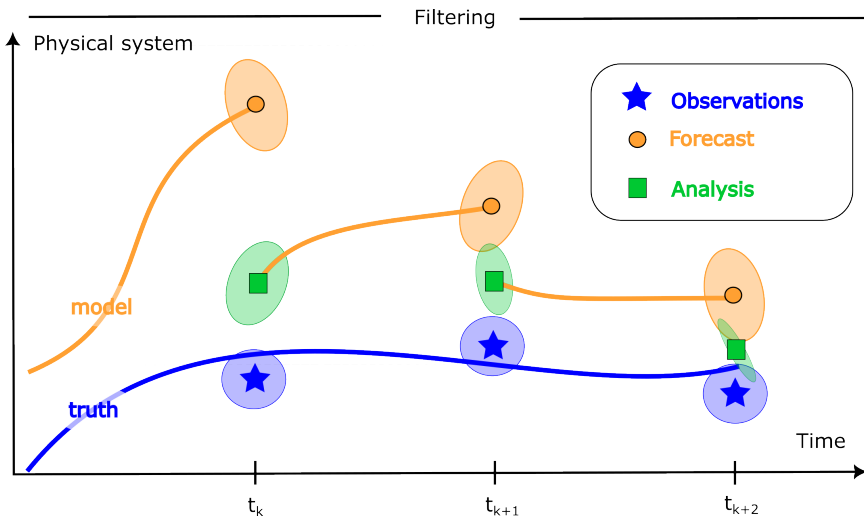


Figure 1.20: Schematic illustration of the principle of sequential filtering, which combines model estimates (orange) with observations (blue stars) to update the analysis (green). The shaded areas represent a probability density with variance decreasing in time as the uncertainty in the analysis decreases at each new assimilation step.

With data assimilation, we can combine physics-based models with observations to estimate the system's unknowns and the time evolution of the model states used to describe dynamical processes. Figure 1.20 gives a schematic illustration of the data assimilation principle. We assume a truth (blue line) that evolves over time for the physical process we want to understand better and eventually forecast. Observations of the truth are imperfect, with a measurement error that we represent with a shaded circle in Fig. 1.20. A model (orange) describes the state's time evolution, and this model state also contains errors (orange shaded circles). The data assimilation result is illustrated in green with the so-called analysis, in which information on the physical process from both the model and the observation is combined to estimate the non-observable

states, quantify the uncertainty about the state of the physical process, and improve the forecast thereof. In data assimilation, a probability density function (PDF) represents the knowledge (and, accordingly, the uncertainty) we have about the model, the observation, and the estimated state. In Figure 1.20, these PDFs are indicated with shaded circles of varying shapes.

In the following section, I provide an overview of data assimilation and briefly review the particle filter and how we can estimate the states of the physical processes.

1.4.1. REPRESENTING A PHYSICAL PROCESS

In this thesis, we are interested in a data-assimilation method, the particle filter. The filtering approach assumes a Markov process in which the model at the time step $k + 1$ only depends on the previous time step k . Because of this, we can apply the particle filter sequentially and assimilate new observations when they are available.

As mentioned above, it is impossible to know or to model exactly the non-observable model states, and the best that we can do is to model this state with

$$\mathbf{x}^k = \mathcal{M}(\mathbf{x}^{k-1}) + \beta^k. \quad (1.24)$$

$\mathcal{M}(\mathbf{x}^{k-1})$ represents the deterministic part of the state evolution, and β^k is the stochastic part of the model, which is typically unknown and cannot be modeled with a deterministic term. β^k can also be seen as a representation of the error in the dynamical model. Based on the state evolution as described in Eq. 1.24, we can consider it the objective of data assimilation to better model \mathbf{x}^k by adding to the estimation information from the observations \mathbf{y} .

1.4.2. BAYESIAN INFERENCE

To understand how data assimilation estimates the process, we start by defining the model state vector, \mathbf{x} . As mentioned earlier, the model states are the system's unknowns, and it is usually impossible to know their exact values. We define model states with the unknown state vector \mathbf{x} , of dimension N_x , with the *true* value, \mathbf{x}_t . Data assimilation provides the best estimate of \mathbf{x}_t denoted as \mathbf{x}^a . The superscript a stands for analysis.

Model states of \mathbf{x} , are mapped to the observations with

$$\mathbf{y}^k = \mathcal{H}(\mathbf{x})^k + \mathbf{e}^k, \quad (1.25)$$

where \mathcal{H} is the observation operator, which maps the state space to the observational space, including a measurement error, \mathbf{e} . Similarly to Eq. (1.24), we define the dynamical model \mathcal{M} . \mathcal{M} gives the time evolution of the states from time $k - 1$ to time k with a model error, ϵ

$$\mathbf{x}^k = \mathcal{M}(\mathbf{x}^{k-1}) + \epsilon^k. \quad (1.26)$$

Eq. (1.25) and Eq. (1.26) illustrate how we represent the uncertainty of the observations and the model. The question is how much we should trust the model or the observations when comparing them. A probabilistic approach can help quantify uncertainty and thus balance the importance of models and observations in the analysis. Assuming that we know the probability of a state in a physical process, we can define the PDF of this state. In the estimation problem, we wish to estimate the PDF of the states \mathbf{x} , given the

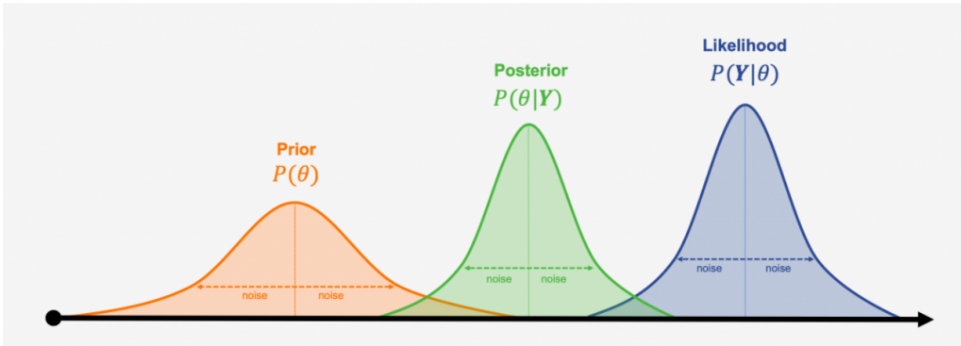


Figure 1.21: Principle of Bayes' theorem with a schematic representation of the probability density functions of the prior (orange) and the likelihood (blue). The green probability density function represents the posterior, which is the Gaussian product of the prior with the likelihood.

observations \mathbf{y} , which is denoted by $p(\mathbf{x}|\mathbf{y})$. To derive this conditional PDF, we use Bayes' theorem

$$p(\mathbf{x}, \mathbf{y}) = p(\mathbf{x}|\mathbf{y}) p(\mathbf{y}) = p(\mathbf{y}|\mathbf{x}) p(\mathbf{x}), \quad (1.27)$$

leading to:

$$p(\mathbf{x}|\mathbf{y}) = \frac{p(\mathbf{y}|\mathbf{x}) p(\mathbf{x})}{p(\mathbf{y})}. \quad (1.28)$$

The marginal PDF, $p(\mathbf{y})$, is a normalization term. Figure 1.21 illustrates Bayes' theorem (Eq. (1.28)), where prior and likelihood are represented with a Gaussian PDF, which variance represents the uncertainty in the model and observations. The posterior distribution is proportional to the product of the prior and the likelihood, and the posterior variance is consequently proportional to the product of the variance in the prior and the likelihood.

To apply Bayes' theorem, the prior PDF and the likelihood are represented by a discrete sample using Monte Carlo sampling methods. The particle filter (Beskos et al., 2014; Snyder et al., 2008; van Leeuwen et al., 2019; Wikle and Berliner, 2007) is an ensemble-based data assimilation method and uses Bayes' theorem. The next question is how to sample the prior to obtain a posterior PDF, which represents the state PDF we try to estimate, defined as the target PDF. In the following, I describe the importance of sampling in the particle filter and illustrate how to approximate the target PDF.

1.4.3. IMPORTANCE SAMPLING

From the previous description of data assimilation, the aim principle is to estimate an evolving process. The true state of the process has a PDF called the target PDF, which we try to estimate. To efficiently sample the prior state, considering the objective of approximating the target PDF, we introduce a proposal density, also called prior proposal density. In importance sampling, the proposal density, $p(x)$, generates a discrete sample of model states called particles, which aim to represent the target PDF

$$p(x) = \sum_{i=1}^{N_e} \frac{1}{N_e} \delta(x - x_i). \quad (1.29)$$

By applying Bayes' theorem in Eq. (1.28), we weigh each particle to approximate the target PDF, providing a discrete posterior distribution according

$$p(x|y) = \sum_{i=1}^{N_e} w_i \delta(x - x_i), \quad (1.30)$$

where w_i is the weight attributed to each particle with

$$w_i = \frac{p(\mathbf{y}|\mathbf{x}_i)}{\sum_{j=1}^{N_e} p(\mathbf{y}|\mathbf{x}_j)}. \quad (1.31)$$

This shows we can approximate the target PDF with particles drawn from different densities and weighed proportionally to the difference between the model and observations. The best estimate of the state vector \mathbf{x} , i.e., the analysis, is the expected mean of the posterior distribution. Importance sampling gives an approximation of the expectation of the function, $f(x)$, representing the target PDF

$$E[f(x)] = \int f(x)p(x)dx \approx \sum_{i=1}^{N_e} w_i f(x_i). \quad (1.32)$$

The particle filter is an implementation of importance sampling, in which we use the definition of a Markov process (Sec. 1.4.1) to calculate the system's time evolution sequentially. We can then write the prior proposal density by decomposing the probability of the model states at each time step

$$p(x^{0:k}) = p(x^k|x^{0:k-1})p(x^{0:k-1}). \quad (1.33)$$

To simplify the notation, we consider the evolution of a single model state. In Equation (1.34), $p(x^{0:k})$ is the probability of the model state at time t_k starting with the initial conditions at time t_0 . This can be expressed as a conditional probability considering the previous time step from t_0 . Using the definition of the Markov process, each time step only depends on the previous time step. This means that time t_k only depends on the time t_{k-1} and that the state evolution further in the past does not add information on the probability of the state at time t_k . Therefore, we can write

$$p(x^{0:k}) = p(x^k|x^{k-1})p(x^{0:k-1}), \quad (1.34)$$

where $p(x^k|x^{k-1})$ is defined as the transition density, also called transition kernel. We can use the same property to decompose $p(x^{0:n})$ in a product of transition density from t_0 to t_k

$$p(x^{0:k}) = p(x^k|x^{k-1})p(x^{k-1}|x^{k-2})\dots p(x^1|x^0)p(x^0). \quad (1.35)$$

For the implementation of the particle filter, we want to know the transition density, $p(x^k|x^{k-1})$, which allows us to forecast the model state from time $k-1$ to time k , where new observations are available. The transition density relates to the dynamical model in Eq. (1.26), with the model error representing the stochastic part of the system and, consequently, the primary source of error in the model forecast. Figure 1.22 illustrates the principle of the particle filter with sequential assimilation. The initial ensemble

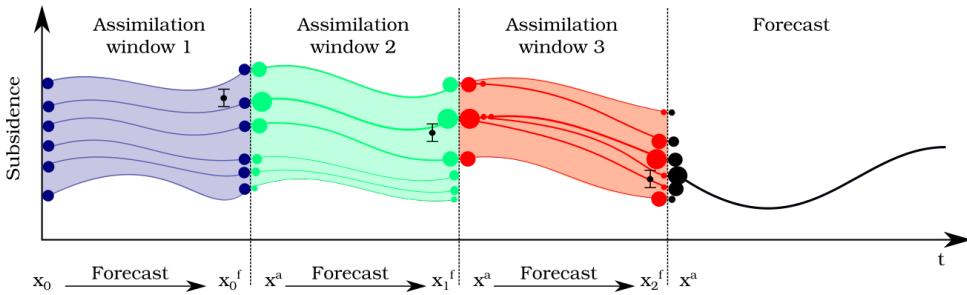


Figure 1.22: Schematic principle of the particle filter with a sequential update at each new available observation. The particle weights are updated at the end of each assimilation window, and the best estimate of the state vector produces a forecast after the three assimilation windows.

(blue dots) in the first assimilation window is generated to represent the target PDF. Ensemble members are projected in time with the dynamical model at time $k + 1$, where an observation is available. In the analysis, each particle is weighted. The posterior distribution provides an updated to better approximation of the target PDF, illustrating the principle of importance sampling. Forecast and analysis steps can be iterated at each new observation. Note that in importance sampling, the value of the particles is not changed, and only the weights are updated. This can have a detrimental effect if the distance between particles and observation increases in time. In that case, strategies such as resampling or tempering can help correct the ensemble of particles (Li et al., 2015).

A particle filter algorithm can be described in three steps:

Initialization Importance sampling starts with N_e particles, or also called ensemble members, $\{\mathbf{x}_1, \mathbf{x}_2, \dots, \mathbf{x}_m\}$ sampled from a probability density $p(\mathbf{x}^{k-1})$, which approximates the exact target density. The initial sampling is represented in Fig. 1.22 at the start of the assimilation window 1, with blue dots as a schematic representation of the initialized particles.

Forecast The particles m , are propagated from time $k - 1$ to time k with $\mathbf{x}_m^k = \mathcal{M}(\mathbf{x}_m^{k-1}) + \mathbf{e}^k$, i.e., using the transition density.

Analysis At the end of the assimilation window (Fig. 1.22), we apply Bayes' theorem (Eq. (1.28)) and give and update the weight of each particle given the observations. We compare the model predictions $\mathcal{M}(\mathbf{x}_m^{k-1})$ with the observations \mathbf{y}^k through the likelihood $p(\mathbf{y}|\mathbf{x})$. The likelihood is a PDF, which represents the distribution of the uncertainty in data, and the posterior distribution $p(\mathbf{x}|\mathbf{y})$ is calculated by weighting each particle. The posterior weights are normalized with $\sum_{j=1}^{N_e} w_j = 1$. Then, the expected value of the posterior distribution provides an estimator of the state variable values.

1.5. RESEARCH OBJECTIVES

COMBINING model-predicted subsidence with the geodetic estimates through data assimilation can help estimate subsidence based on a physical description of its driving mechanisms, reducing uncertainty in model parameters and variables. In this thesis, I implement a data-assimilation method, the importance sampling, to assimilate leveling and InSAR estimates. This allows us to understand the subsidence-driving mechanisms and, eventually, forecast subsidence. Sources of uncertainty in data assimilation are a) errors in the physical model, b) errors in the data, and c) approximations in the data assimilation method (Evensen et al., 2022; Nearing et al., 2018; van Leeuwen et al., 2015). When assimilating leveling and InSAR estimates, data errors include instrumental and processing errors. For example, in the case of InSAR, errors come from the unwrapping process, the contextualization process, and other aspects of the data processing (Sec. 1.2). In the case of model-predicted subsidence, the physical-model errors stem from the uncertainty in model inputs and approximations of the physical processes. In the Groningen subsidence estimation problem, physical models simulate subsidence as a function of pressure variation and the reservoir's geomechanical properties (Sec. 1.3.1). As a result of errors in these inputs and initial conditions, the model can provide erroneously predicted subsidence. The approximations in the data assimilation method are typically related to the limited computational resources to sample the solution space of our estimation problem.

A range of inversion and optimization methods, such as least-square inversion, conjugate gradient, or Newton methods, can be used in estimation problems to fine-tune model parameters and better represent subsurface properties (Tarantola, 2005). However, since the model and data contain partly unknown errors, it is uncertain how to weigh the information from the model and the data in these methods. Data assimilation provides a mathematically consistent manner to balance the information of models and data. Various data assimilation methods exist and are applied to problems such as weather forecasts, oceanography, physical geography, and, in our example, reservoir engineering (Evensen et al., 2022; van Leeuwen et al., 2019). The data assimilation approach in this study, importance sampling, provides a formulation of these estimation problems to estimate model states and their uncertainty probabilistically (Evensen et al., 2022).

Importance sampling is a straightforward algorithm for updating the ensemble (i.e., the ensemble of model realizations) and their probability using Bayes' theorem. The particle filter is an implementation of importance sampling with a sequential update of a dynamical model and is used for model forecasts. The terms *importance sampling* and *particle filter* are used interchangeably in this thesis if the model is time-dependent and used for forecasting. Importance sampling is not often used in geoscience applications because of the computational inefficiency in problems with a large number of parameters and observations, which require a large number of model realizations, referred to as the ensemble size (Bengtsson et al., 2008; Beskos et al., 2017; Chorin and Morzfeld, 2013). However, variants of the particle filter algorithm from Doucet et al., 2000; Snyder, 2011; van Leeuwen et al., 2019 suggest its potential for application in the Groningen region. Moreover, whereas most data assimilation methods under-perform in nonlinear problems and approximate model and observation errors

with Gaussian statistics, importance sampling provides an approach for nonlinear systems without Gaussian assumptions.

To apply importance sampling to the Groningen subsidence estimation problem, we know from earlier studies from Ketelaar, 2009 and Bruna, 2020 that PS-InSAR are sensitive to different subsidence-driving mechanisms other than those from the compacting reservoir. Other studies showed that averaged velocities from interpolated InSAR time series show a good ability to represent deep-driven subsidence (Bourne et al., 2014; Fokker et al., 2016; Smith et al., 2019). However, assimilating cumulative displacements from InSAR time series instead of averaged velocities requires modeling all relevant subsidence-driving mechanisms to compare modeled subsidence with InSAR estimates adequately. This includes, for example, modeling short-time scale subsidence-driving mechanisms and shallow-driven subsidence. Developing a data assimilation framework that has the potential to work with a model that represents all relevant processes and effectively incorporates the densely sampled information of the InSAR estimates in space and time leads to the following main research question:

How can importance sampling be efficiently applied for subsidence estimation in the Groningen region to identify its driving mechanisms better?

To address this problem, I identify the following sub-questions:

1. How can we apply importance sampling in a subsidence estimation problem of the complexity of the Groningen gas field?
2. How can we effectively use InSAR data for subsidence estimation with data assimilation?
3. How can data assimilation identify subsidence-driving mechanisms given the spatial and temporal scales of geodetic displacement estimates?

To answer these questions, the thesis is divided into five chapters:

In Chapter 1, I introduce the history of the Groningen region. I review the different subsidence-driving mechanisms, the principle of geodetic techniques, and the data assimilation principle. Different processes at varying depths can cause subsidence. Before introducing the subsidence models, I give an overview of the principles of the InSAR technique and the sources of errors in InSAR processing. To model subsidence-driving mechanisms, the nucleus of strain approach of Geertsma, 1973 is used to derive a subsidence field created by a compacting reservoir, and shallow-driven subsidence can be described based on meteorological data. Finally, I introduced the basis of Bayesian inference, the importance of sampling in data assimilation, and how this is used in the particle filter.

In Chapter 2, I evaluate the applicability of importance sampling in a problem of the size of the Groningen gas field involving a large number of model variables and subsidence observations. Based on the nucleus of strain approach (Geertsma, 1973), a compacting reservoir model creates the characteristic bowl-shaped subsidence profile over the Groningen region. Given the spatial correlation in the subsidence bowl, I use synthetic tests to evaluate the necessary ensemble size to ensure the quality

of the posterior estimates. Two factors influence the required ensemble size in the assimilation of subsidence observations above the Groningen gas field: the total number of observations and the spatial correlation in the subsidence signal, i.e., a smooth subsidence bowl or a spatially heterogeneous subsidence signal. I propose quantifying the quality of data assimilation results based on the information content in the posterior distribution. By quantifying how the information propagates from prior knowledge and data into the data assimilation result, we can evaluate the efficiency of the importance sampling method. The theory of Monte Carlo sampling, which forms the basis of importance sampling, implies that a loss of information in the posterior means that the ensemble size must increase to conserve minimal efficiency.

In Chapter 3, I propose an implementation of the importance sampling based on the work of Doucet et al., 2000, which allows us to avoid information loss when assimilating an increasing number of leveling and InSAR estimates. The adapted implementation of the importance sampling, the *optimal proposal importance sampling* shows good applicability in synthetic experiments and with actual leveling and InSAR datasets. However, the typical size of approximately 1.5 million spatially distributed data points in InSAR still requires a dataset reduction for a particle-filter application with a limited ensemble size.

In Chapter 4, I propose a data-assimilation methodology based on importance sampling to assimilate InSAR time series to estimate and forecast subsidence. I investigate how to conceptually model subsidence-driving mechanisms in the Groningen region and provide proof of concept in separating subsidence regimes using synthetic experiments and the spatio-temporal characteristic of the subsidence signal. The methodology tested with InSAR datasets allows forecasting seasonal evolution of subsidence and provides insights into improving the modeling of subsidence-driving mechanisms.

In Chapter 5, I conclude this thesis with a conclusion per chapter with recommendations for the future development of subsidence estimation with data assimilation in the Groningen region.

2

EFFECT OF SPATIALLY CORRELATED SUBSIDENCE SIGNAL IN SUBSIDENCE ESTIMATION WITH IMPORTANCE SAMPLING

Of course, the entire effort is to put oneself outside the ordinary range of what are called statistics.

Stephen Spender

The particle filter is a data assimilation method based on importance sampling for state and parameter estimation. We apply a particle filter in two different quasi-static experiments with models of subsidence caused by a compacting reservoir. The first model considers uncorrelated model state variables and observations, with subsidence fields resulting from a single source of strain. In the second model, the subsidence field is a summation of subsidence contributions from multiple sources, which causes spatial dependencies and correlations in the modeled subsidence field. Assimilating these correlated subsidence fields may trigger weight collapse. With synthetic tests, we show in a model of subsidence with 50 independent state variables and spatially correlated subsidence, a minimum of 10^{13} particles are required to have information in the posterior distribution identical to that in a model with 50 independent and spatially uncorrelated observations.

Spatial correlations cause information loss that can be quantified with mutual information. We illustrate how a stronger spatial correlation results in lower information content in the posterior and empirically derive the required ensemble size for the

Parts of this chapter have been published in Computational Geosciences: Kim and Vossepoel, 2024, On spatially correlated observations in importance sampling methods for subsidence estimation.

importance sampling to remain effective. We furthermore illustrate how this loss of information is reflected in the log-likelihood and how this depends on the number of model state variables. Based on these empirical results, we propose criteria to evaluate the required ensemble size in data assimilation of spatially correlated subsidence fields.

2.1. INTRODUCTION

As introduced in Section 1.4, data assimilation combines observations with models to estimate model parameters and variables. Parameter values remain constant in time, whereas variable values evolve in time. We use the term state vector for the quantities to be estimated so the state vector can contain both parameters and state variables. The complexity of a data assimilation system rapidly increases with the number of model state variables and observations and has implications for how we predict physical processes with the data assimilation system.

One of the methods used in data assimilation is the particle filter (van Leeuwen et al., 2019) or the particle method (Vossepoel and van Leeuwen, 2007) for static problems. The particle method that we use is a static application of the particle filter and is, in essence, an importance sampling method. The particle method refers to importance sampling in static data assimilation problems in the following. Importance sampling, filtering, and ensemble-based methods have been applied for subsidence estimation (Fokker et al., 2016; Zoccarato et al., 2016). Other authors (Evensen et al., 2019; Evensen and Van Leeuwen, 2000; Gazzola et al., 2021) have used an ensemble smoother (ES) and an iterative ensemble smoother to estimate subsurface geomechanical state variables. Given the system's complexity, an essential question in these applications is whether the ensemble spread is sufficiently large to ensure the method's applicability.

In many applications, the ensemble size is chosen based on trial and error. The particle method, like most other importance sampling methods, suffers from weight collapse, and its performance exponentially degrades as the dimension of the state and observation spaces increases (Bengtsson et al., 2008; Beskos et al., 2014; Snyder et al., 2008). We can prevent this weight collapse by increasing the ensemble size. A more systematic approach to evaluate the necessary ensemble size has been proposed by Snyder et al., 2008 and Bengtsson et al., 2008 and tested in a practical example through the work of Slivinski and Snyder, 2016. However, analytic derivations of the ensemble size in these publications are often based on abstract problems, and the results are not always easily translated to geoscience problems (van Leeuwen et al., 2019). Snyder et al., 2008 highlight, for example, the problem of non-Gaussian prior and observations and the nontrivial dependencies between state variables and observations. In this study, we will extend the results of Snyder et al., 2008 to empirical cases with spatially correlated fields of observations, focusing specifically on the feasibility of the particle method and its performance. We illustrate this with an example of subsidence caused by reservoir compaction due to a pressure variation, where observations of subsidence allow us to estimate the geomechanical properties of the reservoir (Fokker et al., 2012; Fokker et al., 2016). Spatial correlations exist in nearly all geophysical fields and appear in a subsidence field when a single subsidence source causes a surface displacement over a certain region, e.g., a subsidence bowl with a width of several kilometers. In general, a deeper source of subsidence in the subsurface creates a subsidence field at the surface with a more significant correlation length. In comparison, subsidence from a shallower source has a shorter correlation length. Moreover, a spatially correlated subsidence field does not necessarily imply that the measurement errors are correlated, and in this study, we assume independent measurements and, hence, uncorrelated measurement

errors. In a previous study on the particle filter, Snyder et al., 2008 derive a theoretical relationship between the maximum weight, w_{max} of the particles and the dimension of the problem for an example of independent and identically distributed (i.i.d.) samples and under the assumption of a standard normal density for the prior and the likelihood. In their study, the authors generalize the results at an asymptotic limit with a linear transformation from model state space to the observation space represented by an I_d (identity) observation operator. Strategies to assimilate spatially correlated observations for a large number of observations are developed by Simonin et al., 2019. However, to our knowledge, there is no theoretical approach to estimate the criterion for weight collapse and the required ensemble size in a spatially correlated field, that is when a variable at one location depends on variables at other locations. The objective of the present study is to evaluate the necessary ensemble size that ensures the applicability of the particle method and that avoids weight collapse when 1) the system dimension increases and 2) when the observed field is spatially correlated. For this, we use two conceptual models of subsidence: 1) a one-component model and 2) a multi-component model of subsidence. In the one-component subsidence model, we use a one-to-one transformation from the model state variables of the reservoir pressure variation to subsidence, which gives i.i.d. subsidence values to represent a first-order approximation of a compacting reservoir without spatial correlation. The multi-component model, which includes spatial correlation, is based on the nucleus of strain approach of Geertsma, 1973, which has been used in literature to estimate geomechanical reservoir properties (Du and Olson, 2001; Fokker et al., 2016). The resulting subsidence shows spatial correlation, as the displacement field is a superposition of subsidence created by a pressure variation in different reservoir compartments. Consequently, the subsidence values are linear combinations of the pressure variation and, therefore, not i.i.d.. To derive the ensemble size in problems with spatial correlation, we propose an empirical quantification of the information in both the prior knowledge and the posterior estimate using the formalism of mutual information in information theory. Mutual information can be used to quantify the available information from models and observations as demonstrated in Nearing et al., 2018. We propose to use a similar metric based on entropy and mutual information to quantify the information loss in the case of posterior weight collapse.

This chapter is organized as follows. Section 2.2 gives an overview of importance sampling and the previous results of Snyder et al., 2008 for weight collapse in high-dimension. In Section 2.3, we present the subsidence models, and in Section 2.4, using information theory with the metric of mutual information, we extend the results of Snyder et al., 2008 to the example of spatially correlated subsidence. Results in Section 2.5 illustrate how the ensemble size must increase with spatially correlated observations to avoid degradation of the efficiency of the importance sampling. Sections 2.6 and 2.7 conclude our study.

2.2. IMPORTANCE SAMPLING METHOD

In this section, we first give a brief overview of importance sampling, which is at the base of the particle method, and we introduce the problem of weight collapse.

2.2.1. BACKGROUND ON IMPORTANCE SAMPLING

The correct description of a physical system can be uncertain when physical processes are not directly observable, for example, processes happening in the subsurface that can only be indirectly observed at the surface. Assuming that we know the probability of a physical process, we can approximate its exact probability density function (PDF), i.e., the target PDF, by a discrete distribution. In Section 1.4.3, we introduced the principle of importance sampling to estimate the probability of a model variable or a parameter, \mathbf{x} , given the observations \mathbf{y} (Doucet et al., 2001; Morzfeld et al., 2018; van Leeuwen et al., 2015). In the following, we adopt the definition of importance sampling for a quasi-static application with the particle method. We briefly overview importance sampling and refer to Chapter 1 for details.

Based on the same principle that in Section 1.4.3, N_e particles gives realization of the model state variables, x , with $\{\mathbf{x}_1, \mathbf{x}_2, \dots, \mathbf{x}_m\}$ and are sampled from the probability density $p(\mathbf{x}) \sim \sum_{i=1}^m w_i \delta(\mathbf{x} - \mathbf{x}_i)$, which approximates the exact target density. Each state in $\{\mathbf{x}_i, i = 1, \dots, N_e\}$, gives a model representation to be compared with an observation $\{y_i, i = 1, \dots, N_y\}$, N_y being the number of observations. For the model state vector \mathbf{x} , we evaluate the model $\mathcal{M}(\mathbf{x})$ and map it to observations \mathbf{y} via the observation operator \mathcal{H} :

$$\mathbf{y} = \mathcal{H}[\mathcal{M}(\mathbf{x})] + \epsilon, \quad (2.1)$$

where ϵ represents the measurement error, and in this chapter, \mathcal{M} is the forward model, representing the physics of the process without time evolution. To estimate the probability density function of the state variables x , the particle method uses Bayes' theorem (Sec. 1.4.2, Eq. (1.28)). With importance sampling (Sec. 1.4.3), we use discrete samples of \mathbf{x} to generate the prior $p(\mathbf{x})$, and we compare the model predictions $\mathcal{M}(\mathbf{x})$ with the observations \mathbf{y} through the likelihood $p(\mathbf{y}|\mathbf{x})$. The posterior distribution $p(\mathbf{x}|\mathbf{y})$ is calculated by weighting each particle with weights

$$w_i = \frac{p(\mathbf{y}|\mathbf{x}_i)}{\sum_{j=1}^{N_e} p(\mathbf{y}|\mathbf{x}_j)} \quad (2.2)$$

In Eq. (2.2), the posterior weights are normalized with $\sum_{j=1}^{N_e} w_j = 1$. The expected value of the posterior distribution is an estimator of the state variable values, and we use $\hat{\mathbf{x}}$ to refer to the “analysis”, i.e., the posterior quantity in the state space. The quality of the posterior depends on the ensemble size, N_e , as well as the dimension of the state- and observation spaces (Evensen et al., 2022). Moreover, the uncertainty in the analysis depends on the uncertainty in $p(\mathbf{x})$ and in the observations. Section 2.4 introduces the entropy concept to quantify the posterior distribution's quality. The entropy, $H(x)$, is minimal if a variable x_i can be estimated with zero uncertainty from $p(\mathbf{x})$, with the probability $p(x_i) = 1$. Conversely, the entropy is maximal and equal to $H(x) = \log(N_e)$, if there is equal probability between N_e variables, with $p(x_i) = 1/N_e$.

2.2.2. WEIGHT COLLAPSE IN THE PARTICLE METHOD

We define the efficacy of importance sampling to estimate the state vector as the ability to get a posterior distribution representing the prior and the likelihood as formulated in Bayes' theorem (Sec. 1.4.2 Eq. (1.28)). As in any sampling method, the posterior mean becomes a better estimator of the state vector as the number of samples and, hence, the ensemble size increases. If a given ensemble size is insufficiently large to sample the prior, we can observe a collapse of the weights in the posterior (Eq. (2.2)). Weight collapse occurs when one single particle has almost all the weight in estimating the posterior mean. In this case, the maximum weight, w_{max} , of all the particles converges to one. Collapse occurs sooner when the dimensions, N_x , and N_y increase unless the ensemble size increases exponentially as well (Bengtsson et al., 2008; Beskos et al., 2014; Beskos et al., 2017).

Previous results of Snyder et al., 2008 and Bengtsson et al., 2008 give an indication of the applicability of importance sampling, more specifically the particle filter, for a given ensemble size at the asymptotic limit. This asymptotic limit gives the asymptotic condition for collapse for large ensemble size and large number of observations.

In the following, we briefly review the asymptotic theory. For details, we refer the reader to Snyder et al., 2008 and Bengtsson et al., 2008. The theory of the asymptotic limit is applicable for a case with an i.i.d. prior state vector \mathbf{x} and observation error ϵ , and with an Identity (I_d) observation operator \mathcal{H} . If we assume the prior state vector, \mathbf{x} , and model $\mathcal{M}(\mathbf{x})$, in the one-component model to be i.i.d, we can apply the asymptotic limit to evaluate the required ensemble size. To compare and understand how weight collapse occurs in the multi-component model with spatial correlation, we address the following question:

Can we identify the required ensemble size and maximum weight w_{max} , for which importance sampling is practically applicable?

We start with the assumption of standard normal density for the prior and the likelihood to derive a theoretical relationship between the required ensemble size, N_e , and the dimension N_y .

To derive this relationship, Snyder et al., 2008 approximate the likelihood of one particle, $p(\mathbf{y}|\mathbf{x}_i)$, as the product of the likelihoods over the observation vector, for an I_d observation operator and with i.i.d. prior state variables and observations error ϵ .

$$p(\mathbf{y}|\mathbf{x}_i) = \prod_{j=1}^{N_y} f [y_j - (\mathcal{H} \cdot \mathcal{M}(\mathbf{x}_i))_j]. \quad (2.3)$$

In Eq. (2.3), for a given observation j , $(\mathcal{H} \cdot \mathcal{M}(\mathbf{x}_i))_j$ is the model prediction from the particle \mathbf{x}_i seen at the observation point j and f is a standard normal density function $f \sim N(0, 1)$. The expression of the likelihood in Eq. (2.3) can be simplified and expressed as a Gaussian distribution, $N(\mu, \tau)$ by defining a re-scaled mean μ and variance τ . To do this, we define a log likelihood V_{ij} using $\Psi() = \log f()$ as follows,

$$V_{ij} = -\Psi [y_j - (\mathcal{H} \cdot \mathcal{M}(\mathbf{x}_i))_j], \quad (2.4)$$

where, using the expression of the log likelihood V_{ij} in Eq. (2.4), the expression of the likelihood in Eq. (2.3) can be rewritten as a re-scaled likelihood of $p(\mathbf{y}|\mathbf{x}_i)$

$$p(\mathbf{y}|\mathbf{x}_i) = \exp(-\mu - \tau S_i). \quad (2.5)$$

Here, μ is a re-scaled mean, and the variance is τ . These are defined as a function of the log-likelihood V_{ij}

$$\mu = \sum_{j=1}^{N_y} E(V_{ij}) \quad \tau^2 = \text{var} \left(\sum_{j=1}^{N_y} V_{ij} \right). \quad (2.6)$$

An important condition for the expression of the likelihood in Eq. (2.5) to be a valid approximation of the Eq. (2.3) is that the scale factor S_i can be approximated by a standard normal density $S_i \sim N(0, 1)$. From Eq. (2.5) and Eq. (2.6), we express S_i as a function of the log-likelihood, μ and τ and later verify its Gaussianity with the following expression. S_i is now

$$S_i = \left(\sum_{j=1}^{N_y} V_{ij} - \mu \right) \tau^{-1}. \quad (2.7)$$

Interestingly, Snyder et al., 2008 emphasize that in the example of a one-component model, the expression of S_i does not directly depend on the dimension, N_x , of the model state vector to be estimated.

Using the expression of the re-scaled likelihood (Eq. (2.5)) and with the approximation $S_i \sim N(0, 1)$, we can now connect the maximum weight, w_{max} , to the dimension N_y , and to the ensemble size N_e , in the case of standard normal distribution for the likelihood and the prior. With this, we find

$$E[1/w_{max}] - 1 \approx \sqrt{\frac{4}{5}} \sqrt{\frac{\log N_e}{N_y}}. \quad (2.8)$$

In this expression, the maximum weight, w_{max} , is related to S_i through Eq. (2.2). Snyder et al., 2008 use the convergence properties of a $w_{max} \rightarrow 1$ and $S_i \sim N(0, 1)$ for large N_e and N_y to derive the asymptotic expression (Eq. (2.8)). Eq. (2.8) is valid for a Gaussian prior and likelihood under the assumption of S_i converging to a Gaussian distribution.

An important result of Snyder et al., 2008 is that from Eq. (2.3) and from the expression of the log-likelihood in Eq. (2.4), the likelihood only depends on the dimension N_y , meaning that the observation dimension, rather than the state dimension, control the weight collapse. The approximation in Eq.2.5 and Eq. (2.6) are valid only if the prior distribution of state variables is close to a Gaussian distribution.

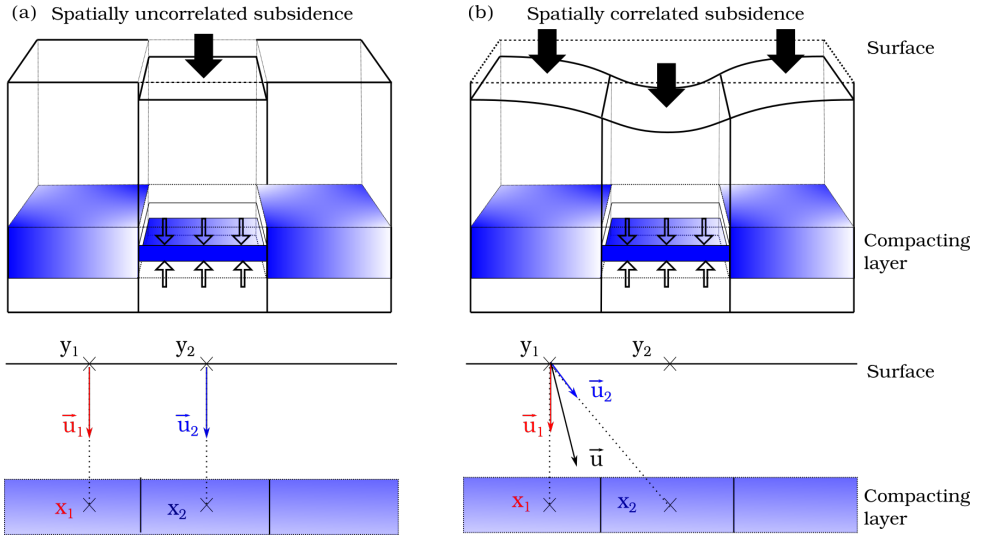


Figure 2.1: Models of subsidence. (a) One-component subsidence model and (b) the multi-component subsidence model with spatial correlation. 3D models are built with an ensemble of 1D columns. While the one-component model simulates subsidence only for the surface directly above the compartment, the multi-component model computes the deformation field as an integrated response from all compartments.

2.3. SUBSIDENCE MODELS

Subsidence can occur due to reservoir compaction, which is a decrease in reservoir thickness due to a pressure variation due to, for example, gas production. When faults or different rock compositions compartmentalize reservoirs, the reservoir may compact more strongly in certain areas. We discretize the reservoir into $5.5 \text{ km} \times 5.5 \text{ km} \times 240 \text{ m}$ cuboid-shaped elements, with a constant reservoir thickness of 240m (Tab. 2.1). In the following, we will use the term *compartment* to refer to reservoir elements. These could be geological reservoir compartments or volumes within the reservoir with the same reservoir property. As a simplification, we first simulate the compaction of each compartment without the created subsidence affecting the surface above other compartments. This is illustrated in Fig. 2.1a with the “one-component model”. In contrast to the one-component model, Fig. 2.1b shows spatially correlated subsidence created from the cumulative effect of the compaction in all compartments. To create this spatially correlated subsidence, we use the “multi-component model”, in the sense that the resulting subsidence is a linear combination of all pressure variations. A commonly used subsidence model due to pressure variation is the nucleus of strain approach of Geertsma, 1973; Muñoz and Roehl, 2017; Tempone et al., 2010. The nucleus of strain represents a compaction of a reservoir compartment as a point source of pressure variation, ΔP . The analytical solution of the vertical displacement at the surface ($z = 0$) created by a single nucleus of strain is

$$u_z(r, 0) = \frac{-C_m(1 - \nu)V\Delta P}{\pi} \frac{D}{(r^2 + D^2)^{3/2}}, \quad (2.9)$$

where r is the horizontal distance between an observation point at the surface and the vertical of a nucleus of strain at a depth D and with the compaction coefficient of the reservoir, C_m , the Poisson ratio ν and the volume V of the reservoir, the pressure variation ΔP . In the data assimilation experiment with this subsidence model, the pressure variation ΔP for each compartment, $\mathbf{x} = \{\Delta P_i, i = 1, \dots, N_x\}$ are the unknown variables that are being estimated. These variables form the state vector.

2.3.1. ONE-COMPONENT MODEL OF SUBSIDENCE

The one-component model gives a first approximation of the subsidence caused by the pressure variation (and associated reservoir compaction) and does not take into account the spatial correlation in the subsidence field. To build this model, we start with a 1D geometrical approximation of subsidence (Fig. 2.1a), and we create adjacent and independent compartments at the reservoir depth with Eq. (2.9). This gives a discretization of 1D columns of subsurface with the reservoir layer and a $5.5 \text{ km} \times 5.5 \text{ km}$ resolution for subsidence at the Earth's surface (Fig. 2.1). Because we don't include spatial correlation in the one-component model, an observer at one point only sees the compaction in the reservoir compartment directly below (Fig. 2.1), resulting in the horizontal distance r of the nucleus of strain to the observation point, $r = 0$, such as that we have a vertical displacement $u_z(r = 0, 0)$.

In this case, the model \mathcal{M} represents a mapping from a pressure variation of the reservoir to a vertical displacement of the surface with a one-to-one relationship between pressure variation state variables and subsidence. The model state variables are independent; hence, the subsidence values associated with each compartment are also independent, resulting in an uncorrelated subsidence field. The number of columns gives the model resolution, which, in our case, defines the dimension of the state and the observation space. This model is similar to the example in Snyder et al., 2008 with an I_d observation operator, $\mathcal{H} = I_d$.

2.3.2. MULTI-COMPONENT MODEL OF SUBSIDENCE

The one-component subsidence model computes a local displacement caused by a single nucleus, and the resulting subsidence field does not include the response from the entire compacting reservoir. As an alternative, the nucleus of strain approach can model an arbitrarily shaped reservoir (Candela et al., 2019; Muñoz and Roehl, 2017; Tempone et al., 2010) by linearly adding the effect of each nucleus k to the total displacement field

$$\mathbf{u}_z(r, 0) = \sum_{k=1}^{N_x} \mathbf{u}_{z,k}. \quad (2.10)$$

The geometry of the multi-component model is similar to the one-component model of subsidence, with a nucleus of strain in the center of each reservoir compartment. We compute the subsidence (Eq. (2.9)) by calculating the influence of the nucleus of strain over the volume, V , of the reservoir compartment (Geertsma and van Opstal, 1973). The difference with the one-component model is that the surface displacement u_z at one location j in space arises from all sources of strain in all reservoir compartments

(Fig. 2.1b). Therefore, \mathcal{M} transforms pressure variation to subsidence, creating a spatially correlated subsidence field at the surface. The spatial correlation in the multi-component model thus implies that the model $\mathcal{M}(\mathbf{x})_j$, computed for an observation point j from the state vector \mathbf{x} can be written as

$$(\mathcal{M}(\mathbf{x}))_j = \sum_{k=1}^{N_x} m_{jk} x_k, \quad (2.11)$$

where m_{jk} is the jk^{th} element of the model matrix. Recall that the multi-component model integrates the responses of all compartments and thus is not a one-to-one transformation from the pressure variation to the subsidence (i.e., it is a non-injective transformation), and, in this case, an observation j is linearly dependent to all $k = 1, \dots, N_x$ components of the state vector. As described in Eq. (2.1), the observation operator remains $\mathcal{H} = I_d$ as in the one-component model, assuming that the measurement method is the same. In the following, we use these two subsidence models to investigate the effect of spatial correlation in weight collapse. The pressure variation, the compartment size, and the thickness are modeled after the Groningen gas reservoir in the Netherlands (Tab. 2.1). The mechanical properties are also taken from this reservoir (Tab. 2.2). In the following, we estimate the pressure variation in each of the

Table 2.1: Pressure variation, compartment size and thickness of the multi-component model.

	ΔP	dx	dy	dh
Nucleus of strain	-0.35 MPa	0.05°	0.05°	240 m

Table 2.2: Reservoir properties.

Parameter	Symbol	Value	Unit
Depth	D	2800	m
Thickness	h	240	m
Poisson ratio	ν	0.32	-
Compaction coefficient	C_m	1×10^{-10}	Pa^{-1}

compartments using observations of subsidence, defining the state vector with $\{\mathbf{x}_k, k = 1, \dots, N_x\}$, N_x being the number of compartments and thus the state space dimension. We set the number of observations N_y , equal to the number of state variables to test the particle method with the two models of subsidence at the asymptotic limit (Sec. 2.2.2) and the agreement with the theoretical derivation of weight collapse from Snyder et al., 2008.

2.3.3. SYNTHETIC EXPERIMENTS FOR SUBSIDENCE MODELS

With synthetic data assimilation experiments, we can assess the efficacy of the particle method to estimate an unknown quantity. The state vector \mathbf{x} of dimension N_x represents the unknown pressure variation, ΔP , that we want to estimate for each grid cell of

the reservoir. A reservoir pressure variation ΔP creates reservoir compaction and subsidence. We simulate this by applying the forward model operator, \mathcal{M} , and with data assimilation, we update the distribution of the state variables ΔP given subsidence observations \mathbf{y} . Both state and observation vectors \mathbf{x} and \mathbf{y} have values spatially distributed over a regular grid and have the same dimension $N_x = N_y$. The pressure variation and subsidence can vary in time, usually involving a dynamical forward model \mathcal{M} . In the study, we test the method over a one-time step update of the state ΔP considering a quasi-static case. To do this we define a "true" value of state variables, \mathbf{x}^{truth} and sample values from this truth to generate synthetic observations for assimilation $\tilde{\mathbf{y}}$, $\{\tilde{y}_i, i = 1, \dots, N_y\}$ with Eq. (2.1). We use the notation $\tilde{\mathbf{y}}$ to define synthetic observations and avoid confusion with the vector observations, \mathbf{y} , in Eq. (2.1). The observation operator \mathcal{H} maps the true state vector \mathbf{x}^{truth} to the synthetic observations $\tilde{\mathbf{y}}$ and Gaussian noise, ϵ , is linearly added to simulate imperfect observations:

$$\tilde{\mathbf{y}} = \mathcal{H} \left[\mathcal{M}(\mathbf{x}^{truth}) \right] + \epsilon. \quad (2.12)$$

We use the observation operator \mathcal{H} , applied to the forward modeling operator \mathcal{M} , to compute the model prediction of subsidence from the pressure variation. Note that we use $\mathcal{H} = I_d$ in the example with synthetic experiments. However, \mathcal{H} could differ given the origin of the empirical data, e.g., leveling or InSAR techniques. We compare the outcome of synthetic experiments with the "true" values of state variables and subsidence estimates as an indication of the efficacy of the importance sampling. We expect a different required ensemble size, N_e , larger for the multi-component model than for the one-component model. To understand this, let's assume that the one-component model requires N_e Monte Carlo samples to solve N_y independent equations of 1 variable each. One particle is then a vector of N_y values, and we solve a system of N_y independent equations, which is relatively straightforward. Now, if the N_y equations each contain linear combinations of all N_y variables, as in the multi-component model, the equations are no longer independent, and it becomes more difficult to solve this problem with N_y samples. Therefore, we expect the ensemble size, N_e , to increase when the subsidence in one location depends on pressure variations in other locations, as is the case in the multi-component model.

2.4. ENTROPY AND MUTUAL INFORMATION

We investigate weight collapse in data assimilation problems with spatially correlated observations using the information theory of Shannon (Shannon, 1945), which is commonly applied in probability theory in the field of dynamical systems (Jost, 2005). The measure of entropy quantifies the uncertainty and, thus, the information about an unknown quantity. Fowler and van Leeuwen, 2012, 2013; van Leeuwen, 2003; Yustres et al., 2012 demonstrate using information theory and mutual information in Bayesian estimation problems. Nearing et al., 2013 further use entropy and mutual information to evaluate the efficiency of a data assimilation method. For a particle method, sources of uncertainty are model error, imperfect data, and the approximation in the importance sampling algorithm, which all propagate into the posterior distribution. The importance sampling algorithm assumes that we can adequately sample the prior.

However, weight collapse can occur if the sampling is inadequate, for example, because of non-independent or insufficient samples. In this case, the expected mean of the posterior is no longer a good representation of the true posterior (Chap. 1 Sec. 1.4.3 Eq. (1.28)). This implies a loss of information in the posterior estimate. We use the metric of entropy and mutual information to evaluate the propagation of information from prior and likelihood to posterior, as defined in Nearing et al., 2018 and Brewer, 2017. Mutual information describes how much information two arguments have in common, similar to a correlation between two random variables normally distributed. For example, it can give the common information between the random variable x contained in the distribution $p(\mathbf{x})$, representing the model state variables and the data for assimilation \mathbf{y} , with distribution $p(\mathbf{y})$ (Fig. 2.2). Using mutual information in data assimilation problems allows us to evaluate how the information before assimilation is conserved in the posterior. For a state variable x sampled from a discrete distribution $p(\mathbf{x})$, the entropy $H(x)$ of $p(\mathbf{x})$, can be interpreted as "can we know x given $p(\mathbf{x})$ " and is expressed by

$$H(x) = -\sum_i p(x_i) \log(p(x_i)). \quad (2.13)$$

Let us introduce random variables x , y , and z . In assimilation problems, we have

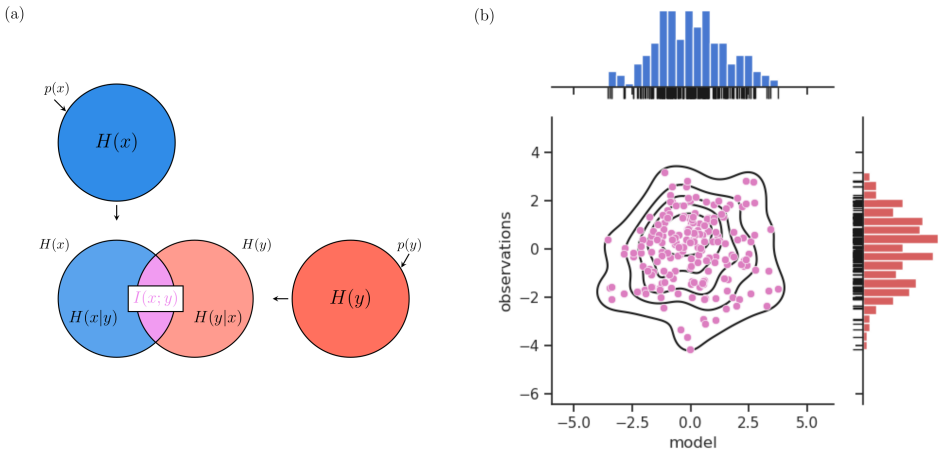


Figure 2.2: Venn diagram to illustrate the metric of entropy before assimilation. (a) The colored area in the circle represents the entropy of a distribution (e.g., entropy $H(x)$ of the prior distribution $p(\mathbf{x})$). In this drawing, the intersection of the entropy of prior and data visualizes the mutual information $I(x; y)$. The remaining area of entropy (e.g., $H(x|y)$) represents the reduced uncertainty on the variable x given the knowledge brought by the variable y . (b) Joint probability gives an intuitive approach to mutual information as a measure of similarity between probability distributions. In the example with discrete Gaussian distributions for the prior and the data, if the joint probability shows a strong correlation, then the mutual information increases as the joint probability increases (Eq. (2.14)).

samples of the model predictions, \mathbf{x} , and we have the observation vector \mathbf{y} for the assimilation (Eq. (2.1)). In the case of a synthetic experiment, the analysis can be compared with the truth. However, in realistic data assimilation problems, we don't know the truth, and therefore, to test the performance of the data assimilation, we

compare the analysis with independent observations, which we refer to as validation data. Let us assume that \mathbf{z} is a vector of validation data of dimension N_y . By construction, observation vectors \mathbf{y} and \mathbf{z} are sampled from the same density, $N(0, 1)$, and the same observation model (Eq. (2.1)). We assume them to be independent. $H(x)$ is the entropy in the model, and it measures the uncertainty on the model predictions \mathbf{x} . Similarly, for the entropy in a data set, we can compute $H(y)$, from observations $\{y_i, i = 1, \dots, N_y\}$ with Eq. (A.2).

We can now compute the mutual information $I(z; x)$ between $p(\mathbf{z})$ and $p(\mathbf{x})$

$$I(z; x) = \sum_{\mathbf{z}} \sum_{\mathbf{x}} p(\mathbf{x}, \mathbf{z}) \log \left(\frac{p(\mathbf{z}, \mathbf{x})}{p(\mathbf{z})p(\mathbf{x})} \right). \quad (2.14)$$

In Eq. (2.14), the prior distribution $p(\mathbf{x})$, of the model predictions $\mathcal{M}(\mathbf{x})$, is compared with the validation data \mathbf{z} , using the joint probabilities $p(\mathbf{z}, \mathbf{x})$.

As mentioned in Section 2.3.2, the state and the observation spaces have the same dimension, $N_x = N_y$. Thus, the vector of the model prediction has the dimension of N_x . A more practical computation of the mutual information (Paninski, 2003), written as a function of the entropy and the joint entropy $H(z, x)$ is

$$I(z; x) = H(x) + H(z) - H(z, x). \quad (2.15)$$

Also, Eq. (2.15) can be applied to estimate the mutual information $I(z; y)$. $I(z; x)$ and $I(z; y)$ now give an indication of the information content in the model variable x and the assimilated data y , which can be used to evaluate a certain data-assimilation setup. By quantifying the propagation of information content before and after assimilation, we can relate weight collapse to the importance sampling performance and, therefore, evaluate the required ensemble size given the model complexity.

To evaluate how the information content before assimilation propagates to the posterior, we define the differential information I_{diff} and the data assimilation efficiency \mathcal{E}_{DA} (Nearing et al., 2018). The differential information is the difference between the mutual information in the posterior and the prior and is expressed as $I_{\text{diff}} = I(z; \hat{x}) - I(z; x)$. This quantity can be negative if the particle method *corrupts* the prior information available before assimilation (e.g., in the model or in the observations). We define the data assimilation efficiency \mathcal{E}_{DA} to describe how the prior and observation information is conserved in the posterior distribution. \mathcal{E}_{DA} is the ratio of the posterior mutual information $I(z; \hat{x})$ and the total information in model and observations $I(z; x, y)$,

$$\mathcal{E}_{DA} = \frac{I(z; \hat{x})}{I(z; x, y)} \quad (2.16)$$

The posterior mutual information represents the mutual information between the distribution of the validation data $p(\mathbf{z})$ and the analysis estimate, evaluated from the posterior weighted ensemble $p(\hat{\mathbf{x}})$. The total information in model and observation $I(z; x, y)$ represents the information available before assimilation and is expressed as a function of the mutual information $I(z; \hat{x})$ and of the mutual conditional information $I(z; y|x)$:

$$I(z; x, y) = I(z; x) + I(z; y|x). \quad (2.17)$$

$I(z; y|x)$ is the information that z and y have in common conditioned on the prior $p(\mathbf{x})$ and can be calculated as follows to derive \mathcal{E}_{DA} :

$$I(z; y|x) = \sum_x \sum_y \sum_z p(\mathbf{x}, \mathbf{y}, \mathbf{z}) \log \left(\frac{p(\mathbf{y}|\mathbf{z}, \mathbf{x})}{p(\mathbf{y}|\mathbf{x})} \right). \quad (2.18)$$

The Posterior quantity of mutual information is computed similarly to that of the prior information in Eq. (2.15). The entropy of the posterior distribution $p(\mathbf{x}|\mathbf{y})$ is proportional to the weights $w_i \log(w_i)$, and can be derived in the discrete case with the approximation of

$$p(\mathbf{x}|\mathbf{y}) = \sum_{i=1}^{N_e} w_i \delta(x - x_i)$$

and the expression of the updated weights in Eq. (2.2). A maximum entropy represents a maximum uncertainty on the analysis \hat{x} , and likewise, a decreasing entropy suggests a decreasing uncertainty. Quantities of mutual information are empirically estimated with histogram estimation methods. Algorithm 1 gives a pseudo algorithm to evaluate the prior information before assimilation $I(z; x)$ (Eq. (2.15)) and the posterior information $I(z; \hat{x})$. Other quantities of mutual information are computed in the same manner.

Algorithm 1 Derivation of the mutual information in synthetic experiments

1) Prior information $I(z; x)$

→ Sample $N_x = 50$ state variables of pressure variation x_i

→ Compute subsidence at $N_y = 50$ observation points $x_i = \mathcal{M}(x_i)$

→ Generate a synthetic observation vector of dimension $N_y = 50$ with $\tilde{y}_i = \mathcal{H}[\mathcal{M}(x_i^{truth})] + \epsilon$ and the validation data $\tilde{z}_i = \mathcal{H}[\mathcal{M}(x_i^{truth})] + \epsilon$.

for $n = 1 : nbin$ **do**

 Create histograms of x and \tilde{z} , $nbin$ being the number of bins

 Compute the probability of $p(x)$, $p(\tilde{z})$

 Evaluate the entropy of $H(x)$, $H(\tilde{z})$

end for

→ Compute the mutual information $I(\tilde{z}; x)$ with Eq. (2.15).

2) Posterior information $I(\tilde{z}; \hat{x})$

for $n = 1 : nbin$ **do**

 Create the histogram of x given the weight vector from the assimilation and get $p(\hat{x})$ per bin.

end for

→ Compute $I(\tilde{z}; \hat{x})$ in the manner of Eq. (2.15).

2.5. SUBSIDENCE STATE ESTIMATION

2.5.1. WEIGHT COLLAPSE AND ASYMPTOTIC LIMIT FOR SUBSIDENCE MODELS

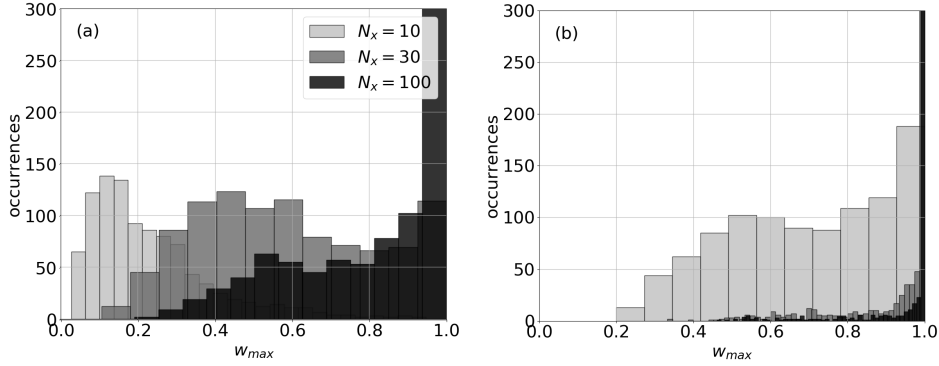


Figure 2.3: Maximum weight w_{max} for the one-component model of subsidence (a) and for the multi-component model of subsidence with spatial correlation (b) from simulations with $N_x=[10, 30, 100]$ state variables and an ensemble size $N_e = 1000$. In those experiments, $N_x = N_y$ and histograms of w_{max} are computed over 1000 simulations.

We observe a stronger weight collapse in the case of spatial correlation in the observation field. Figure 2.3 illustrates the weight collapse in the posterior distribution in the subsidence models of this study. The histograms show the distribution of the maximum weight w_{max} , for both the one-component and multi-component subsidence models and for a model dimension of $N_x = [10, 30, 100]$. The experiment is repeated 1000 times for a consistent estimation. The maximum weight can be used as an indicator of the importance sampling performance. It shows that the method performance can rapidly decrease with spatially correlated observations if the ensemble size is inadequate. To evaluate weight collapse in the case of spatial correlation and an increasing dimension of the state, N_x , and observations spaces, N_y , we test the particle method at the asymptotic limit (Eq. (2.8)). We perform experiments with both the one-component and the multi-component models with a large number of observations $N_y = [600, 800, 1000, 1200, 1400, 1600, 1800, 2000]$. In each experiment, we assimilate synthetic subsidence observations into ensembles with $N_e = N_y^n$ with $n = [0.75, 0.875, 1.0, 1.25]$. Not surprisingly, the results of the one-component model (Fig. 2.4a and b) show a good accordance between simulations and the theoretical prediction of $E[1/w_{max}]$ from Eq. (2.8). The relationship in Eq. (2.8) allows a linear relationship to connect the maximum weight w_{max} to the ensemble size N_e and the number of state variables N_x . A linear interpolation of the results suggests that the line of $E[1/w_{max}] - 1 = -0.008 + 1.0721\sqrt{\log(N_e)/N_y}$ describes the variability of the maximum weight which exponentially depends on N_e . The particle method in the one-component subsidence model shows good agreement with the results of Snyder et al., 2008. However, it clearly appears that the particle method in the multi-component model does not fit the

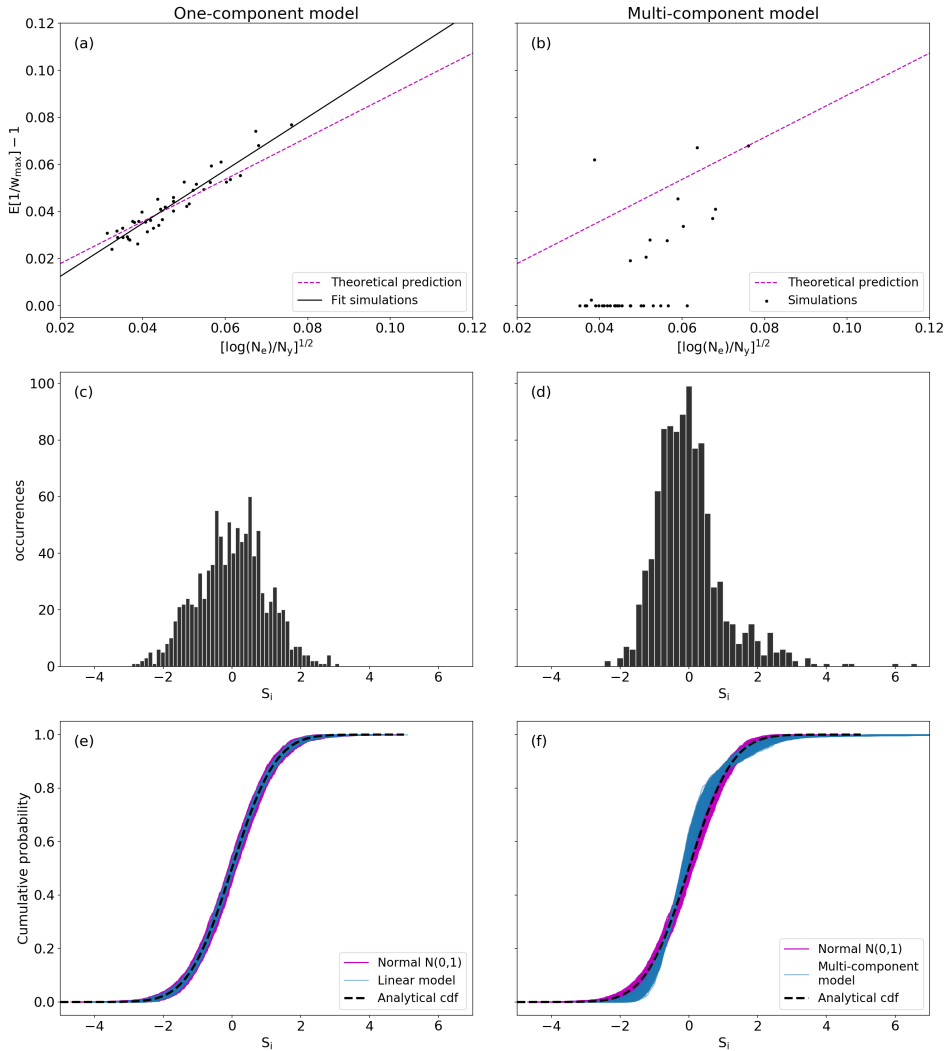


Figure 2.4: Results at the asymptotic limit for the one-component model of subsidence and the multi-component model. Verification of the condition for collapse ((a), (b)). The dashed line gives the theoretical prediction of Eq. (2.8), and the solid line gives the best fit to the simulations given N_x ($N_x = N_y$) and N_e . The histograms of the distribution of the scale factor S_i from the re-scaled likelihood in Eq. (2.7) ((c), (d)). In (e) and (f), Kolmogorov-Smirnov (K-S) tests of the distribution of S_i show the cumulative probability distributions over 1000 simulations with 1) a sampled standard normal density $N(0,1)$, 2) the subsidence model and in dashed line the analytical cumulative probability of a density $N(0,1)$.

theoretical prediction of Eq. (2.8). The main difference between the one-component model and the multi-component model is reflected by the negative log-likelihood (Eq. (2.4)) that results from the summation in the model operator \mathcal{M} (Eq. (2.11)). If we assume a Gaussian density for the expression of the negative log-likelihood in the one-component model

$$V_{ij} \propto \frac{1}{2} \frac{[y_i - (\mathcal{H}[\mathcal{M}(\mathbf{x}_i)])_j]^2}{\sigma^2}, \quad (2.19)$$

this becomes

$$V_{ij} \propto \frac{1}{2} \frac{[y_j - \mathcal{M}(x)_{ij}]^2}{\sigma^2}. \quad (2.20)$$

In the case of spatial correlation, the expression of the negative log-likelihood differs as we consider the linear combinations of state variables (Eq. (2.11)). Because of the mapping from the model input to the model output reflected by \mathcal{M} , the log-likelihood depends on the state space dimension N_x (Eq. (2.21)) in the case of spatial correlation. This can be explained by the fact that in the case of spatial correlation, we consider the differences between the vector observation y_j with the model computed from all model state variables.

$$V_{ij} \propto \frac{1}{2} \frac{[y_j - \sum_{k=1}^{N_x} m_{jk} \cdot x_{ik}]^2}{\sigma^2}. \quad (2.21)$$

To assess how the weight collapse in the assimilation with the multi-component model (Eq. (2.21)) differs from the theoretical prediction of weight collapse in Eq. (2.8), we test the approximation of the observation likelihood in Eq. (2.5) against the probability distribution of the term S_i in Eq (2.7). The term S_i is the scale factor that allows us to express the re-scaled likelihood (Eq. (2.3)) as a Gaussian distribution. The main assumption to re-scale this likelihood is that S_i follows a standard normal density, $S_i \sim N(0, 1)$.

The histograms in Fig. 2.4 show the distributions of S_i in the one-component and the multi-component model. The distribution of S_i in the multi-component model shows a skewness compared to the result for the one-component model, which approaches a standard normal distribution. Distributions of S_i provide evidence of the effect of state variables dependency in Eq. (2.21) (Slivinski and Snyder, 2016).

The histograms in Fig. 2.4 show the result of S_i for a single simulation. To confirm the deviation to a standard normal density in the distribution of S_i , we perform the K-S (Kolmogorov-Smirnov) tests over 1000 simulations.

The analytical cdf (cumulative density function) of the standard normal distribution and the cdf of sampled distributions from the standard normal density, $N(0, 1)$ are first compared to evaluate the spread around the analytical solution (Fig. 2.4e and f), due to the sampling. For a dimension $N_x = N_y = 1000$ and the ensemble size of $N_e = 1000$, we compute the value of S_i (Eq. 2.7) and compare to the analytical and sampled cdf. We choose the values of N_x , N_y , and N_e to perform simulations of S_i at the asymptotic limit in a regime where Eq. (2.8) is valid.

Results in Fig. 2.4e and Fig. 2.4f show a very good overlap of the cdf for the one-component model for both the sampled distributions and the S_i distributions. K-S

tests confirm the main assumption that S_i is approximately normal in the case of the one-component model of subsidence.

The K-S test for the multi-component model exhibits a skewness in the cdf of S_i , corresponding with the deviation from a standard normal density in the histogram (Fig. 2.4d). We have computed the K-S test statistic and the p-values between two distributions for the cases: Gaussian/Gaussian, Gaussian/ S_i one-component, and Gaussian/ S_i multi-component. The result is an average of the comparison of the S_i distribution against 1000 Gaussian distributions: Results show a lower p-value

Table 2.3: K-S test results of the S_i distribution in the one-component and the multi-component model. S_i distributions are compared to Gaussian distributions and average over 1000 simulations.

	KS statistic	p-value
Gaussian	0.032	0.66
S_i : one-component	0.034	0.60
S_i : multi-component	0.095	0.015

for the multi-component model than for the one-component model, confirming the deviation from the Gaussian distribution. Most p-values are below the threshold of 0.05, usually taken as a resemblance criterion. This implies that the Gaussian approximation of S_i is invalid in the multi-component model. Results with the multi-component model thus suggest that S_i can not always be approximated by a standard normal distribution when the observations are spatially correlated and consequently when the log-likelihood explicitly depends on the state dimension, N_x in Eq. (2.21). Implications of non-Gaussian S_i are that 1) the re-scale likelihood in Eq. (2.5) is not a valid approximation and 2) the relationship between the maximum weight and the required ensemble size is not linear (Fig. 2.4a and b). With these empirical results, we highlight a limit of the analytical derivation of the required ensemble size in a spatially correlated data assimilation problem.

2.5.2. ENTROPY AND MUTUAL INFORMATION FOR SUBSIDENCE MODELS

With $H(z)$ being the uncertainty about a set of observations, with the metric of mutual information, we evaluate the information content in the model, $I(z; x)/H(z)$, and in the data $I(z; y)/H(z)$ that resolves the uncertainty on z . We apply the same methodology for both the one-component and the multi-component model. With synthetic data assimilation experiments, we compute the entropy and the mutual information with a histogram method. The histogram method requires a sufficient sample size to evaluate the probability of the sample into bins. The sample size in this simulation is the number of model predictions, N_x , and the number of observations N_y , respectively, for $I(z; x)/H(z)$ and $I(z; y)/H(z)$. The binwidth is chosen such that the histogram covers the range of subsidence values (e.g., for both model predictions and synthetic observations). For our experiments with the dimension of $N_x = N_y = 50$, sensitivity tests on the robustness of the histogram method led us to choose a bin resolution of 0.5mm to create histograms of subsidence. Table 2.4 shows the mutual information for the one-component and the multi-component model before the assimilation. The

Table 2.4: Prior information content in model and data with a bin resolution of subsidence of 0.5 mm and 40 bins for $N_x = N_y = 50$.

	One-component	Multi-component
$I(z; \mathbf{x})/H(z)$	0.76	0.76
$I(z; \mathbf{y})/H(z)$	0.76	0.77
$w_{max}(N_e = 10^3)$	0.71	0.94

information content in both the model and in the data is 0.76. The one-component and the multi-component models have similar information content before assimilation, which is unsurprising, as both have been sampled from the same Gaussian distribution. We chose a relatively small $N_x = N_y$ of 50, which is sufficient to ensure we avoid ensemble collapse. This ensemble size is used to reproduce the results of entropy and mutual information with the histogram estimation, and we keep the same $N_x = N_y$ of 50 in this study to compare results. The importance sampling experiments are performed

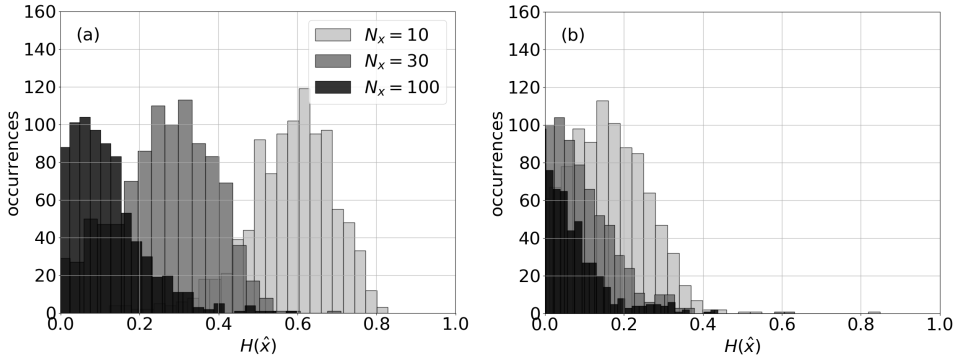


Figure 2.5: Posterior entropy for the one-component model and b the multi-component subsidence model for the dimension $N_x=[10, 30, 100]$ and 1000 ensemble members. Histograms of entropy (Eq. (A.2)) applied to the weighted posterior probability distribution. The entropy is computed and averaged over 1000 simulations.

for an ensemble size $N_e = 1000$. As expected from histograms of w_{max} in Fig. 2.3, the weight collapse is stronger in the multi-component model than in the one-component model (Tab. 2.4) as the dimension increases. This suggests that the importance sampling itself is the main cause of information loss in the posterior in case of weight collapse. The posterior entropy, $H(\hat{\mathbf{x}})$ in Fig. 2.5, which represents the uncertainty on the vector of state variables \mathbf{x} , after the assimilation in the posterior distribution $p(\mathbf{x}|\mathbf{y})$, is computed for the dimensions $N_x = [10, 30, 100]$. Comparing Fig. 2.5 with Fig. 2.3, we observe that the posterior entropy decreases as the maximum weight increases. Comparison of Fig. 2.5b with Fig. 2.5a shows that the posterior entropy converges faster to zero in the case of a model with correlation than in the case of the one-component model. Similarly to the maximum posterior weight in Fig. 2.3, the entropy decreases as the dimension increases, highlighting that both the maximal weight and the posterior entropy indicate weight collapse.

2.5.3. INFORMATION CONTENT AND EFFICIENCY

In the following, to evaluate the ability of the data assimilation algorithm to conserve information in the posterior, we use the definitions of the data assimilation efficiency \mathcal{E}_{DA} (Eq. (2.16)), and of differential information I_{diff} . According to the results of the information content before assimilation (Tab. 2.4), we compute \mathcal{E}_{DA} and I_{diff} with the binwidth of 0.5 mm and the dimensions $N_x = N_y = 50$ for an increasing ensemble size N_e . Figure 2.6 shows results of I_{diff} for the one-component and the multi-component

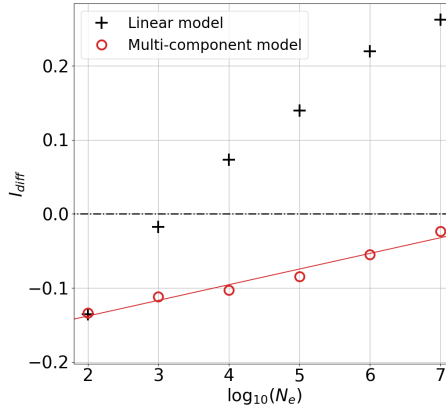


Figure 2.6: The differential information I_{diff} indicates the ability of the posterior to conserve the prior information content. The best-fit line, obtained by linear interpolation of the differential information with the multi-component model (red solid line), is given by $I_{\text{diff}} = 0.018\log_{10}(N_e) - 0.17$.

model. Results clearly show a negative I_{diff} for a small ensemble size, in agreement with a stronger weight collapse. In the example of the one-component model, $I_{\text{diff}} < 0$ for ensemble size $N_e < 10^3$ and a maximum weight $w_{\text{max}} \sim 0.7$. Differential information increases as a function of the ensemble size, N_e , for both the one-component and the multi-component model. As expected, the ensemble size of $N_e = 100$ and $N_e = 1000$ are insufficiently large to avoid weight collapse in the one-component model and give a negative differential information, I_{diff} . In this example, the information in the posterior distribution is less than in the prior. We refer to this as *corrupted* information with negative differential information. I_{diff} becomes positive for larger ensemble sizes, reflecting an increasing information content in the posterior and a respectively decreasing weight collapse.

Results of the differential information with the one-component model show good agreement with the estimation of the required ensemble size of Snyder et al., 2008 and are used as a performance benchmark for our study. Transposing this approach to the multi-component model, Fig. 2.6 shows that with an ensemble size of $N_e = 10^7$, the particle method still corrupts the prior information, with $I_{\text{diff}} < 0$ and the maximum weight approaching $\max w_i = 0.8$ (Fig. 2.7).

To evaluate the ensemble size, which preserves the prior information and then ensures the applicability of importance sampling in the multi-component model, we compare

the efficiency \mathcal{E}_{DA} with the maximum weight and the differential information I_{diff} . The

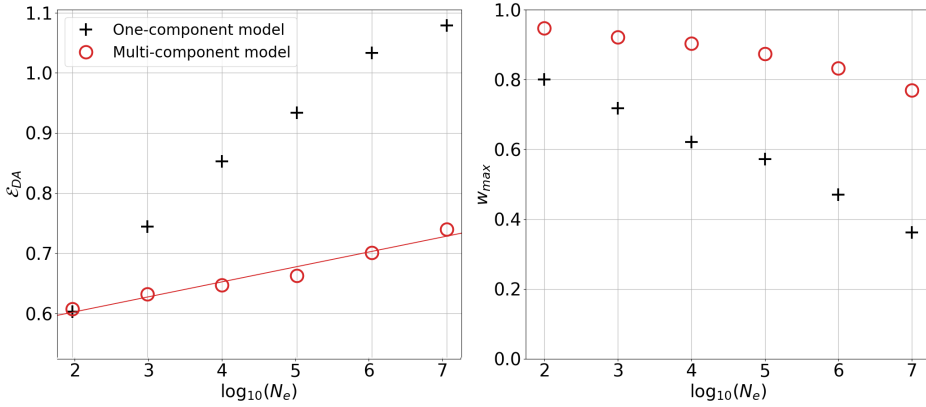


Figure 2.7: Efficiency \mathcal{E}_{DA} of the particle method for the one-component model and the multi-component model of subsidence for a dimension $N_x = 50$, and with an increasing ensemble size N_e . The best fit of \mathcal{E}_{DA} with the multi-component model is given by $\mathcal{E}_{DA} = 0.022 \log_{10}(N_e) + 0.56$.

efficiency \mathcal{E}_{DA} as illustrated in Fig. 2.7 measures the quality of the posterior given the information content in the prior model and the assimilated observations. Comparison of \mathcal{E}_{DA} with the differential information (Fig. 2.6), shows that the information in the posterior ($\mathcal{E}_{DA} \sim 0.75$) is at least equal to the prior information (Tab. 2.4) for a positive I_{diff} . An efficiency \mathcal{E}_{DA} larger than the prior information implies that the particle method conserves the prior information content. With the example of the one-component model with $N_e = 100$, the particle method does not conserve the prior information with an efficiency of $\mathcal{E}_{DA} = 0.6$ less than the mutual information before assimilation $I(z; x)/H(z) = 0.76$ (Tab. 2.4). For an increasing ensemble size $N_e > 10^4$, the particle method now conserves the prior information ($\mathcal{E}_{DA} > 0.75$) and does not corrupt the information in the posterior ($I_{\text{diff}} > 0$). This result shows that the required ensemble size should be $N_e > 10^4$, which is consistent with the previous results of Snyder et al., 2008. For equivalent ensemble sizes and equal prior information content, the efficiency in the multi-component model is less than in the one-component model. This result confirms that the importance sampling algorithm causes the loss of information when the observations are spatially correlated. For an increasing ensemble size, the efficiency becomes larger than one (Fig. 2.7a) despite the normalization. This may come from the uncertainty in the histogram method for calculating the mutual information. This could be reduced using a state dimension larger than $N_x = N_y = 50$ (i.e., model prediction or data).

Using the differential information and the efficiency \mathcal{E}_{DA} , we can evaluate the minimum required efficiency of a particle method. We consider an acceptable performance in the one-component model for a \mathcal{E}_{DA} at least equal to either the prior information in the model or in the observation. Using this approach, the differential information has a positive value at $N_e = 10^4$ with the efficiency of $\mathcal{E}_{DA} = 0.85$, which is larger than the prior information content in the model and in the data (Tab. 2.4). This then suggests $\mathcal{E}_{DA} =$

0.85 as the minimum required efficiency corresponding to $I_{\text{diff}} > 0.07$ for an ensemble size of $N_e = 10^4$.

In the multi-component model, linear interpolation in Fig. 2.7a gives an equivalent performance of $\mathcal{E}_{DA} \sim 0.85$ with an ensemble size larger than $N_e > 10^{13}$. An ensemble size of $N_e > 10^{13}$ is thus required in the example of the multi-component model to have the same performance as that in a one-component model with an ensemble size $N_e = 10^4$. Likewise, the results of I_{diff} in Fig. 2.6 suggest that we need an ensemble size larger than $N_e > 10^9$ to lift the differential information to a positive value. For I_{diff} to reach ~ 0.07 , the required ensemble size should be larger than $N_e > 10^{13}$.

Table 2.5: Required ensemble size N_e to ensure the particle method applicability in the models of subsidence based on the differential information and the data assimilation efficiency \mathcal{E}_{DA} . Experiments are performed with a bin resolution of subsidence of 0.5 mm and 40 bins for dimensions $N_x = N_y = 50$.

	one-component	Multi-component
$I_{\text{diff}} > 0$	$N_e > 10^3$	$N_e > 10^9$
$I_{\text{diff}} > 0.07$	$N_e > 10^4$	$N_e > 10^{13}$
$\mathcal{E}_{DA} > 0.85$	$N_e > 10^4$	$N_e > 10^{13}$

2.6. DISCUSSION

Setting an adequate ensemble size can prevent weight collapse in importance sampling methods in high-dimensional problems. Spatial correlation in the observed field increases the model complexity and requires importance sampling strategies with a large ensemble size. In this study, we show an example of a transformation from model input to model output involving non-i.i.d. model predicted subsidence, which requires increasing ensemble sizes to ensure the applicability of importance sampling.

As in most data-assimilation systems, the observables sample a spatially correlated field. In data assimilation methods, these non-injective transformations from the state space to the observation space are associated with spatial correlations, and depending on the strength of the correlations, the tendency for weight collapse varies. Thus, data-assimilation practitioners can expect a possible deviation from the asymptotic results of weight collapse as derived by Snyder et al., 2008. Our empirical results can help derive the required ensemble size, showing that information theory, specifically the metric of mutual information, can give empirical criteria to ensure a minimum importance sampling efficiency. The results of a so-called multi-component model at the asymptotic limit provide insights into understanding the deviation from the results of the importance sampling with the one-component model. In the first part of this study, we highlight that in the case of spatial correlation in subsidence, the approximation of the likelihood and the distribution of the scale factor S_i deviates from a standard normal probability distribution. The deviation remains small. However, the log-likelihood explicitly depends on the dimension of the state space, N_x . This could explain why the particle method in the multi-component model suffers from a stronger weight collapse than in the one-component model. In the results of Slivinski

and Snyder, 2016 with examples of nonlinear models, we observe a similar deviation at the asymptotic limit in our multi-component model, with a reservoir model that has a varying strength of compaction. Evaluating the required ensemble size N_e can be very difficult given model complexity, and this complicates the definition of a generalized methodology to evaluate N_e . We propose criteria to evaluate the required ensemble size in problems of realistic complexity involving high dimension and spatial correlation.

Information theory gives a means to quantify the information in the model and the data. It shows how this information is propagated in the posterior distribution (Nearing et al., 2013). The quality of the data assimilation estimate is often assessed with the variance of the posterior distribution or the effective sample size (Li et al., 2014; Martino et al., 2017). However, the posterior variance can be biased because of weight collapse, causing a narrow and non-representative posterior distribution. In data assimilation, applying localization is a common procedure to reduce the observation dimension and increase the posterior variance (Fowler and van Leeuwen, 2013; Luo et al., 2019; Poterjoy, 2016). A consequence of localization could be that the information of a dataset is optimized by not taking into account the redundant information. In our approach, we evaluate the bias caused by weight collapse by assessing the method performance using mutual information through the quantities of differential information and data assimilation efficiency. The differential information I_{diff} and the data assimilation efficiency \mathcal{E}_{DA} reveal that weight collapse corrupts the information in the posterior distribution, highlighting that the algorithm itself is the main cause of information loss in importance sampling.

To compute the metric of mutual information, we used the histogram method and set the sample size of model predictions and the data to $N_x = N_y = 50$ to test the sensitivity of the particle method to the ensemble size N_e . In this study, we choose the number of state variables and observations of $N_x = N_y = 50$ to have the same spread and binwidth in the histograms since we want to compare results for an ensemble size between $N_e = 100$ to $N_e = 10^7$. Increasing N_x and N_y for the histogram method would result in ensemble collapse or require an unpractical ensemble size. The one-component model of subsidence provides a means to compare the empirical results of mutual information with the theoretical background on weight collapse in the particle method (Bengtsson et al., 2008; Beskos et al., 2014; Beskos et al., 2017; Snyder et al., 2008). Mutual information results show good agreement with previous results of Snyder et al., 2008. The same methodology with mutual information could be applied to larger datasets or a time series of data in filtering and ensemble smoother methods. Weight collapse also occurs in those methods (Stordal and Elsheikh, 2015). From the result of the efficiency of the data assimilation, \mathcal{E}_{DA} , we derive by linear interpolation the required ensemble size in the multi-component model. It has been shown that the ensemble size must scale exponentially with the dimensions N_y and N_x (Bengtsson et al., 2008; Beskos et al., 2017; Snyder et al., 2008). As spatial correlation depends on the data-assimilation system, we may also expect a deviation from the linear interpolation proposed in this study. For example, \mathcal{E}_{DA} in the linear model slightly levels off, and this may suggest that the interpolated values of the required ensemble size in the multi-component model are slightly underestimated. Our approach is also interested in assessing the method performance (e.g., information loss, ensemble size) or optimizing the data assimilation

before assimilation by evaluating the information content in the prior and in the data. Other criteria to ensure the applicability of importance sampling are the maximum weight or an effective sample size of the prior ensemble. This could be a threshold for choosing the ensemble size and setting a minimum level for the required data assimilation efficacy.

However, taken alone, it is not clear how we should choose these values. Using positive differential information I_{diff} and a minimum data assimilation efficiency \mathcal{E}_{DA} , we can only obtain a first impression of what is the relevant amount of information that the posterior should contain in a specific problem.

2.7. CONCLUSION

With an example of subsidence models, we show that the main cause of performance loss in the particle method comes from the sampling strategy. By choosing a larger ensemble size, we can effectively prevent weight collapse. The required ensemble size in a problem with spatial correlation can be underestimated if evaluated based on non-representative transformation from the state to observation space. In this study, we propose two criteria based on the information theory: the differential information and the data assimilation efficiency using the metric of mutual information. This can be used to empirically derive the required ensemble size in the case of spatial correlation in the observed field. For this, we relate the weight collapse and the performance of importance sampling to the information content before and after assimilation. We find that in the one-component model of subsidence, the particle method requires an ensemble size larger than $N_e > 10^4$ for a dimension $N_x = N_y = 50$ to propagate the information available before assimilation and to obtain positive differential information. Our results show good agreement with an earlier study of Snyder et al., 2008 and provides an empirical method to measure the applicability of a data assimilation method through the differential information and the relative (i.e., relative to the prior information) criterion of the data assimilation efficiency to choose the ensemble size. This approach could be further used to track the information content in other data assimilation problems and to optimize the prior information content.

3

REDUCING WEIGHT COLLAPSE TO ASSIMILATE GEODETIC DATASETS WITH IMPORTANCE SAMPLING

The truth is rarely pure and never simple.

Oscar Wilde

Leveling and InSAR provide observation points of subsidence with a high spatial density and can be used for subsidence monitoring. Here, subsidence estimates obtained from leveling and InSAR are used in importance sampling to estimate the compaction of a gas reservoir causing subsidence. The importance sampling method is often restricted to applications with small dimensional systems, e.g., systems with few observations or states. Assimilating leveling and InSAR datasets with importance sampling in the Groningen region, which covers more than $50 \text{ km} \times 50 \text{ km}$, requires an unpractical ensemble size to ensure the importance sampling's efficiency and avoid posterior weight collapse. This chapter presents the use of a specific prior proposal density, known as the optimal proposal, in importance sampling. We present a formulation for the prior proposal density based on the results of Snyder, 2011 and Doucet et al., 2000. The implementation of importance sampling with the optimal proposal allows us to apply the importance sampling and the particle filter (in a dynamical case) to the estimation problem of subsidence caused by compacting reservoirs. The proposed particle filter implementation is tested in synthetic experiments, with actual leveling datasets with up to 500 benchmarks in the leveling network and InSAR displacement velocities with up to 1000 PS. Results suggest the possibility of applying the particle filter in the Groningen region with InSAR datasets.

3.1. INTRODUCTION

In a data-assimilation estimation problem, the physical system evolves in time from given initial conditions. The system's future states are uncertain, especially if physical processes are stochastic or chaotic (Diab-Montero et al., 2023). In data assimilation, the “past knowledge” from the model and the observations are combined for an estimation of the system's states and updates of model forecasts (Asch et al., 2016; Carrassi et al., 2022). Filtering methods such as particle filter (importance sampling in a dynamical case) give a probabilistic framework to infer the evolution of non-Gaussian and nonlinear systems (Bain and Crisan, 2009; van Leeuwen et al., 2015). The preservation of a non-Gaussian distribution makes the particle filter a suitable method for estimation problems in nonlinear systems, with a minimum assumption of prior knowledge. However, its performance decreases exponentially with the system dimension (Bengtsson et al., 2008; Snyder et al., 2008), for example, when the number of assimilated observations increases. van Leeuwen et al., 2015 address how observations can be assimilated successfully and how the number of observations relates to the ensemble size, showing that many observations (e.g., more than 10) lead to unpractical applications in meteorological systems for weather forecasts. Snyder et al., 2008 and Bengtsson et al., 2008 give a theoretical background of the particle filter applicability in a high-dimensional system and provide the posterior weight behavior at the asymptotic limit. Beskos et al., 2014; Beskos et al., 2017; Chorin and Morzfeld, 2013 also provide theoretical insight into weight collapse in the particle filter as a function of the dimension of the states vector and the observation vector. They derive criteria on the applicability of the particle filter in idealized models.

Chapter 2 illustrates how posterior weight collapse in the example of subsidence can degrade the posterior distribution more than expected from theoretical results with i.i.d. model states (Slivinski and Snyder, 2016). In subsidence applications, leveling and InSAR techniques give subsidence estimates that can be assimilated to infer subsurface properties, e.g., reservoir parameters and variables such as compaction (Gazzola et al., 2021). A leveling dataset has approximately 500 spatially distributed observations to assimilate, and the InSAR dataset gives more than 1 Million spatially distributed observations.

Particle filter methodological developments suggest that it is possible to use a particle filter with these leveling and InSAR datasets. Ades and van Leeuwen, 2013; Doucet et al., 2001; Doucet et al., 2000; Morzfeld et al., 2018; van Leeuwen, 2010 have proposed strategies to improve the importance sampling algorithm. These strategies are based, for example, on localization methods (Poterjoy, 2016) and on the use of proposal densities (Ades and van Leeuwen, 2013; Doucet et al., 2000; van Leeuwen and Ades, 2013). Results of Snyder, 2011, in a conceptual model with Gaussian distributions for model and observation errors, show that we can expect to assimilate up to 1000 observations with an ensemble size less than 10^4 .

In this chapter, we test the applicability of importance sampling to assimilate leveling and InSAR displacement velocities. In the Groningen gas field in the Netherlands, the compacting reservoir causes subsidence at the Earth's surface. Thus, the assimilation of the leveling and InSAR dataset allows us to estimate the reservoir compaction and

update the subsidence model. In these problems, the subsidence signal is typically spatially correlated and shows spatial smoothness. In Chapter 2, a basic importance sampling method could not handle a system with a spatially correlated subsidence signal without an ensemble size larger than 10^{13} . Therefore, this current chapter introduces the “optimal proposal particle filter” so we can apply particle filter for subsidence estimation in the Groningen gas field, where 1) the compacting reservoir causes spatially correlated subsidence over the entire area (Chap. 1) and 2) geodetic datasets involve large observational datasets.

The implementation is based on the so-called optimal proposal as defined in Doucet et al., 2000. In Section 1.4.3, I presented the principle of importance sampling and defined the prior proposal density with the transition density $p(\mathbf{x}^k|\mathbf{x}^{k-1})$ for a Markov process. Now, in this chapter, I give more details on how to choose this prior proposal density.

This chapter is organized as follows. In Section 3.2, I summarize importance sampling with the standard particle filter and weight collapse. In Section 3.3, I define the prior proposal density, starting with the general review of the proposal density from the book of van Leeuwen et al., 2015, allowing us to introduce an expression for the optimal proposal. In Section 3.4, I test the implementation of the optimal proposal first, with a synthetic test to show how we can reduce weight collapse before testing the method with leveling and InSAR datasets. I conclude this chapter in Sections. 3.5 and 3.6 with a discussion and conclusion.

3.2. STANDARD PARTICLE FILTER

A particle filter provides a probabilistic approach to improving knowledge about unknown or uncertain model variables and parameters using system observations. For a vector of unknown model states \mathbf{x} and an observation vector \mathbf{y} , this concept can be expressed in Bayes’ theorem (Sec.1.4.2, Eq. 1.28),

$$p(\mathbf{x}|\mathbf{y}) \propto p(\mathbf{y}|\mathbf{x})p(\mathbf{x}), \quad (3.1)$$

where the conditional probability of \mathbf{x} given \mathbf{y} is proportional to the likelihood of the observations and the prior $p(\mathbf{x})$. We refer the reader to Section 1.4.3 for more details on the principle of importance sampling.

To represent the distribution of a model state \mathbf{x} , we sample a distribution to create an ensemble of particles $\{\mathbf{x}_1, \mathbf{x}_2, \dots, \mathbf{x}_m\}$ and build a discrete probability density function $p(\mathbf{x}) \sim \sum_{i=1}^m w_i \delta(\mathbf{x} - \mathbf{x}_i)$. Each particle i is weighted given its probability to represent the model state with the weight w_i , and the Dirac δ represents a discrete sample to approximate the target PDF. The success of a particle filter in estimating the model states depends on the statistical properties of the ensemble to approximate the target PDF. With the particle filter, once particles are sampled from a probability density $p(\mathbf{x}^{k-1})$, we propagate the ensemble forward to time k , where new observations are available, using a forward model simulation. This forward propagation can be captured with the transition density $p(\mathbf{x}^k|\mathbf{x}^{k-1})$. We assume that the transition density of the model, \mathcal{M} , to

propagate the particles in time correctly. Using again Bayes' theorem and assuming that the time evolution of the states is discretized with $\mathbf{x}^{0:k} = (\mathbf{x}^0, \dots, \mathbf{x}^k)$, we can write

$$p(\mathbf{x}^k | \mathbf{y}^{0:k}) = \frac{p(\mathbf{y}^k | \mathbf{x}^k)}{p(\mathbf{y}^k)} \int p(\mathbf{x}^k | \mathbf{x}^{k-1}) p(\mathbf{x}^{k-1} | \mathbf{y}^{1:k-1}) d\mathbf{x}^{k-1}. \quad (3.2)$$

In Eq. 3.2, we recognize the propagation in time of the particles from $k-1$ to k in the transition density, $p(\mathbf{x}^k | \mathbf{x}^{k-1})$. After propagating the ensemble forward, we can perform assimilation at time k and update the weight of each particle given the difference between the model outcome and observations. According to Bayes' theorem (Eq. 1.28), the updated weight of a particle i is

$$w_i^k = w_i^{k-1} p(\mathbf{y} | \mathbf{x}_i^k). \quad (3.3)$$

Using Eq. 3.3, the particle weights are updated, and the posterior distribution's expected mean provides an estimator of the model states. In the following, we refer to Eq. 3.2 and Eq. 3.3 as the "standard particle filter". A limitation of the particle filter's application, or the application of importance sampling in general, is the so-called weight collapse; certain model realizations can give a very good fit when compared with the observations, leading to large weights for these particles. In contrast with these particles with a very large weight, most other particles have a weight close to zeros (Bengtsson et al., 2008; Snyder et al., 2008; van Leeuwen et al., 2015). This is known as weight collapse, and in case of weight collapse, the posterior PDF $p(\mathbf{x} | \mathbf{y})$ is no longer an appropriate approximation of Bayes' theorem. Weight collapse increases when the number of observations increases for a given ensemble size, making the standard particle filter difficult to apply in most geoscience applications where there are many observations available.

3.3. PROPOSAL DENSITY IN PARTICLE FILTER

The study of Doucet et al., 2001; Doucet et al., 2000; Snyder et al., 2015; van Leeuwen, 2009 gives insights into the application of the particle filter in a high-dimensional problem, and van Leeuwen et al., 2019 more recently provides an excellent review of particle filter application in high-dimensional problems. The authors show that, with adequate sampling of the observation space, weight collapse can be avoided without increasing the ensemble size. In fact, we can sample the prior states with a proposal density function using information from the data as background knowledge. Doucet et al., 2000 use the term of *optimal proposal* to refer to this prior proposal density.

3.3.1. DEFINITION OF A PROPOSAL DENSITY FUNCTION

In the standard particle filter, the transition density $p(\mathbf{x}^k | \mathbf{x}^{k-1})$ gives the distribution of the states propagated at time k (Eq. 3.2). By "proposing" a different transition density to forward the prior ensemble, we can obtain more effective particle weights (Ades and van Leeuwen, 2015; Chorin and Morzfeld, 2013; Snyder et al., 2015) and avoid weight collapse (Chap. 2). To obtain such transition density, it is possible to modify the

transition density of the standard particle filter, by multiplying and dividing Eq. 3.2 by a function $q(\mathbf{x}^k|\mathbf{x}^{k-1}, \mathbf{y}^k)$, which we refer to as proposal transition density $q(\mathbf{x}^k|\mathbf{x}^{k-1}, \mathbf{y}^k)$. Introducing this term in Bayes' theorem, we obtain

$$p(\mathbf{x}^k|\mathbf{y}^{0:k}) = \frac{p(\mathbf{y}^k|\mathbf{x}^k)}{p(\mathbf{y}^k)} \int \frac{p(\mathbf{x}^k|\mathbf{x}^{k-1})}{q(\mathbf{x}^k|\mathbf{x}^{k-1}, \mathbf{y}^k)} q(\mathbf{x}^k|\mathbf{x}^{k-1}, \mathbf{y}^k) p(\mathbf{x}^{k-1}|\mathbf{y}^{1:k-1}) d\mathbf{x}^{k-1}. \quad (3.4)$$

The principle of the proposal transition density is that it is possible to multiply and divide by any density $q(\mathbf{x}^k|\mathbf{x}^{k-1}, \mathbf{y}^k)$ as long as $p(\mathbf{x}^k|\mathbf{x}^{k-1}) \leq q(\mathbf{x}^k|\mathbf{x}^{k-1}, \mathbf{y}^k)$, to not divide by zero. In the case where the N_e particles have equal weight at the previous time step $k-1$ (in this study, it is the case before the first assimilation step), we can write

$$p(\mathbf{x}^{k-1}|\mathbf{y}^{1:k-1}) = \sum_{i=1}^{N_e} \frac{1}{N} \delta(\mathbf{x}^{k-1} - \mathbf{x}_i^{k-1}) \quad (3.5)$$

in Eq. 3.4, and we obtain the posterior distribution

$$p(\mathbf{x}^k|\mathbf{y}^{0:k}) = \sum_{i=1}^{N_e} \frac{p(\mathbf{y}^k|\mathbf{x}_i^k)}{p(\mathbf{y}^k)} \frac{p(\mathbf{x}_i^k|\mathbf{x}_i^{k-1})}{q(\mathbf{x}_i^k|\mathbf{x}_i^{k-1}, \mathbf{y}^k)} \delta(\mathbf{x}^k - \mathbf{x}_i^k). \quad (3.6)$$

In Eq. 3.6, we use the expression of $p(\mathbf{x}^{k-1}|\mathbf{y}^{1:k-1})$ considering equal-weight particles (i.e., the particle probability is proportional to $1/N$). The principle of the proposal density is that instead of drawing particles from the transition density $p(\mathbf{x}^k|\mathbf{x}_i^{k-1})$, we sample directly from $q(\mathbf{x}_i^k|\mathbf{x}_i^{k-1}, \mathbf{y}^k)$. Because $q(\mathbf{x}_i^k|\mathbf{x}_i^{k-1}, \mathbf{y}^k)$ can also be expressed as a sum of Dirac functions at time k , and because term $1/N$ (Eq. 3.5) is omitted in the following since it is the same for each particle, we write the expression of the particle weights as a function of the proposal density q with

$$w_i \propto p(\mathbf{y}^k|\mathbf{x}_i^k) \frac{p(\mathbf{x}_i^k|\mathbf{x}_i^{k-1})}{q(\mathbf{x}_i^k|\mathbf{x}_i^{k-1}, \mathbf{y}^k)}. \quad (3.7)$$

The expression of the posterior distribution becomes

$$p(\mathbf{x}^k|\mathbf{y}^{0:k}) = \sum_{i=1}^{N_e} w_i \delta(\mathbf{x}^k - \mathbf{x}_i^k). \quad (3.8)$$

This derivation gives the basis for a proposal density, q , for which we can use an arbitrary density function with $q(\mathbf{x}^k|\mathbf{x}^{k-1}, \mathbf{y}^k) = p(\mathbf{x}^k|\mathbf{x}^{k-1})$ in the standard particle filter. However, it is not trivial how one should choose another expression for the proposal density (van Leeuwen et al., 2015).

Doucet et al., 2000 suggest the ‘‘optimal proposal’’ and define a proposal density, q , based on the observations at time k as

$$q(\mathbf{x}^k|\mathbf{x}^{k-1}, \mathbf{y}^k) = p(\mathbf{x}^k|\mathbf{x}^{k-1}, \mathbf{y}^k). \quad (3.9)$$

According to Doucet et al., 2000, by choosing the proposal density from Eq. 3.9, we can use the observations at the next time step, k , to sample the particles. To derive an

expression for weights using the optimal proposal in Eq. 3.9 we use Bayes' theorem, to express the optimal proposal as

$$q(\mathbf{x}^k | \mathbf{x}^{k-1}, \mathbf{y}^k) = p(\mathbf{x}^k | \mathbf{x}^{k-1}, \mathbf{y}^k) = \frac{p(\mathbf{y}^k | \mathbf{x}^k) p(\mathbf{x}^k | \mathbf{x}^{k-1})}{p(\mathbf{y}^k | \mathbf{x}^{k-1})}. \quad (3.10)$$

Using the expression for the weights (Eq. 3.7) and using the expression of q of Eq. 3.10 we obtain

$$w_i = p(\mathbf{y}^k | \mathbf{x}_i^k) \frac{p(\mathbf{x}_i^k | \mathbf{x}_i^{k-1})}{p(\mathbf{x}_i^k | \mathbf{x}_i^{k-1}, \mathbf{y}^k)} \quad (3.11)$$

$$= p(\mathbf{y}^k | \mathbf{x}_i^{k-1}). \quad (3.12)$$

In the work of Doucet et al., 2000, the optimal proposal is derived for different cases, depending on the Gaussianity and the linearity of the problem. In our subsidence problem, distribution of model and observation errors are assumed Gaussian.

3.3.2. OPTIMAL PROPOSAL APPLIED IN THE SUBSIDENCE PROBLEM

In the example of subsidence caused by a compacting reservoir, the state vector is composed of the model state variables of compaction, ζ , and displacement field, \mathbf{u} , such as $\mathbf{x} = [\zeta, \mathbf{u}]^T$. A forward model transforms the compaction state, ζ to the displacement field, \mathbf{u} . In Chapter 2, we have introduced the forward model, \mathcal{M} , in a quasi-static example. Now, \mathcal{M} forwards the model states in time, and the observation operator, \mathcal{H} , maps state space to observation space. Here, we make the same assumption as in Chapter 2, namely, that \mathcal{H} represents the measurement operator, which is solely a function of the measurement method and can be defined with an I_d (Identity) observation operator. From the general model

$$\mathbf{x}^k = \mathcal{M}(\mathbf{x}^{k-1}) + \mathbf{e}^k \quad (3.13)$$

$$\mathbf{y}^k = \mathcal{H}\mathbf{x}^k + \epsilon^k, \quad (3.14)$$

we obtain for our specific subsidence problem

$$\begin{aligned} u^k &= \mathcal{M} \left[\mathbf{u}^{k-1}(\zeta^{k-1}) \right] + \mathbf{e}^k \\ \mathbf{y}^k &= \mathcal{H} \mathcal{M} \left[\mathbf{u}^{k-1}(\zeta^{k-1}) \right] + \epsilon^k = \mathcal{H} \mathbf{u}^k + \epsilon^k. \end{aligned} \quad (3.15)$$

With the measurement error, ϵ and the model error, \mathbf{e} . The subsidence problem in Eq. 3.15 is illustrated in Fig. 3.1 as a Markov process of the model state vector, where the compaction, ζ , is the unobservable model state.

To implement the optimal proposal based on the example in Doucet et al., 2000, we consider Gaussian and independent model error, $\mathbf{e} \sim N(0, \Sigma_e)$, and observation error, $\epsilon \sim N(0, \Sigma_\epsilon)$. To implement the optimal proposal in the subsidence problem, we sample compaction states, ζ and write the transformation from compaction to subsidence in the forward model as $u = A\zeta$ (Eq. 3.15). Assuming that we know A , this allows us to derive the

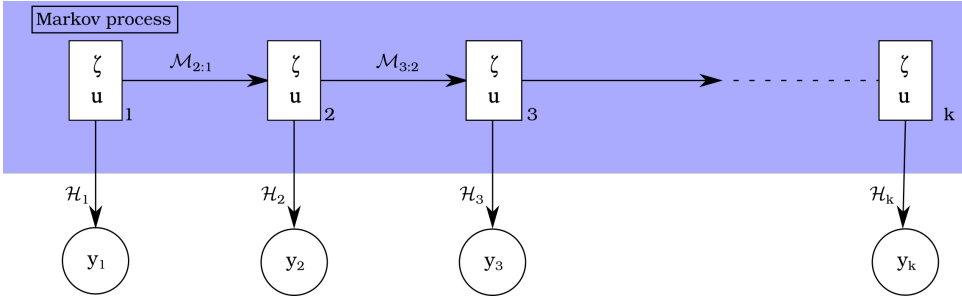


Figure 3.1: Illustration of a Markov process in the subsidence problem, showing the dynamical model, \mathcal{M} forwarding in time the model state vector, $\mathbf{x} = [\zeta, \mathbf{u}]$. The observation operator, \mathcal{H} , is applied to the state vector to map the model state of displacement, \mathbf{u} to the observations \mathbf{y} . The compaction states ζ is the unobservable variable to be estimated with data assimilation.

expression of the optimal proposal (Doucet et al., 2000; Snyder et al., 2015) as a function of ζ . From the subsidence model in Eq. 3.15 and the Gaussian assumption for ϵ and \mathbf{e} we obtain

$$\mathbf{y}^k | \zeta^k \sim N(\mathcal{H} A \zeta^k, \Sigma_e), \quad \mathbf{y}^k | \zeta^{k-1} \sim N(\mathcal{H} \mathcal{M}(A \zeta^{k-1}), \Sigma_e + \mathcal{H} \Sigma_e \mathcal{H}^T). \quad (3.16)$$

Using the property of the conditional distribution of the multivariate Gaussian distribution, which implies that all conditional distributions of a multivariate Gaussian distribution are Gaussian (Snyder et al., 2015; Tong and Tong, 1990), we can express the optimal proposal density at time k , as a Gaussian distribution

$$\zeta^k | (\zeta^{k-1}, \mathbf{y}^k) \sim N(\mu^k, \mathbf{P}), \quad (3.17)$$

with mean μ^k and covariance matrix, \mathbf{P} :

$$\begin{aligned} \mu^k &= m_\zeta^k + \Sigma_e \mathcal{H} (\mathcal{H} \Sigma_e \mathcal{H}^T + \Sigma_e)^{-1} (\mathbf{y}^k - \mathcal{H} \mathcal{M}(A m_\zeta^{k-1})) \\ \mathbf{P} &= \Sigma_e - \Sigma_e \mathcal{H} (\mathcal{H} \Sigma_e \mathcal{H}^T + \Sigma_e)^{-1} \Sigma_e \mathcal{H}, \end{aligned} \quad (3.18)$$

where m_ζ is the mean of the prior probability distribution of the compaction ζ from a background knowledge. Using the same property of the conditional distribution of multivariate Gaussian distribution, we can similarly derive the expression for the weights

$$w_i^k \propto \exp\left(-\frac{1}{2} (\mathbf{y}^k - \mathcal{H} \mathcal{M}(A \zeta_i^{k-1}))^T (\Sigma_e + \mathcal{H} \Sigma_e \mathcal{H}^T)^{-1} (\mathbf{y}^k - \mathcal{H} \mathcal{M}(A \zeta_i^{k-1}))\right). \quad (3.19)$$

This implementation of the proposal density is based on Gaussian assumptions and is assumed to be suitable for nonlinear models (Doucet et al., 2000; Snyder et al., 2015).

This implementation of the particle filter with the optimal proposal provides an approach to sample the model states, allowing us to propagate the particles forward in an average trajectory closer to the observations. The implementation prevents a single particle (model realization) from approaching observations more than the other particles, thereby avoiding weight collapse. Algorithm 2 gives an example of the implementation of the particle filter with the optimal proposal for the specific case of the subsidence problem.

Algorithm 2 Implementation of the optimal proposal density in a model of subsidence caused by a compacting reservoir. In this example, leveling data in 2018 are relative to 1978 and involve $N_y = 436$ benchmarks. Compaction values are expressed in meters.

Initialization:

Background knowledge (van Elk et al., 2021; van Elk et al., 2022) $\zeta^{bg} \sim N(0.05, 0.1)$ equivalent to a compaction velocity of $\dot{\zeta}^{bg} = 0.019$ m/year.

Model error $e \sim N(0, 1.10^{-3})$ and $\epsilon \sim N(0, 5.10^{-3})$.

Sampling $\zeta^k | (\zeta^{k-1}, \mathbf{y}^k)$

→ Compute the model A, corresponding to the subsurface response to nuclei with a compaction value of one.

→ Compute μ^k and \mathbf{P} from Eq. 3.18.

→ Sample the ensemble of compaction with N_e particles for each nucleus, n , giving an ensemble of dimension $(N_e \times N_x)$ (Sec.2.3.2)

for $i = 1 : N_e$ **do**

$$p(\zeta^k | \zeta^{k-1}, \mathbf{y}^k)_i \sim N(\mu_k, \mathbf{P}^2)$$

end for

Update

→ Compute model realizations of subsidence field (i.e., the cumulative subsidence from all nuclei, n), u_i^k , for each particle a and apply Eq. 3.19 to update the weights

for $i = 1 : N_e$ **do**

$$u_i^k = \sum_n^{N_x} u_{i,n}^k(\zeta_{i,n}^k)$$

end for

3.4. VERIFICATION ON A COMPACTING RESERVOIR EXAMPLE

To verify the performance of the optimal proposal particle filter in estimating reservoir compaction and subsidence, we model subsidence from an example of a homogeneously compacting reservoir using the analytical solution of Geertsma, 1973 and Geertsma and van Opstal, 1973 (Chap. 1). The reservoir is discretized into cuboid-shaped cells, where a nucleus of strain in each cell represents the cell's compaction (c.f. with the “multi-component model” in Section 2.3). Each cell of the model has identical compaction ζ . We write the solution of the vertical displacement u_i caused by a nucleus, i in location (x_i, y_i, z_i) and assume it is observed at location (x, y, z)

$$u_i = -\frac{(1-\nu)\delta l^2}{\pi} \frac{D}{R^3} \zeta$$

$$R = \sqrt{(x-x_i)^2 + (y-y_i)^2 + (z-z_i)^2}, \quad (3.20)$$

where R is the distance between the nucleus of strain and an observation point at the Earth's surface, D is the depth of the nucleus, δl is the resolution of the grid cell, ν is the Poisson ratio, and ζ is the compaction for a period of production. The subsidence field, u , resulting from the compaction of all nuclei of strain is the sum of displacements u_i created by each nucleus i (Tempone et al., 2010). In the following, we refer to the “observation point” as the location in space where a subsidence observation is available for the assimilation.

3.4.1. AVOIDING WEIGHT COLLAPSE WITH THE OPTIMAL PROPOSAL

In synthetic experiments, the observation vector, \tilde{y} , of dimension N_y , provides simulated cumulative displacements relative to the start of the production. The notation, \tilde{y} , refers to the synthetic observation vector defined in Section 2.3.3. N_y corresponds to the dimension of the observational space, i.e., the number of observation points. To create synthetic observations \tilde{y} , we use the reservoir pressure data from van Elk et al., 2022, provided by the producer NAM. Using the pressure decline, we evaluate the reservoir compaction, used as input to compute subsidence with Eq. 3.20. Synthetic observations, \tilde{y} , are generated by sampling the resulting subsidence field and by adding Gaussian noise with variance $\sigma^2 = 25.10^{-6}$ m to the data points to mimic the observational error (Fig. 3.2). We compare the standard and the optimal proposal particle filter in three different experiments for an increasing number of observation points, $N_y = 10$, $N_y = 30$, and $N_y = 100$ (Tab. 4.1).

Table 3.1: Summary of the data assimilation experiments performed to compare the standard particle filter (SPF) and the particle filter with optimal proposal (PFOP). The implementation of the particle filter is tested in three cases: first in synthetic experiments and after with leveling and InSAR data. For each experiment, the ensemble size, N_e , and the number of assimilated observations, N_y is indicated. The expected mean $E[w_{max}]$, of the maximal weight, w_{max} , indicates the trend of weight collapse over several identical simulations.

	Ensemble size (N_e)	Number of observations (N_y)	$E[w_{max}]$
SPF Synthetic	500	10	0.25
	500	30	0.5
	500	100	> 0.5
PFOP Synthetic	500	10	< 0.2
	500	30	0.2
	500	100	0.4
SPF Leveling	10^3	436 (epoch 2018)	1
PFOP Leveling	10^3	436 (epoch 2018)	0.4
SPF InSAR	10^3	1032	1
PFOP InSAR	10^2	1032	1
	10^3	1032	0.1

By applying the standard particle filter to the subsidence model and the synthetic observations, we test posterior weight collapse for a varying number of observation points and a given ensemble size. We start with ten observation points, i.e., ten different locations in space with one subsidence observation each, which gives $N_y = 10$ observations to assimilate and one value of compaction to estimate (homogeneous reservoir). In the first experiment (SPF synthetic Tab. 4.1), we use the standard particle filter and generate an ensemble of compaction values in 1964 and forecast it to 1972 (Fig 3.3). In this conceptual example, the model \mathcal{M} , moving the ensemble forward in time, such as $\mathbf{x}^{k+1} = \mathcal{M}(\mathbf{x}^k)$, is an identity (I_d) operator $\mathcal{M} = I_d$. Figure 3.3(left) shows the ensemble of compaction values sampled with the standard particle filter, with identical values in 1964 and 1972. Whereas the prior ensemble of compaction shows sufficient

spread around the truth, the prior ensemble of subsidence (computed from compaction) in Fig. 3.3(right) does not sufficiently cover the truth and the observations.

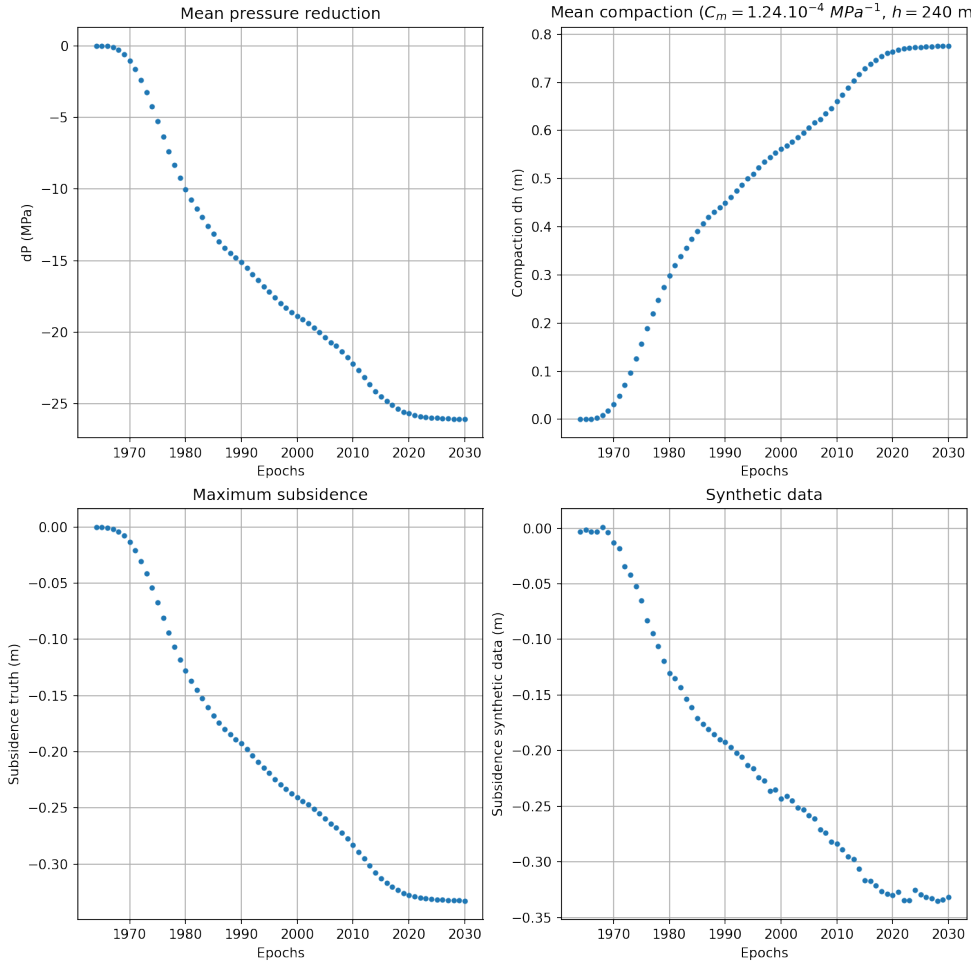


Figure 3.2: Pressure data of the mean pressure in the Groningen gas reservoir from the start of the production in 1964 to 2022 and forecasts to the year 2030. The mean pressure is provided by the NAM and estimated for the entire reservoir based on their reservoir model. The compaction is calculated from the mean pressure reduction and is used as an input in the forward model to compute subsidence. The reservoir compaction is calculated from pressure reduction using values of the compaction coefficient, C_m , and the reservoir height h , from background knowledge. Synthetic data are generated from the modeled subsidence by adding Gaussian noise to the output modeled subsidence.

After the assimilation of the synthetic data, the analysis of reservoir compaction in 1972 is used to update the modeled subsidence in 1972 (magenta star in Fig. 3.3). To evaluate posterior weight collapse, we repeat the previous assimilation step 300 times and compute the maximal weight, w_{max} . The 300 simulations are repeated independently and give a value of w_{max} at each new simulation. The same experiments are performed

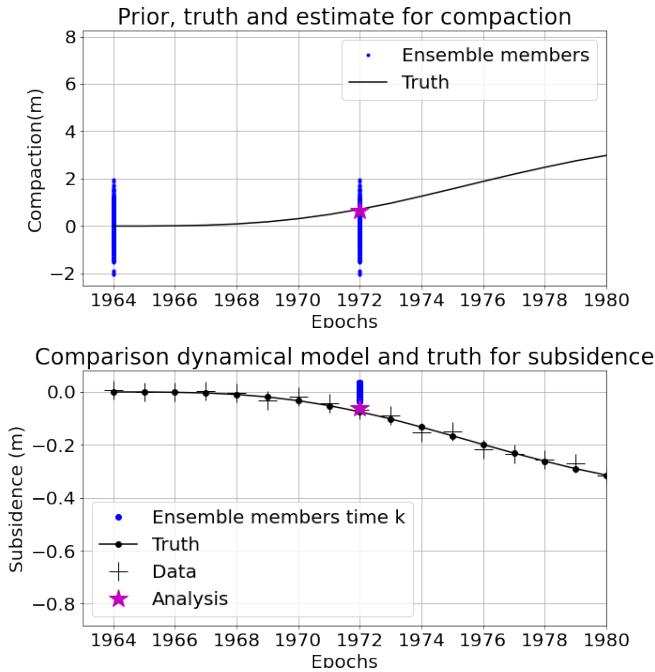


Figure 3.3: Synthetic experiment with the standard particle filter showing an analysis of the reservoir compaction (top) and subsidence states (bottom) for $N_y = 10$ and $N_e = 1000$, with a displacement time series mimicking the leveling data at one observation point. The ensemble at the assimilation step is indicated with blue dots, and the truth with a solid black line. The magenta star indicates the model update of subsidence from the estimated compaction obtained from the data assimilation analysis. The limited spread of the ensemble over the truth illustrates how weight collapse can occur in this example of subsidence caused by a compacting reservoir.

with an increasing number of observation points, $N_y = 30$ and $N_y = 100$, and with both the standard particle filter and the particle filter with the optimal proposal. Histograms of the maximal weight in Fig. 3.4 show that, as expected, the maximal weight converges to the value 1 for an increasing number of observations and a constant ensemble size of $N_e = 500$. A comparison of the maximal weight obtained with the standard particle filter and the particle filter with the optimal proposal with an identical ensemble size, $N_e = 500$, shows that $E[w_{max}] < 0.4$ in the implementation of the particle filter with the optimal proposal, whereas it converges to 1 with the standard particle filter (Fig. 3.5).

3.4.2. TESTING THE OPTIMAL PROPOSAL WITH LEVELING

We now test the particle filter with the optimal proposal to assimilate actual leveling data of the Groningen region. Optical leveling campaigns have been conducted since the start of gas production in 1964 (Fig. 3.6). The leveling technique provides subsidence estimates relative to an epoch of reference and a benchmark (i.e., observation points) of

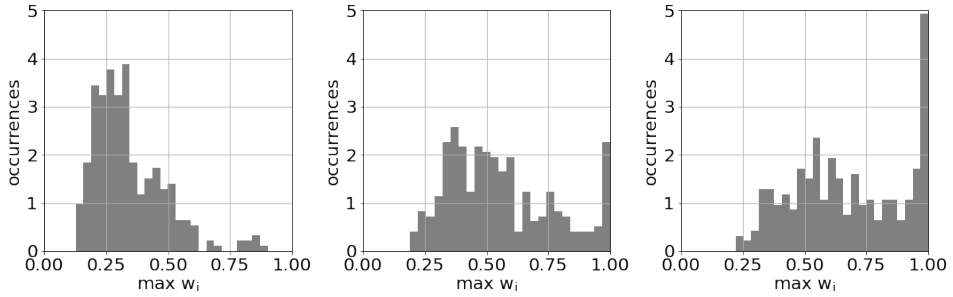


Figure 3.4: Histograms of the maximal posterior weight for the synthetic experiment with a standard particle filter (SPF synthetic) showing how weight collapse increases for an increasing number of observations $N_y = 10$, $N_y = 30$, and $N_y = 100$ for $N_e = 500$. The maximal weights are evaluated over 300 simulations.

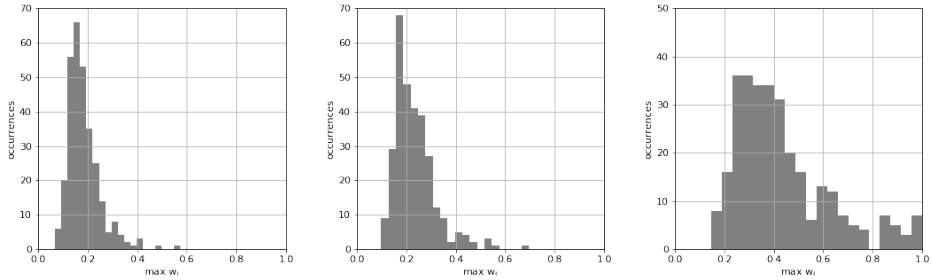


Figure 3.5: Histograms of the maximal posterior weight for the synthetic experiment with particle filter implemented with the optimal proposal (PFOP synthetic). showing how weight collapse increases for an increasing number of observations $N_y = 10$, $N_y = 30$, and $N_y = 100$ for $N_e = 500$. The maximal weights are evaluated over 300 simulations.

reference, and cumulative displacements are available approximately every five years with values relative to the first epoch in 1964 (Sec. 1.2). The benchmark's number and location can vary between the different epochs we then keep only benchmarks with displacement relative to the same benchmark of reference and the same epoch of reference (Sec. 1.2). Fig. 3.6 shows the leveling benchmarks above the Groningen region and the cumulative displacement in 1975 relative to 1964 with the time series of maximal subsidence from 1964 to 2018. In the following, to obtain more than 400 benchmarks over the gas field, we choose 1978 as a reference and assimilate four epochs between 1978 and 2018. The subsidence trend in Fig. 3.6b shows the maximal subsidence over the entire area with a quasi-linear time evolution of subsidence. The almost linear evolution of subsidence suggests that for the production regime in this period, a five-year data-assimilation window is sufficient to test the particle filter.

The same approach as in Section 3.4.1 is applied to test the particle filter with the optimal proposal: we estimate the reservoir compaction at each assimilation step and update the modeled subsidence. In Fig. 3.6, the ensemble members are indicated with grey

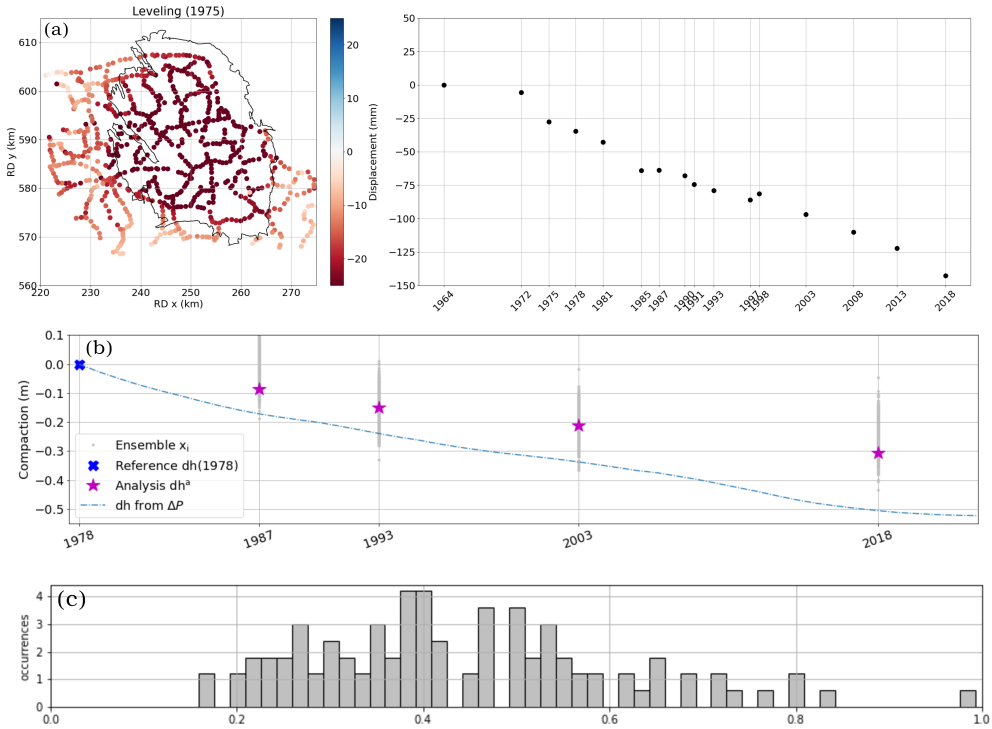


Figure 3.6: (a) Subsidence map showing the leveling benchmarks above the Groningen gas field with cumulative displacement at the epoch 1975 relative to 1978: we choose 1978 as a reference because the leveling network has more benchmarks than in 1964. (a-right) shows the time series of the maximal subsidence from the start of the production in 1964: the cumulative subsidence is zero at the reference date. (b) Data assimilation results showing the estimated cumulative compaction relative to the date of 1978 (magenta stars). The analysis is performed at four epochs for the period 1978-2018. The blue dashed line indicates the compaction computed from the NAM pressure data, the compaction analysis with data assimilation is indicated with magenta stars, and the ensemble spread is indicated with grey dots. (c) The histogram of the maximal posterior weight, w_{max} , indicates the tendency for weight collapse in the assimilation step 2018, where $N_y = 436$ observations are assimilated with an ensemble size of $N_e = 1000$.

dots, showing the spread of the particles, and the compaction analysis is indicated with magenta stars for each assimilation step. The compaction analysis follows the trend of the averaged reservoir compaction calculated from the NAM pressure model (blue dashed line in Fig. 3.6) but has a lower magnitude of the reservoir compaction. Not surprisingly, the homogeneous reservoir model does not fully represent the complexity of the actual reservoir driving mechanisms. As a result, the observed subsidence will differ from the subsidence modeled with the homogeneous reservoir model, but this provides a conceptual framework to test the particle filter. As in the experiment in Section 3.4.1, we run 300 times identical and independent experiments to evaluate the histogram of the maximal weights. Figure 3.6c shows the resulting histogram of the maximal weight for the experiment at the epoch of 2018, where $N_y = 436$ observation points are assimilated with an ensemble size of $N_e = 1000$. The maximal weight,

w_{max} , remains on average below 0.6, which is in agreement with the result in synthetic experiments. Results of maximal weights show that it is possible to assimilate leveling observations of the Groningen region with a particle filter and an ensemble size of $N_e = 1000$.

3.4.3. TESTING THE OPTIMAL PROPOSAL WITH INSAR

The InSAR technique provides additional displacement estimates that complement the leveling estimates. To test the particle filter with the optimal proposal, we assimilate InSAR displacement velocities linearly interpolated in the period from 2015 to 2020. Each observation point (i.e., Point Scatterer PS) has a displacement velocity, (Sec. 1.2), which provides a dense spatial distribution of the observation points: an InSAR dataset contains more than 1 million observation points for each epoch, meaning more than 1 million spatially distributed observation points every six days. We apply a similar approach as in the case of the test with leveling observations and homogeneous reservoir compaction, using the reservoir pressure from the NAM as input to our subsidence model. We perform one assimilation step in 2020 to estimate an average compaction rate for 2015-2020, which allows us to update the displacement velocity in 2020.

DATA REDUCTION

The region of Groningen gives an area of study of approximately $50 \text{ km} \times 50 \text{ km}$, with more than 1 million spatially distributed PS to assimilate, involving an unpractical ensemble size for the particle filter. Observation points are very densely distributed over certain areas, suggesting that the observations may contain redundant information that can be removed from the dataset without losing valuable information. Since it is difficult to evaluate the quality and information content of each individual observation point and consequently evaluate which point can be eliminated from the dataset, we proceed as follows with an entropy estimation. The InSAR dataset is composed of *distributed* scatterers and *point* scatterers (Sec. 1.2). The distributed scatterers give displacements averaged from InSAR reflection, and point scatterers provide displacements from a single reflection point (i.e., simple reflection). First, we remove the distributed scatterers from the dataset and only use displacements from the point scatterers. This allows us to reduce the dataset from 1.5 million to approximately 600.000 observation points. To remove redundant information from the dataset, we use a regular grid over the region of study and test different averaging radii to average data over this grid (see Fig 3.7a green circle of radius δl). Using the entropy metric previously introduced in Section 2.4, we can quantify the information content of the reduced dataset. The entropy, $H(x)$, is minimal if a variable x_i can be estimated with zero uncertainty from $p(\mathbf{x})$, with the probability $p(x_i) = 1$. Conversely, the entropy is maximal and equal to $H(x) = \log(N_e)$, if there is equal probability between N variables, with $p(x_i) = 1/N$ (Chap. 2).

The entropy for the InSAR dataset measures the uncertainty or randomness of the distribution of the displacement velocity values in this dataset. In Fig. 3.7b, for the averaging radius, $\delta l < 2 \text{ km}$, the entropy is estimated to be approximately $H(y) = 0.75$ and this increases to $H(y) = 0.85$ for an averaging radius $\delta l > 3 \text{ km}$. The low entropy value suggests that the subsidence signal from a point scatterer relates to a more specific

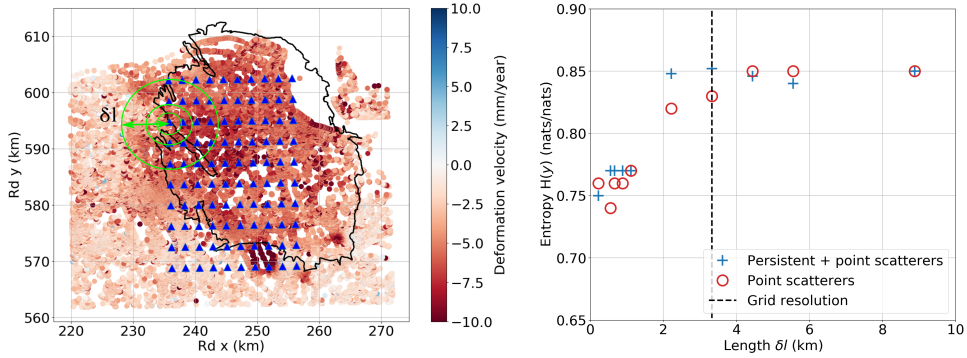


Figure 3.7: (Left) Subsidence map showing circles of different radii (green solid line) used to spatially average InSAR displacement velocity of the observation points over a regular grid (blue triangles) in a neighborhood of δl radius. The solid black line represents the field outline. (Right) The entropy of the reduced dataset as a function of the averaging radius δl shows the reduction of entropy as the averaging area becomes smaller: 1) for a dataset with distributed and 2) point scatterer is indicated with a blue cross. The entropy calculated for the dataset reduced to the point scatterer is indicated with red circles. The dashed line indicates the grid resolution at the value of δl , where the maximal entropy for this spatially averaging experiment is reached.

process, such as deep-driven subsidence, compared to the signal from distributed scatterers, which can be an average of deep-driven and other subsidence signals. For example, point scatterers are often related to reflection on buildings and, thus, deep-driven subsidence. This supports our choice to remove distributed scatterers from the dataset if we aim to estimate only the deep-driven subsidence. With a radius between 2 and 4 km the entropy reaches almost constant values of $H(y) \sim 0.85$, suggesting that the information in the averaged data is similar to that in the initial dataset, with “maximal randomness”. Based on the entropy results in Fig. 3.7, we average point scatterers in an area of 500m diameter to remove redundant information. We obtain an entropy of approximately 0.75. To further reduce the number of observations, we divide the Groningen area into 2km cells. Each grid cell thus contains several averaged observation points (i.e., averaged point scatterers) based on the 500m diameter spatial average. To have a distribution of displacement velocity that is not completely regular, but also has no high concentrations of observation points, we randomly select one averaged observation point in each grid cell. We obtain the spatial distribution of subsidence observations illustrated in Fig. 3.8.

RESULTS OF THE ASSIMILATION OF IN SAR DISPLACEMENTS OVER GRONINGEN

A first test is performed with 288 spatially distributed observation points (PS), $N_y = 288$, and an ensemble size of $N_e = 100$. After applying the particle filter with the optimal proposal assimilating the displacement velocities in 2020, the subsidence update is computed from the estimated reservoir compaction. The maximal displacement velocity, estimated with the particle filter as shown in Fig. 3.8b, suggests a maximal displacement velocity of approximately 10mm/year, which is in agreement with the observed subsidence (Fig. 3.8a). As expected and similar to the experiment with leveling

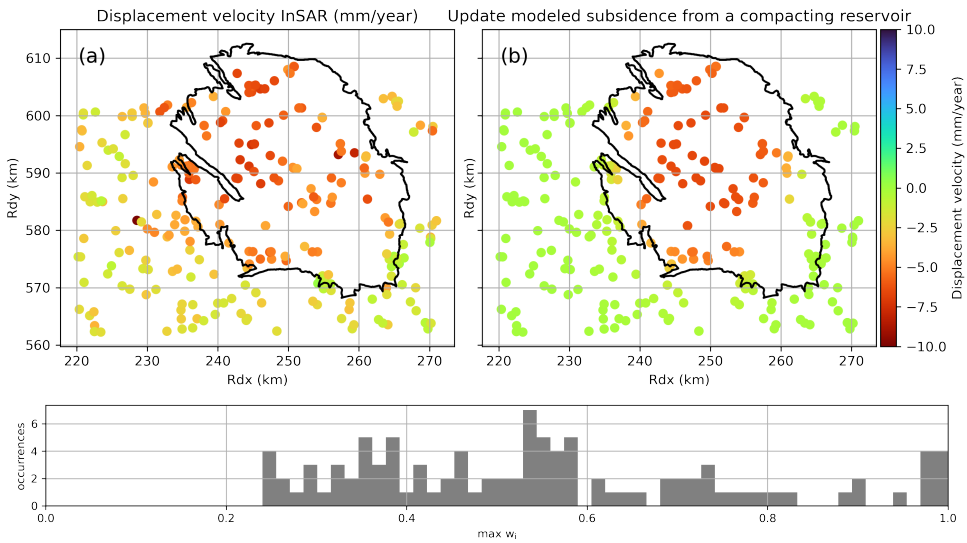


Figure 3.8: Subsidence map of the Groningen gas field (black solid line) showing linear displacement velocities of 288 PS-InSAR location above the Groningen gas field. (a) The InSAR dataset with 288 observation points was used for the assimilation. (b) The subsidence estimate is computed from the compaction analysis after the assimilation step, showing the subsidence in mm/year at the observation locations. (Bottom) The histogram of the maximal posterior weight is computed over 100 data-assimilation runs for the $N_y = 288$ observations and an ensemble size of $N_e = 100$.

displacements, the homogeneous compacting reservoir does not fully represent the heterogeneity of the subsidence field. The InSAR displacements show local subsidence over the area with a spatial extent smaller than 1 km that is not present in the data-assimilation estimates. The actual measurement error is unknown, but we can assume several millimeters based on the order of magnitude of InSAR errors (Auriac et al., 2014; Ketelaar, 2009). The choice of the observation error in the data-assimilation system also has an effect on the posterior weight collapse: the assumption of a small observation error reduces the variance of the likelihood and can cause weight collapse. In this experiment with InSAR, we are interested in testing how the particle filter with the optimal proposal avoids weight collapse. Therefore, we assume the minimal value of $\epsilon = 1$ mm for all observations. In the experiment with $N_y = 288$ and an ensemble size of $N_e = 100$ the data-assimilation analysis gives an estimated compaction rate of -0.065 m/year associated with a maximal subsidence of approximately 10 mm/year, and a maximal weight averaged less than 0.6 (Fig. 3.8).

The same experiment as the one described above (with the homogeneous reservoir and the same ensemble size, $N_e = 100$) is now performed with a larger dataset of $N_y = 1032$ observation points and an ensemble size of $N_e = 100$ (Fig. 3.9). For this experiment, the estimated reservoir compaction of 0.071 m/year gives a modeled-subsidence update of approximately -10 mm/year. As expected, the posterior distribution suffers from weight collapse. The maximal weights are indicated in the histogram in Fig. 3.9

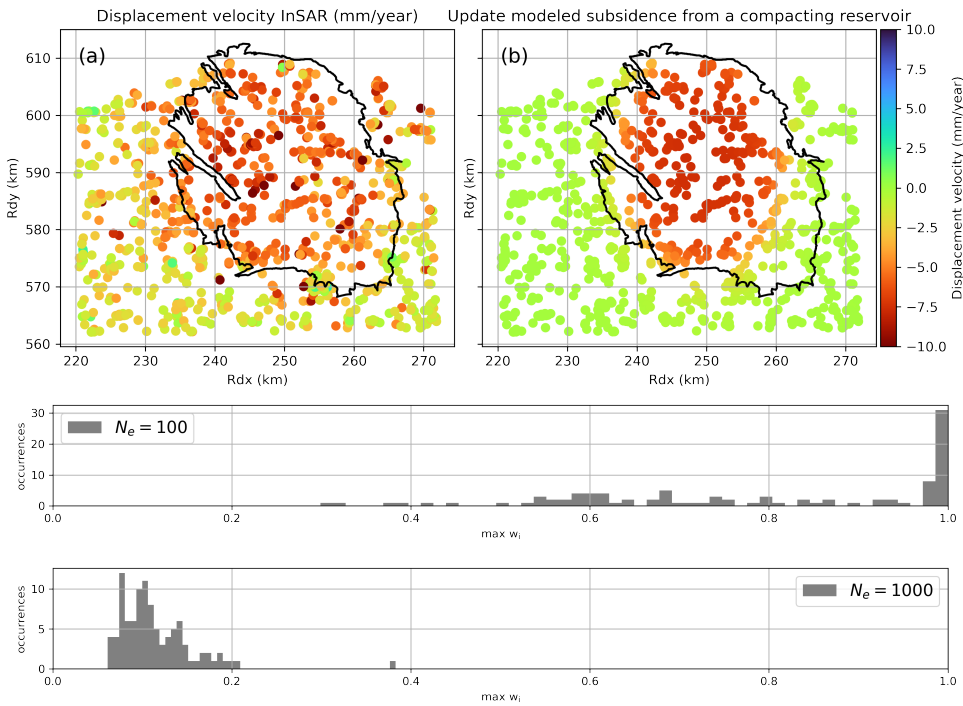


Figure 3.9: Subsidence map of the Groningen gas field (black solid line) showing displacement velocities at PS locations above the Groningen gas field with (a) the InSAR displacement velocity from the reduced dataset and (b) the model-update of subsidence after assimilation. The histograms of the maximal weight are computed over 100 data-assimilation runs. Histograms show the maximal weights in an experiment with $N_y = 1032$ observation and with (top) $N_e = 100$ and (bottom) $N_e = 1000$, showing weight collapse for $N_e = 100$ and the absence thereof for $N_e = 1000$.

(histogram based on 100 simulations) and show that most maximal weights are above 0.6, suggesting weight collapse.

We increase the ensemble size to $N_e = 1000$, repeat the experiment with $N_y = 1032$ observation points, and evaluate how the maximal weight changes. The result in Fig. 3.9 shows that the maximal weight is reduced from almost 1 to less than 0.2. The estimated compaction for this experiment is 0.071 m/year, in agreement with the previous experiment with $N_y = 288$ and an ensemble size of $N_e = 100$.

3.5. DISCUSSION

This chapter provides an application of the particle with an optimal proposal for subsidence estimation in the Groningen region and focuses on evaluating weight collapse. The result of weight collapse in the experiments in this chapter agrees with our synthetic tests in Section 3.4.1 and the results in Snyder, 2011 and Snyder et al., 2015. Indeed, Snyder et al., 2015, based on theoretical proof, provides an expression for the performance bound of the optimal proposal at the asymptotic limit and proposes how to avoid weight collapse with the optimal proposal. Another approach based on the particle filter (NAM, 2017) is proposed for the Ameland gas field, a small reservoir in the Groningen region. The method of NAM, 2017 is similar in that it is based on a proposal density. However, further description of the NAM, 2017 method could help understand how weight collapse is avoided and, thus, if their approach can be applied to other cases.

The results of the experiments in this chapter reveal limitations in both the model, the data, and the data-assimilation methodology. A homogeneous compacting reservoir does not fully represent subsidence observed with leveling and InSAR data. Specifically with InSAR, we notice the sensitivity of weight collapse to the observation error, and thus the importance of setting correct observation errors in the data-assimilation approach (Eq. 3.14). This is also one of the conclusions of Snyder et al., 2015. The assumption of small measurement and model errors in the data-assimilation system gives the optimal proposal a small variance, which consequently samples the prior state variables with a narrow variance distribution. In our case, this has the effect of an estimated subsidence very close to the observations suggesting weight collapse or “overfitting”. Increasing the observation error can have a beneficial effect on weight collapse, similar to an “inflating” variance in the likelihood, allowing a better spread of the prior ensemble with the optimal proposal. Further work on the InSAR processing can help improve the assumptions on both observational and model errors.

Moreover, further refinement of the model would allow a better representation of non-homogeneous reservoir compaction. While this might give a more realistic simulation of subsidence, it could also increase the chance of posterior weight collapse. This could be the case, for example, with a compartmentalized reservoir or a model including an additional shallow source of subsidence (e.g., a combination of the one-component model and the multi-component model in Chapter 2).

Whereas avoiding weight collapse with a number of observations larger than $N_y = 1000$ requires unpractical ensemble sizes with the standard particle filter, it is possible with an ensemble size of $N_e = 1000$ when using the particle filter with the optimal proposal. As van Leeuwen et al., 2015 suggested, the optimal proposal particle filter may not be applicable in cases with very large observational- and state-space dimensions. For example, with an InSAR dataset of 1.5 million observation points. The authors also highlight that it is unclear if the particle filter with an optimal proposal would still apply in highly nonlinear systems. To our knowledge, the optimal proposal density particle filter’s applicability remains an open question since it has never been tested on highly nonlinear systems. In the example of subsidence in the Groningen gas field, the subsidence caused by the compacting reservoir is quasi-linear. However, nonlinearity in other processes causing subsidence above the Groningen gas field is uncertain. Thus,

the particle filter's applicability with an optimal proposal in a more complex system still needs to be tested. I address this point in Chapter 4. Since weight collapse appears to be mainly driven by the dimension of the observational space (Bengtsson et al., 2008; Snyder et al., 2008; Snyder et al., 2015), I expect that this particle filter implementation can help avoid weight collapse in a system with sizeable state-space dimension.

3.6. CONCLUSION

I implemented a particle filter with the so-called optimal proposal described in Doucet et al., 2000. The approach was tested on a compacting reservoir causing subsidence, with synthetic and actual leveling and InSAR datasets, assimilating 1000 observations with an ensemble size of $N_e = 1000$. The principle of the particle filter with an optimal proposal is to use the observations to improve the sampling of the prior ensemble. In the example of a compacting reservoir causing subsidence, we define a probability density function to sample a state vector of reservoir compaction and assimilate geodetic subsidence estimates to estimate the compaction and update the subsidence model. Results show that, for the same number of observations and ensemble size, the particle filter with an optimal proposal reduces weight collapse in the posterior distribution compared to the standard particle filter. We also test the optimal proposal density particle filter using leveling and InSAR data and with different sizes of observational data sets. In the two cases, we assimilate up to 1000 observations at a very low computational cost, with a maximal ensemble size of $N_e = 1000$. The results of experiments with the particle filter with an optimal proposal suggest that this method is well suited for compacting reservoirs of the Groningen gas field with InSAR and leveling displacement estimates.

4

MULTI-SOURCE SUBSIDENCE ESTIMATION AND FORECASTS USING THE PARTICLE FILTER METHOD AND INSAR

The sciences do not try to explain, they hardly even try to interpret, they mainly make models. [...] The justification of such a mathematical construct is solely and precisely that it is expected to work.

John van Neumann

Reducing reservoir thickness at several kilometers of depth by compaction in the subsurface can lead to land subsidence at the surface. In addition to reservoir compaction, processes in the upper subsurface layers contribute to the total subsidence. This chapter provides a data-assimilation approach for estimating subsidence in the Groningen region, combining InSAR time series of cumulative displacement with physics-based models. InSAR provides spatio-temporal information on the subsidence signal, with observation points densely distributed in space and available every six days. Our approach assimilates the InSAR time series of cumulative displacements into a physics-based model of subsidence caused by multiple subsurface processes. In this study, subsidence is caused by 1) a producing reservoir with linear time evolution of compaction and 2) the shallow subsurface, which causes subsidence with a periodic time evolution that appears to correlate with meteorological data. The methodology is validated in synthetic tests and provides proof of concept for identifying deep- and shallow-driven subsidence. We apply the same methodology with the InSAR time series and use different meteorological data to test the separation of large-scale subsidence from time-varying localized subsidence. Subsidence forecasts based on correlations with the climatological temperature of the Netherlands provide insight into potential subsidence-driving mechanisms.

4.1. INTRODUCTION

Subsidence above the Groningen gas field has a characteristic bowl-shaped profile caused by the compacting reservoir, with a large correlation scale of the subsidence field (Sec. 1.2). This compacting reservoir is assumed to be the dominant driver of subsidence in the Groningen region (Ketelaar, 2009), to which we will refer as the *deep driver* of subsidence in this chapter. Deep-driven subsidence is considered long-term subsidence since it increases over time proportionally to the pressure reduction in the reservoir layers. In this study, all other driving mechanisms causing subsidence are hereafter referred to as *shallow drivers*, in comparison to those at the depth of the reservoir depth (Chap. 1). In contrast to the expected subsidence caused by the compacting reservoir, InSAR-based displacement estimates show spatial heterogeneity in the subsidence field. Additionally to spatial heterogeneity, the observed temporal variation of the vertical displacement from the InSAR time series could be caused by processes other than the compacting reservoir, such as shallow subsurface processes. For example, in Section 1.3.2, I showed that soil dryness could lead to clay shrinkage and oxidation of the organic soils, such as peat, for soil layers above the groundwater level (Erkens et al., 2016). Groundwater level variability also results in swelling shallow layers with seasonal periodic patterns (van Asselen et al., 2020). The infrastructure motion caused by temperature changes can also be observed in the InSAR time series (Hanssen, 2001).

The deep- and shallow-driven subsidence differ in space and time. We expect the shallow-driven subsidence to be localized in space and to have a periodic time variability, whereas the deep-driven subsidence has quasi-linear time evolution (Chap. 1).

In data assimilation, both the model and the observations contain information about the system unknowns, and by combining them with data assimilation (i.e., with Bayes' theorem in Section 1.4.2), we reduce uncertainty about the system unknowns. In our case, the system unknowns are the subsidence-driving mechanisms. Data assimilation methods used in subsidence estimation (Candela et al., 2021; Kroon et al., 2009; Zoccarato et al., 2016) often assume linear models and represent model variables, parameters, model errors, and measurement errors with Gaussian statistics (Emerick and Reynolds, 2013; Iglesias et al., 2013; Wikle and Berliner, 2007). Based on the particle filter tested in Chap. 3 we propose an approach with a proposal density suitable for non-linear systems (Doucet et al., 2000; Farchi and Bocquet, 2018; Snyder, 2011; Snyder et al., 2015; van Leeuwen et al., 2015; van Leeuwen et al., 2019). The implementation of the particle filter from the work of Doucet et al., 2000 that we tested in Chapter 3, shows good applicability to problems with a large number of observations (Snyder, 2011), allowing a particle filter application with InSAR estimates. This approach and similar particle filter variants are referred to as the *optimal proposal particle filter* and, to our knowledge, were never applied to subsidence problems such as in the Groningen gas field.

In this chapter, we propose assimilating the InSAR time series of vertical cumulative displacements, accounting for 1) the temporal variability, i.e., with a seasonal subsidence signal in the InSAR estimates, and the spatial variability, i.e., varying

smoothness, of the subsidence signal in the InSAR estimates. Based on these spatio-temporal characteristics of the subsidence signals, we test the particle filter to identify multiple subsidence-driving mechanisms and estimate subsidence accordingly. The chapter is organized as follows. We provide an overview of the model and the subsidence observations in Sections 4.2 and 4.3, respectively, followed by an overview of the particle filter and its implementation for the assimilation of InSAR time series in Section 4.4. Next, we perform synthetic experiments that we discuss in Section 4.5, and finally, we apply the data assimilation method to the Groningen region with actual InSAR estimates in Section 4.6.

4.2. MULTI-SOURCES SUBSIDENCE MODEL

In this chapter, I consider total subsidence to be a combination of two sources of subsidence. One subsidence source is the reservoir's compaction, the deep-driven subsidence, and can be represented by a model similar to the "multi-component" model in Section 2.3.1. The other source represents processes in the shallow subsurface, causing shallow-driven subsidence. Since the shallow-driven subsidence has short spatial correlation scales compared to the grid on which we represent the subsidence (i.e., 2km), we can consider this with models of the "one-component" type in Section 2.3.2. The total subsidence field, u_{enu} , modeled at time t in a Cartesian east, north, up (e, n, u) coordinate system, with deep and shallow-driven subsidence is expressed with

$$u_{\text{enu}}(t) = u_{\text{enu}}^{\text{deep}}[\zeta(t)] + \eta(t), \quad (4.1)$$

where $u_{\text{enu}}^{\text{deep}}(\zeta(t))$ is the subsidence caused by the reservoir compaction, $\zeta(t)$, and driven by the pressure variation in the reservoir, whereas $\eta(t)$ is the additional subsidence term representing other sources of subsidence. We define η as a stochastic term. In the following, we first elaborate on the deep-driven subsidence, $u_{\text{enu}}^{\text{deep}}(\zeta(t))$, and then on the shallow-driven subsidence by introducing the SPAMS model (Conroy et al., 2023) and the temperature-based subsidence model.

Fjaer et al., 2008; Geertsma, 1973; Geertsma and van Opstal, 1973 describe a conceptual representation of compacting reservoirs with the nucleus of strain approach to model subsidence (Sec. 1.3.1). We use this approach and express Geertsma's solution in Cartesian coordinates to obtain a displacement in three directions, as it is commonly used for the InSAR displacement estimates. We consider a disk-shaped reservoir of 15km radius at a depth $D = 2900\text{m}$ that we discretize into 968 cells. With a radius of 15km (i.e., a diameter of 30km) the disk of nuclei of strain has approximately the width of the Groningen gas field. Such a representation of the Groningen gas field has been shown to realistically represent its subsidence bowl (van Thienen-Visser and Fokker, 2017). The uni-axial compaction of the reservoir, ζ , varies in time according to the hydrocarbon production and the averaged mean pressure reduction ΔP over a time period Δt (Chap. 1). The Earth's surface displacement at point coordinate (x, y, z) resulting from a single nucleus of strain i , at the location (x_i, y_i, z_i) , at depth D and at time t relates the displacement, u in the Cartesian coordinates E,N,U, to the compaction,

$\zeta(t)$, with the equations:

$$\begin{aligned} u_{E,i}(t) &= \frac{(1-\nu)}{\pi} \frac{(x-x_i)}{R^3} \delta l^2 \zeta(t) \cdot t \\ u_{N,i}(t) &= \frac{(1-\nu)}{\pi} \frac{(y-y_i)}{R^3} \delta l^2 \zeta(t) \cdot t \\ u_{U,i}(t) &= \frac{(1-\nu)}{\pi} \frac{D}{R^3} \delta l^2 \zeta(t) \cdot t \\ R &= \sqrt{(x-x_i)^2 + (y-y_i)^2 + (z-z_i)^2}, \end{aligned} \quad (4.2)$$

where R is the distance between the nucleus and a point at the surface, ν is the Poisson ratio, and δl is the resolution of a reservoir grid cell. For a reservoir discretized in N nuclei of strain, the displacement at one point, p , at the Earth's surface is the sum of displacements $u_{\text{ENU},i}$ created by each nucleus i :

$$u_{\text{ENU}}^{\text{deep}}(\zeta(t))_p = \sum_i^N u_{\text{ENU},i}(\zeta(t))_p. \quad (4.3)$$

In addition to the deep-driven subsidence from the homogeneous reservoir, the local subsidence, assumed to occur at shallow depths, can be modeled with a vertical displacement due to processes occurring at shallow depths, which have thus a short area of influence at the Earth's surface.

Shallow subsurface processes usually require models with a high spatial resolution with different physical processes depending on the soil type (Koster et al., 2018; van Asselen et al., 2018). Because we expect shallow drivers to correlate with precipitation and evapotranspiration if they relate to soil motion, η in this chapter is assumed to be a function of meteorological data. According to the soil water content, we observe uplift in winter and subsidence in summer (e.g., higher water content in winter than in summer). Soil water content and, thus, shallow drivers of subsidence vary when temperature changes. In this chapter, we test two models with 1) η correlating with precipitation and evapotranspiration and 2) η correlating with atmospheric temperature

$$\eta(t) = \begin{cases} u_{\text{u}}^{\text{shal}}(\mathbf{x}, P(t), E(t)), \\ u_{\text{u}}^T(\mathbf{x}, T(t)). \end{cases}$$

The shallow-driven subsidence, $u_{\text{u}}^{\text{shal}}(x, P(t), E(t))$, is the soil compaction, assumed to be related to soil moisture and determined by precipitation, $P(t)$, and evapotranspiration, $E(t)$ with scale factor \mathbf{x} . Subsidence $u_{\text{u}}^T(x, T(t))$ correlates with the averaged atmospheric temperature of the Netherlands, $T(t)$. The empirical SPAMS model shows good agreement with subsidence time series from extensometer data (Conroy et al., 2023) and provides a shallow-driven subsidence model without prior knowledge of the soil type. Using SPAMS allows us to reduce the model complexity for the shallow subsurface in the Groningen region. We apply the SPAMS model with a 2×2 km resolution at the Earth's surface (Fig. 4.1). This model is introduced in Section 2.3.2 and provides an expression for the vertical displacement, $u_{\text{u}}^{\text{shal}}$, which is the sum of a

reversible subsidence component, R , and a long-term subsidence component, I ,

$$u_u^{shal}(\mathbf{x}, P(t), E(t)) = R(x_P, x_E, P(t), E(t)) + I(\mathbf{x}, P(t), E(t)), \quad (4.4)$$

where the $\mathbf{x} = \{x_P, x_E, x_I\}$ are scaling factors that can vary per location. Conroy et al., 2023 define $I(\mathbf{x}, P(t), E(t))$ as the *irreversible* component. In the following, we use the term *long-term* subsidence because part of the long-term displacement, both in the shallow subsurface and in the deep subsurface (i.e., reservoir compaction), is elastic and thus possibly reversible. The component $R(x_P, x_E, P(t), E(t))$ in Eq. 4.4 is defined as *reversible* in Conroy et al., 2023 and is characteristic of the seasonal swelling of the soil and expressed as the function of the precipitation, $P(t)$, and the evapotranspiration, $E(t)$. We keep the term reversible to relate to the short-time variation in subsidence, e.g., uplift in winter and subsidence in summer, for consistency with the SPAMS model. The long-term component, $I(\mathbf{x}, P(t), E(t))$, is expressed as a function of a constant rate x_I and a step function f increasing in time given the difference between precipitation and evapotranspiration resulting in a water surplus. We refer the reader to Chapter 1 for more details on the SPAMS model.

Precipitation and evapotranspiration data are available from the KNMI (Koninklijk Nederlands Meteorologisch Instituut). For the area above the Groningen gas field, 21 stations provide daily precipitation data, and two stations provide daily evapotranspiration data. We choose the station of Nieuw Beerta as a reference for evapotranspiration and interpolate the precipitation data over a 2×2 km grid (Fig.4.1). We thus obtain daily interpolated maps of precipitation for the period of 2015 to 2020.

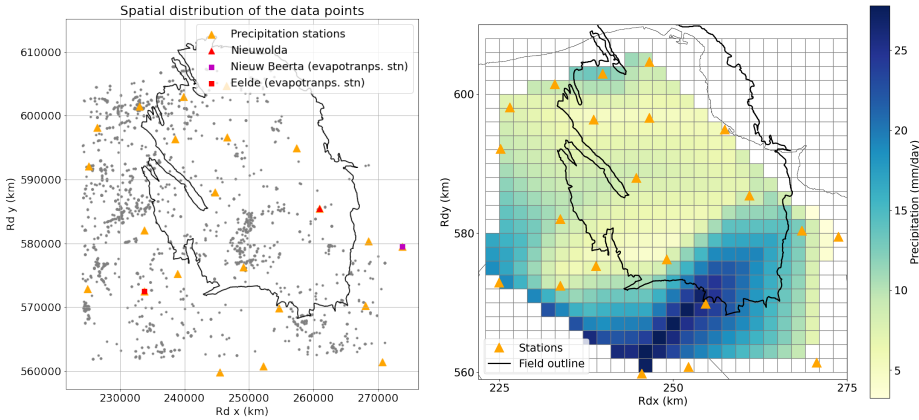


Figure 4.1: (Left) Spatial distribution of the PS averaged per parcel above the Groningen gas field (field outline in black solid line) with the location of the meteorological stations measuring precipitation (orange triangles) and evapotranspiration data (squares). Grey dots indicate observation points where PS-InSAR displacement estimates are averaged over a 250 m radius. (Right) Map of the area of the Groningen gas field showing the interpolation of the precipitation data (orange triangles) over the Groningen gas field with 2×2 km grid cells.

Seasonal variations of soil motion are correlated with seasonal temperature changes because soil moisture depends on temperature: subsidence occurs in summer when

temperature increases, i.e., when the soil is dry. A simple approach is to model the term η (Eq. 4.4) with the subsidence, u_u^T , where T is the daily averaged atmospheric temperature and $T(t)$ as defined in Chapter 1. Thus, in Eq. 4.1 the term η can represent a local subsidence, u_u^T , and for consistency with the SPAMS model, the subsidence u_u^T is defined as the sum of a reversible component R , and an long-term component, I ,

$$u_u^T(\mathbf{x}, T(t)) = R(x_\theta, T(t)) + I(x_I, T(t)). \quad (4.5)$$

In Eq. 4.5, x_θ is the scale factor, which correlates subsidence with temperature, and x_I relates to the irreversible subsidence component. The reversible component $R(x_\theta, T(t))$ is now

$$R(x_\theta, T(t)) = x_\theta T(t), \quad (4.6)$$

and the long-term component, I , is proportional to a step function $f[T(t)]$, such as:

$$I(x_I, T(t)) = \sum_{-\infty}^t x_I f(T(t)), \quad (4.7)$$

with

$$f(T(t)) = \begin{cases} 0, & \text{for } T(t) > 15^\circ\text{C (soil moisture increases)} \\ 1, & \text{for } T(t) \leq 15^\circ\text{C (soil moisture decreases),} \end{cases} \quad (4.8)$$

Similarly to the subsidence in the SPAMS model, which assumes increasing long-term subsidence when the evaporation is higher than the precipitation, we use the arbitrary threshold of 15°C for irreversible compaction, which correlates best with the soil dryness (Alvenäs and Jansson, 1997; Jansson, 1998).

4.3. INSAR DATASET REDUCTION FOR ASSIMILATION

InSAR is a technique to estimate the Earth's surface displacements, with the main advantage that the spatial and temporal distribution of observation points (PS) is much higher compared with leveling (Sec. 1.2). Starting in 1992, three different satellite missions acquired subsidence signals over Groningen every 2-3 days, and each InSAR dataset contains more than 1.5 million observation points. An InSAR displacement estimate is derived from the double difference (DD) phase observations, i.e., the phase relative to a reference point and a reference epoch. The observed phase is the sum of multiple components, e.g., the atmospheric phase, displacement phase, residual height phase, noise components, and an unknown integer ambiguity number (Hanssen, 2001). Thus, to obtain InSAR estimates, the displacement must be separated from other phase components that are not directly measured but derived from InSAR processing, as explained in Chapter 1.2. Additionally, since all scatterers can have unique scattering behavior, the quality of the observations is highly variable and not trivial to estimate (Chang and Hanssen, 2015; Ketelaar, 2009). We use coherent and strong reflections, so-called Point Scatterers (PS).

Because InSAR displacements estimated based on PS have complex reflections of the satellite signal on structures, we can not assume that InSAR is only sensitive to the deep drivers of subsidence. Instead, the InSAR displacement estimate is the sum of deep-

and shallow-driven subsidence with possible deformation signals, depending on the reflection of objects at the Earth's surface (e.g., the thermal expansion of infrastructures previously mentioned). We refer the reader to Chapter 1 for more details on the different subsidence processes such as geotechnical movements, deforming infrastructures like roads and railways, and the compaction of shallow soil layers also present in the InSAR estimates (Auriac et al., 2014; Chang and Hanssen, 2015; Fokker et al., 2019; Gharekhani et al., 2021; Ketelaar, 2009; Koster et al., 2018).

We propose the following approach to use InSAR vertical displacement in data assimilation. We average InSAR displacement estimates per parcel (Fig. 4.2) to represent the averaged displacement at the parcel scale. Parcel centroids are defined as *observation points* or *location points* in the following. We use both terms interchangeably. We reduce the dataset's size and the common noise in the PS-InSAR time series by averaging. The second advantage of the parcel average is that we can attribute a soil type per observation point using the geology of the Groningen area in Fig.4.2. The parcel average consists of the following:

1. We define a radius of 250m around each parcel centroid and spatially average the vertical displacement of the InSAR time series within this area. We obtain one time series per parcel centroid.
2. We select three of these averaged time series with a seasonal pattern attributed to the shallow-driven subsidence (i.e., subsidence in summer and uplift in winter). To test if the other time series averaged per parcel have a seasonal component, we test the correlation between the three selected time series and all other parcel-averaged time series. An InSAR time series without correlation with the three selected time series is rejected.
3. We grid the area as in Fig. 4.1 and sample one observation point per grid cell to avoid clusters of observation points with redundant information in areas with a dense distribution of PS, such as urban areas.

4.4. DATA ASSIMILATION METHODOLOGY

4.4.1. IMPORTANCE SAMPLING BACKGROUND

In our data assimilation subsidence problem, we choose the optimal proposal particle filter as described by Doucet et al., 2000; Snyder et al., 2015; van Leeuwen et al., 2015 and in Chapter 3. We start by defining the background knowledge of the physical process in the subsurface causing subsidence. This allows us to evaluate a range of potential values to sample the model states $x_{k-1}^i, i = 1, \dots, N_e$ at time $k-1$ and to sample the model states from the probability distribution $p(\mathbf{x}^{k-1}) \sim \mathcal{N}(m_x, \Sigma_x)$, where m_x represents the mean and Σ_x the covariance matrix. We recall the reader of the definition of the observation operator, \mathcal{H} , mapping the state space to the observation space and the forward model states with \mathcal{M} , as in Section 1.4.1

$$\begin{aligned} \mathbf{x}_k &= \mathcal{M}(\mathbf{x}_{k-1}) + \mathbf{e}_{k-1} \\ \mathbf{y}_k &= \mathcal{H}\mathbf{x}_k + \mathbf{e}_k, \end{aligned} \tag{4.9}$$

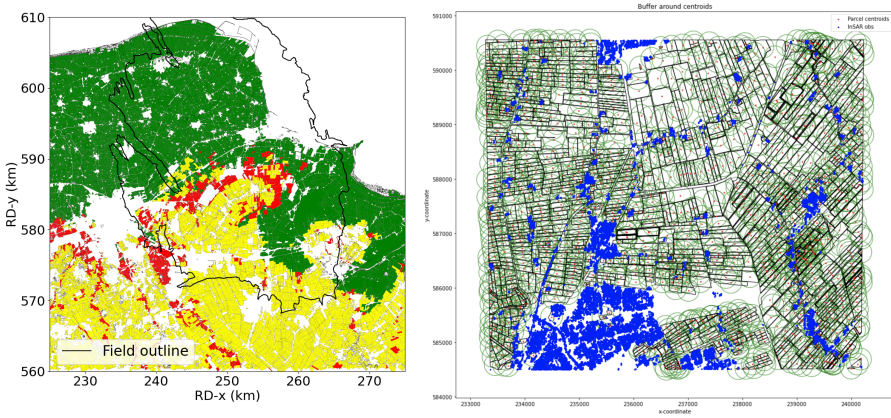


Figure 4.2: (Left) Map of the area of the Groningen gas field showing the approximation of the soil geology per parcel, with clay in the north (green), sand in the south (yellow), and peat areas (red). (Right) Zoom of the map at the parcel level showing parcel geometry over a smaller area above the gas field, with the parcel centroids indicated with a red dot. A circle of 250m radius from parcel centroids is defined, and all PS-InSAR displacement estimates within this perimeter are averaged.

with the model error $\mathbf{e}_k \sim N(\mu_e, \Sigma_e)$ and the measurement error $\epsilon_k \sim N(\mu_c, \Sigma_c)$. The covariance matrix Σ_e and Σ_c are assumed known.

4.4.2. ASSIMILATION OF INSAR TIME SERIES

The particle filter is a sequential method (Fig.1.22 Sec. 1.34), in which a model evolves in time, performing a model update when a new observation is available. This assumes a Markov process, in which the model at time k only depends on the model at time $k - 1$. Until now, we have assimilated the InSAR dataset using vertical displacement velocities because the cumulative displacement of the InSAR time series can vary with very large noise variation between two consecutive epochs. The noise can give displacement difference up to 10mm between two observations in 6-day intervals. This strongly influences the posterior estimate when using a sequential assimilation scheme. However, we expect that assimilating time series of cumulative displacement can provide information on the seasonal variation of the subsidence signal and, consequently, improve the accuracy of subsidence forecasts.

Compared to the standard particle filter in Section 1.4.3 Fig. 1.22, we now assimilate cumulative displacements using all InSAR epochs of an assimilation window rather than an averaged displacement velocity at the end of the assimilation window. InSAR cumulative displacements are relative to the first epoch of the time series, with a new epoch every six days. Therefore, we assimilate all epochs of the InSAR time series in an assimilation window of one year (Fig. 4.3). Figure 4.3 gives a schematic representation of an InSAR time series with cumulative vertical displacement, indicated with black dots and error bars at all epochs. In this example, the time series is split into three assimilation windows of one year each, and a subsidence forecast is performed after the third assimilation. In contrast with the sequential assimilation of the particle filter

depicted in Figure 1.22, in Figure 4.3, all InSAR cumulative displacement estimates (black dots) of the assimilation window are used in the assimilation step. This allows the use of information about all displacement values of the time series in this assimilation window, similar to a smoother approach generally used in ensemble smoothers for reservoir engineering (see, for example, Evensen et al., 2022, Sec. 2.4.4 Fig. 2.4).

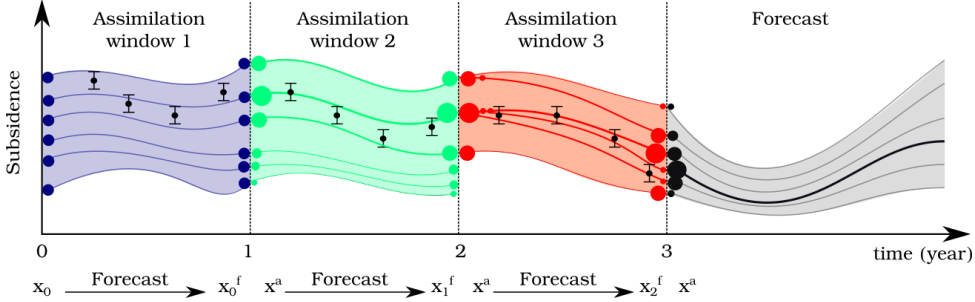


Figure 4.3: Schematic principle of the data assimilation framework with InSAR cumulative displacement estimates. The analysis is performed at the end of each assimilation window, considering all data in the assimilation window (e.g., with the subsidence rate of the time series). Dots at the end of the assimilation windows illustrate the particle ensemble, and the size of the dots at the beginning of the next window represents the value of the particle weight. The second update (after the assimilation window 2) illustrates a resampling step. At the end of the assimilation window 3, an ensemble forecast from the last analysis can be performed (black line). This representation of the particle filter resembles Figure 1.22, but in contrast to the particle filter introduced in Section 1.34, all epochs from InSAR time series are assimilated within an assimilation window.

4.4.3. SEPARATION SUBSIDENCE REGIMES

In a system with a compacting reservoir and a shallow layer of soil causing subsidence, we formulate the state vector based on our nucleus of strain model for the reservoir compaction and the SPAMS model for the shallow-driven subsidence,

$$\mathbf{x} = \left. \begin{array}{l} \zeta \\ x_{E,i} \\ x_{P,i} \\ x_{I,i} \end{array} \right\} \text{SPAMS parameters for each grid cell } i = 1, \dots, N_y. \quad (4.10)$$

where ζ is the reservoir compaction, which is an uncertain model state, x_E , x_P , and x_I are the uncertain parameters of the SPAMS model (Eq. 4.4). The reservoir compaction is assumed homogeneous with the same compaction ζ for all reservoir grid cells, while each model grid cell at the Earth's surface, i , has different parameters $x_{E,i}$, $x_{P,i}$, and $x_{I,i}$. In the data assimilation, each particle provides a subsidence model realization m , $m = 1, \dots, N_e$ for particles $\mathbf{x}^m = [\zeta^m(t), x_{E,i}^m, x_{P,i}^m, x_{I,i}^m]$. Therefore, from the state vector \mathbf{x} in Eq. 4.10, we model the shallow-driven subsidence for each grid cell independently and add the deep-driven component to obtain the total vertical displacement $u_i(t) = u_i^{deep}(\zeta(t)) + u_i^{shal}(\mathbf{x}_i, P_i(t), E_i(t))$ in each grid cell over the area.

To identify the deep- and shallow-driven subsidence, we use the following assumptions:

- Temporally, with an assimilation window of one year, we assume that deep-driven subsidence varies linearly in time, whereas shallow-driven subsidence has seasonal variability shorter than one year.
- Spatially, over the Groningen area, the subsidence signal has spatial characteristics: the deep-driven subsidence signal has a typical smooth subsidence bowl over the area, whereas shallow-driven subsidence is spatially heterogeneous.

In the data assimilation analysis step, we use this spatial correlation (smoothness) in the subsidence bowl to constrain the estimate of the reservoir compaction, ζ . This imposes that the generated subsidence field from the prior values of ζ best fits the InSAR displacement velocity over the area, thereby without modeling any shallow-driven subsidence. In the second part of the analysis, we model a time series of cumulative displacement at each observation point, including deep- and shallow-driven subsidence, and compare this modeled time series with the InSAR time series. The procedure is described in Algorithm 3 and consists as follows.

4

The amount of reservoir compaction over the one-year assimilation window provides a compaction rate (i.e., a certain amount of compaction per year). The compaction is assumed to be homogeneous in the entire reservoir. From this compaction rate, we apply the forward model based on the nucleus of strain, defined previously in Section 4.2, and we compute with Eq. 4.2 a displacement velocity (i.e., amount of displacement per year). This modeled displacement velocity is attributed to the deep-driven subsidence. The Groningen region is discretized into grid cells of 2km resolution (Fig. 4.1), and the displacement velocity is computed in each grid cell, resulting in a modeled subsidence field with spatial correlation (i.e., smooth subsidence bowl). In the data assimilation analysis step, we compare the InSAR displacement velocity to the modeled displacement velocity computed from the compacting reservoir. The L2-norm, δ_0 , of the difference between the InSAR and the modeled velocity is calculated over all grid cells of the area (Alg. 3). Consequently, each particle corresponds to an L2-norm, given that its compaction value represents the spatial correlation in the InSAR subsidence signal. From the same particle, we model the time series of cumulative displacement with deep- and shallow-driven subsidence, providing a modeled time series of vertical displacement in each grid cell at the Earth's surface and all epochs of the assimilation window. In the analysis step in the data assimilation (Alg. 3), we compare the InSAR time series of cumulative displacement with this modeled time series at all epochs in a data assimilation window, Δt . The time-averaged difference, δ_i , between the modeled time series and the InSAR time series is computed for all particles. Finally, the L2-norm δ_0 and the time-average difference δ_i are included in the analysis through Bayes' theorem to attribute a weight to the particles.

Algorithm 3 Data assimilation framework with InSAR time series including deep- and shallow-driven subsidence illustrating the prior sampling and the application of the forward model (FM) to the state vector with a reservoir model based on the nucleus of strain (NS) and the SPAMS model (SPAMS). The L2-norm, δ_0 , and the time-averaged difference, δ_i , over the assimilation window Δt are computed and incorporated in the likelihood in the analysis step. Note that in the likelihood, the term δ_0 is a sum over all observations, and δ_i is assumed independent between grid cells and does not involve a sum over all observations.

Sampling: generate an ensemble of dimension N_e for the state vector $[\zeta, x_p(i), x_e(i), x_I(i)]$, with $i = 1 \dots N_y$ the number of grid cells.

Forecast: $t_k \rightarrow t_{k+1}$

for $m = 1 : N_e$ **do**

for $i = 1 : N_y$ **do**

$$\zeta \xrightarrow{NS} \begin{cases} u_{m,i}^{deep} \\ \dot{u}_{m,i}^{deep} \end{cases},$$

$$[x_{P,m,i}, x_{E,m,i}, x_{I,m,i}] \xrightarrow{SPAMS} \begin{cases} u_{m,i}^{shal} = u_{m,i}^{shal,R} + u_{m,i}^{shal,I} \\ \dot{u}_{m,i}^{shal,I} \end{cases}$$

→ Compute the dynamical model with deep- and shallow components:

$$u_{m,i}(t) = u_{m,i}^{deep}(\zeta(t)) + u_{m,i}^{shal}(x_{m,i}, P_i(t), E_i(t))|_{\Delta t}$$

→ Compute the subsidence rate with deep and shallow components:

$$\dot{u}_{m,i} = \dot{u}_{m,i}^{deep} + \dot{u}_{m,i}^{sh,I}$$

→ Compute the time-averaged difference between the modeled time series of vertical displacement and the InSAR time series over N epochs for the particle m in the cell i

$$\delta_i = \frac{1}{N} [(y_i - u_{i,m})]_{\Delta t}^2$$

end for

→ Compute the L2-norm, δ_0 , of the difference between the modeled subsidence and the InSAR displacement velocities over the N_y cells and for each particle m ,

$$\delta_{0,m} = \frac{1}{N_y} \left[\sum_i^{N_y} (\dot{y}_i - \dot{u}_{i,m}) \right]^2$$

end for

Analysis: estimation of $[\zeta, x_p(i), x_e(i), x_I(i)]$

→ Compute the likelihood for each particle m

$$p(y | [\zeta, x_p(i), x_e(i), x_I(i)]_m) \propto \exp \left[-\frac{1}{2} (\delta_{0,m} \Delta t^2 + \delta_i) \right]$$

→ Apply the likelihood as a weight to each particle m using δ_0 and δ_i .

4.5. PROOF OF CONCEPT WITH SYNTHETIC EXPERIMENTS

4.5.1. SYNTHETIC EXPERIMENT SET-UP

We test the data assimilation methodology in synthetic experiments based on the same principle as the synthetic experiments in Chapter 2. The motivation for synthetic experiments is that we generate a *truth*, \mathbf{x}^{truth} , which represents the unknown quantities that we aim to estimate. This approach allows us to validate the data assimilation result by comparing the data assimilation estimate to the synthetic truth. The state vector in this synthetic experiment is the state vector as defined in Eq. 4.10, with the model state of compaction, ζ for the deep-driven subsidence and the model parameter of the SPAMS model for the shallow-driven subsidence. We discretize the region of interest at the Earth's surface into N_x grid cells of 2×2 kilometers each (Fig. 4.1). In these synthetic experiments, we simulate synthetic data, $\tilde{\mathbf{y}}$, representing the total displacement with deep-driven subsidence from the reservoir compaction model and with the shallow-driven subsidence from the SPAMS model. We add a Gaussian noise with a 1 mm standard deviation. To assess the accuracy of the data assimilation analysis, we compare the analysis, i.e., the expected mean of the posterior distribution, to the truth.

We perform two tests: one is quasi-static, and one is time-varying. In the first quasi-static, we test the separation of deep- and shallow-driven subsidence using a simplification of the proposed data assimilation approach. We do not assimilate the InSAR time series of vertical displacement, only the InSAR linear displacement velocity. This test allows us to verify if we can separate the deep- and shallow-driven subsidence with a particle filter over a single update step by using the fact that the deep-driven subsidence has a smooth subsidence bowl and that the shallow-driven subsidence is spatially independent. This case also resembles the assimilation of leveling displacements in the experiments in Chapter 3, Section 3.4, but with the difference that we now add a second subsidence driving mechanism.

In a second test, we use a dynamical model to simulate the cumulative displacement of the InSAR time series (Eq. 1.24). We simulate deep-driven subsidence based on the NAM estimation for the reservoir pressure (Chap.3) and model the time evolution of the shallow-driven subsidence with the SPAMS model (Fig. 4.1).

4.5.2. SEPARATION OF DEEP- AND SHALLOW-DRIVEN SUBSIDENCE

For the synthetic quasi-static test, we estimate the state vector and update the modeled subsidence at time t_k using the initial conditions of no compaction and no subsidence, e.g., before the start of production at time t_{k-1} , and then simplify the shallow-subsurface model by defining a stochastic term, η (Eq. 1.4.1). We simulate synthetic displacement estimates with ten years of hydrocarbon production, with an equivalent mean pressure reduction of $\Delta P = 5$ MPa in the reservoir. We choose model inputs to mimic the Groningen gas field assuming a constant compaction coefficient of $C_m = 1.24 \times 10^{-4} \text{MPa}^{-1}$ and a reservoir height of $h = 240$ m (Bourne et al., 2014; Fjaer et al., 2008; Hettema et al., 2000), resulting in an annual compaction rate of 0.15 m/year. We simplify the soil geology of the region of Groningen (Fig. 4.2) and create a synthetic

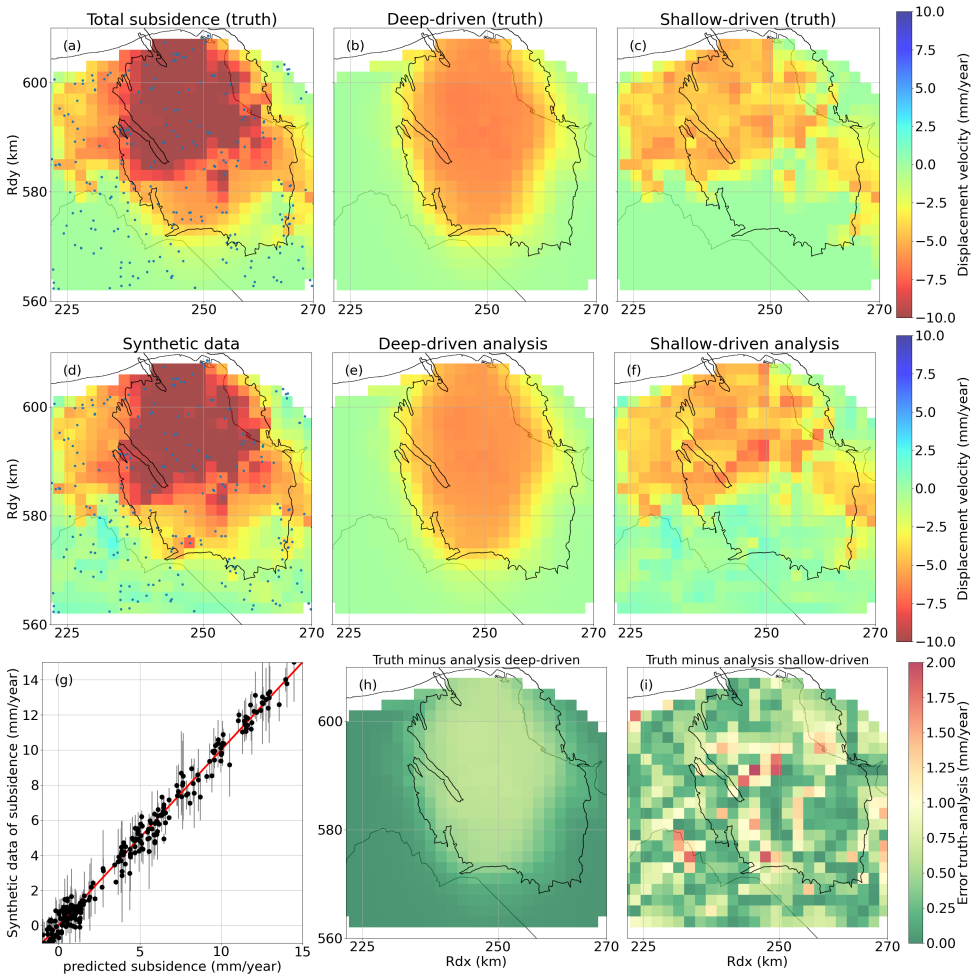


Figure 4.4: Synthetic experiments for the quasi-static example. A true deep- and shallow-driven subsidence is simulated in (b) and (c), and the sum of the two is shown in (a). From the true total displacement in (a), we create synthetic subsidence data by adding a synthetic measurement error, see (d). Dots indicate the location of the observation, i.e., synthetic Point Scatterer in InSAR. Assimilation of synthetic data in (d) provides analysis for the deep- and shallow-driven subsidence in (e) and (f). Figure (g) shows the comparison between the synthetic data and the analysis, with error bars indicating the measurement error in the synthetic data at each observation point. (h) and (i) show the absolute error between the analysis and the truth for both the deep- and shallow-driven subsidence, quantifying the analysis's fit to the truth.

clay shrinkage with a displacement velocity in the north from a Gaussian density with a mean $\eta = -5$ mm/year, whereas the peat and sand areas in the south, in this synthetic case, are not compacting ($\eta = 0$ mm/year). We compute subsidence from \mathbf{x}^{truth} for the deep- (Fig. 4.4b) and the shallow-driven subsidence (Fig. 4.4c). The total subsidence is the sum of the deep and shallow components (Fig. 4.4), and from the total subsidence, we generate the synthetic displacements $\tilde{\mathbf{y}}$ (Fig. 4.4d).

We consider a data-assimilation system (Eq. 4.1) with a Gaussian model and measurement errors. We generate a prior state of compaction using the prior “optimal” proposal density from Eq. 3.9. The prior states η are sampled from a uniform distribution. We have limited background knowledge of processes in the shallow subsurface; for reasons of simplicity, we assume a uniform distribution of η . We sample particles with an ensemble size, $N_e = 1000$, and assimilate synthetic linear displacement velocities spatially over $N_y = 268$ observation points at each assimilation step of one year (Sec. 4.5.1). Figure 4.4a illustrates the synthetic displacement velocity over the Groningen region with a model resolution of 2 km grid cell. The displacement velocity in Fig. 4.4a is a total subsidence computed by adding the simulated synthetic deep-driven subsidence (Fig. 4.4b) and the shallow-driven subsidence (Fig. 4.4c). The synthetic observation points for the assimilation are indicated with blue dots and show a homogeneous coverage over the area.

4

The assimilation results in Fig. 4.4 e and f show a correct separation of the characteristic bowl-shaped subsidence and the compacting clay. To evaluate the error in the analysis, Fig. 4.4g shows the synthetic data as a function of the total subsidence analysis. The error bars in grey represent the simulated measurement error, ϵ , at each location with a spread of approximately $[-2, 2]$ mm, corresponding to 2σ of the measurement error introduced in the synthetic data. The difference between subsidence analysis (Fig. 4.4e and f) and synthetic displacements (Fig. 4.4d) gives a spread of the same order of magnitude as the measurement error ϵ . Figures 4.4h and i show the absolute error between the analysis $\hat{\mathbf{x}}$ and the truth, \mathbf{x}^{truth} for the deep- (h) and shallow-driven (i) subsidence. As expected from the smooth subsidence bowl generated with the synthetic truth, in Fig. 4.4h, the error in the compaction analysis ζ gives an error in the updated subsidence in the shape of the modeled subsidence bowl, and has an error in the spatial gradient of the displacement field less than 1 mm/year. The residual of the shallow-driven subsidence analysis in Fig. 4.4i has a random character, i.e., without spatial correlation (Sec. 2.3.1), which is not surprising given our assumption on the local effect of shallow processes on the subsidence field. We observe a heterogeneous error distribution in Fig. 4.4i, which averages below 2 mm/year with a root mean square error (RMSE) in the analysis of 1 mm between the predicted total subsidence and the synthetic displacement, falling within the range of the introduced measurement error ϵ . The RMSE of the truth relative to the predicted shallow-driven subsidence is also 1 mm.

We now create a synthetic time series for each observation location of the second test with a dynamical model and introduce a seasonal variation in the shallow component of this synthetic truth. In this second test with a dynamical model, we sequentially update the model at the end of each assimilation window as illustrated in Fig. 4.3. In Figure 4.5, we show how we create shallow-driven subsidence in the synthetic displacements to mimic InSAR displacement estimates with a seasonal variation. Figure 4.5a shows a map of the true displacement velocity for the shallow-driven subsidence and equivalent time series for two specific locations (indicated with stars in Fig. 4.5). These displacement time series are simulated for deep-driven subsidence with an exponential time decay of compaction. Dotted lines show the shallow-driven subsidence with the seasonal pattern for the reversible component and a *step function* for the long-term component. The total modeled subsidence, as represented in the solid line in Fig. 4.5, is the sum of the deep-

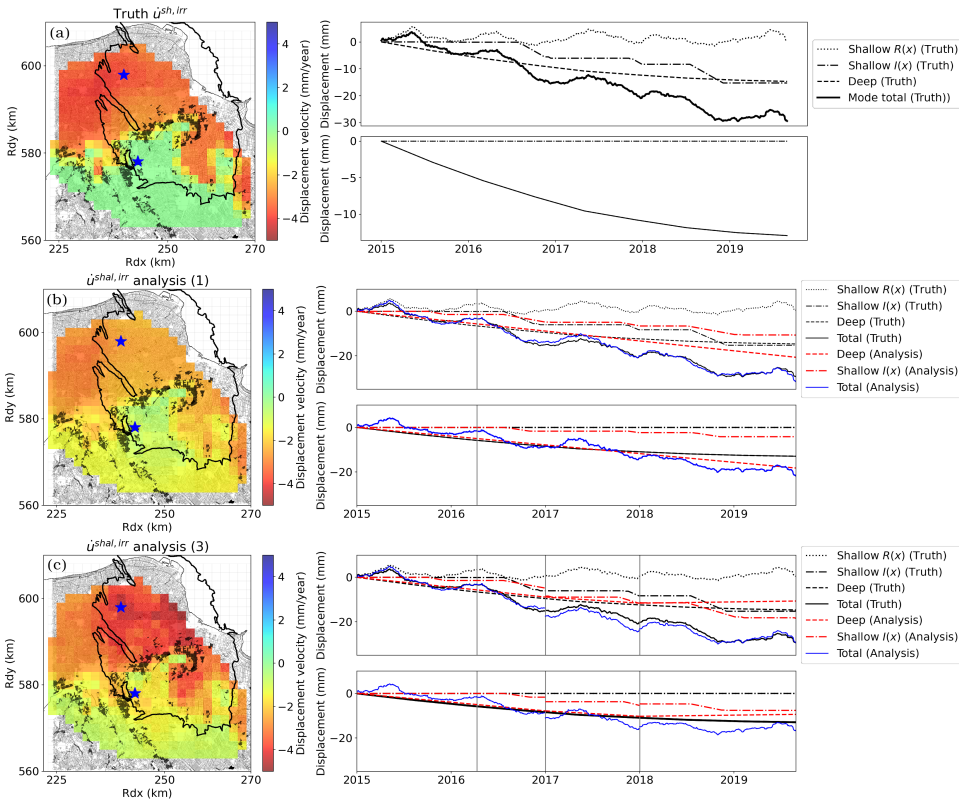


Figure 4.5: Modeled shallow displacement velocity updated from the data assimilation analysis in a synthetic test. Synthetic subsidence time series are modeled with deep (dashed line) and shallow-driven subsidence (dotted line). Displacement time series are shown for two locations, which are indicated with blue stars on the map. The first row (a) shows the truth (black lines). The second row (b) shows the model update from the data assimilation analysis (blue lines): the model is updated after one assimilation step. The third row (c) shows the model update after resampling, followed by a third assimilation step in 2018.

and shallow components.

We perform assimilation steps in January 2016, 2017, and 2018 with the data-assimilation framework of Section 4.4 and test if we can retrieve the deep- and shallow-driven subsidence components with the data assimilation. The subsidence model updated from the estimated compaction, in Fig. 4.5b, shows good agreement between analysis and truth for the north, i.e., for the location indicated with the star. In the south, the exponential decay of the deep-driven subsidence is correctly estimated but exhibits shallow-driven subsidence, which does not exist in the simulated truth. Figure 4.5b shows the map for the analysis of the shallow-driven subsidence as an averaged displacement velocity. Comparison with the truth in Fig. 4.5a shows the correct pattern of the compacting clay with an overestimation of subsidence over the area of Groningen with an error for the deep-driven subsidence, with a similar error in the gradient of the subsidence bowl as in Fig. 4.4h.

Errors in the analysis can come from constructing the prior distribution covering values for compacting and non-compacting clay. Indeed, in our example, subsidence occurs in the north but has a zero value in the south. To appropriately represent the solution space, the prior ensemble is sampled with a spread that covers all possible subsidence values between -5 mm and 0 mm. Because of the range amplitude of the possible values, particles far from the truth influence the expected mean of the posterior, which can lead, in some cases, to a bias in the estimate. This error in the deep-driven analysis leads to an overestimation of the parameter x_I in some locations to fit the observations and compensate for the error in the deep-driven subsidence analysis. To avoid this compensation taking place, we performed a re-sampling step before the subsequent assimilation window. Figure 4.5c shows the analysis result after the re-sampling step with a map of the shallow displacement velocity. The figure shows a better resemblance of the analysis with the truth in Fig. 4.5a than was the case without the re-sampling step (Fig. 4.5b). In this case, the resampling step allows us to reduce the variance in the prior ensemble. Results from the synthetic tests in this section illustrate our proposed method for separating deep—and shallow-driven subsidence and how errors in measurement and model propagate into the analysis.

4.6. APPLICATION TO THE GRONINGEN REGION WITH REAL GEODETIC DATASETS

For an ultimate application of data assimilation with real InSAR time series at the scale of the Groningen gas field, it is not straightforward to model and approximate all processes contributing to the subsidence. In particular, defining a model to represent the physical processes in the shallow subsurface through the term η is not straightforward (Eq. 4.1 in Sect. 4.2). Chapter 1 presented the subsidence driving mechanisms in the Netherlands, and more specifically in the Groningen region, and Section 4.2 provided possible driving mechanisms for the shallow-subsurface, such as variations in soil water content related to precipitation and temperature changes. Based on the known driving mechanisms, I explore the estimation of subsidence-driving mechanisms for 1) η correlating with soil water content and 2) η correlating with the averaged temperature of the Netherlands. Before testing the assimilation with actual InSAR data, I evaluate the assimilation approach by assimilating leveling data into the subsidence model of Section 4.2.

We have previously estimated the compaction field and the modeled subsidence from the compaction field with leveling data in Chapter 3. Figure 4.6 shows the result of subsidence estimation with the method of Chapter 3, with a heterogeneous reservoir and leveling-based displacement estimates. In the case of heterogeneous reservoir compaction, in Fig. 4.6, the nuclei of strain have mutually independent compaction values, but the resulting subsidence field has spatial correlations as the subsidence at each location at the surface is a result of all nuclei of strain at the reservoir level. Based on the compaction model in Section 4.2, we evaluated the evolution of the compaction field assimilating leveling-based displacement estimates from 1987 to 2018, relative to 1978 (Chapter 3). The subsidence field results of this data assimilation analysis agree with the history of the gas field with increased compaction in the north (Fig. 4.6). The compaction

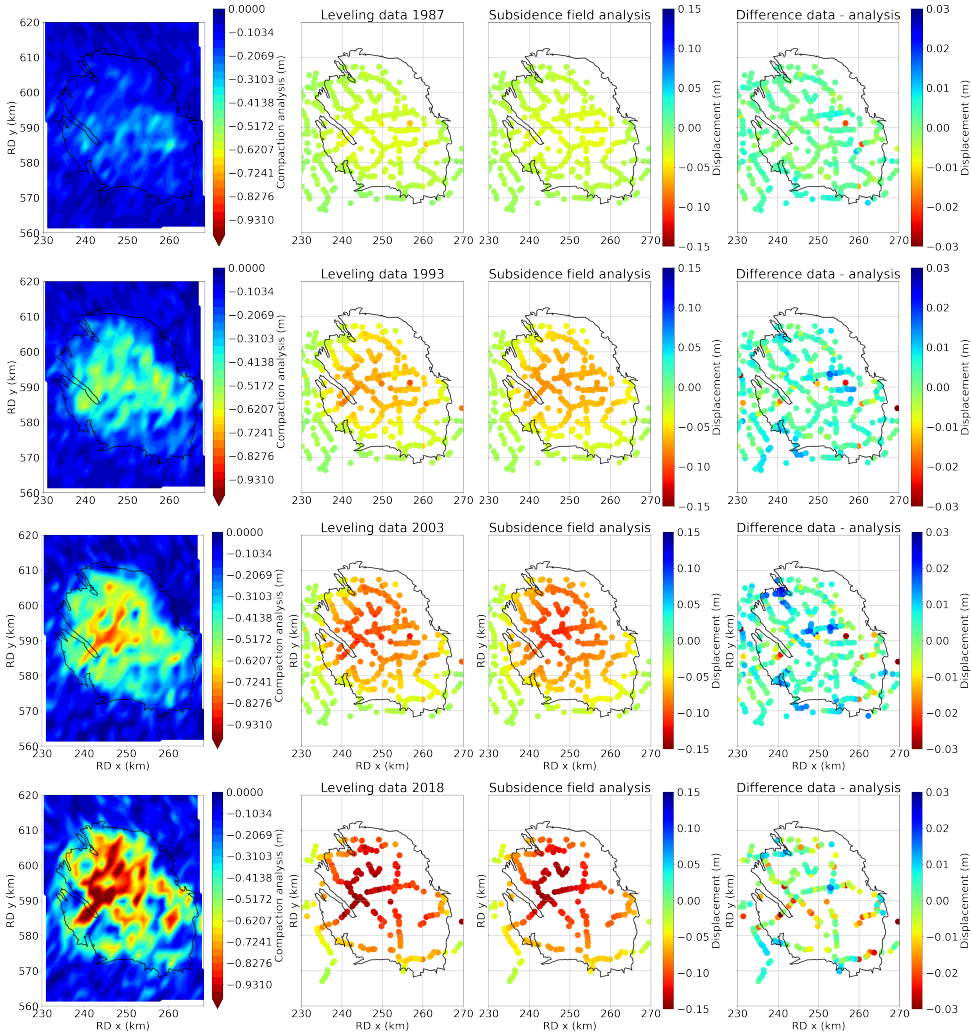


Figure 4.6: (First column) Time evolution of the reservoir compaction estimated from the leveling data with the particle filter (Chapter 3) at the date of 1987, 1993, 2003, and 2018. The third and fourth columns show the modeled subsidence based on the compaction estimates and the error between the leveling data and the model subsidence.

analysis 2018 shows increased compaction in the north and at specific locations in the south, which also agrees with the production plan of 2014 (NAM, 2016). Indeed, in 2014 the gas production was reduced in the north of the gas field and increased in the south to reduce the pressure gradient in the reservoir. For example, with the closure of the production cluster Loppersum.

The update of modeled-subsidence field analysis in Fig. 4.6 shows a reasonably good agreement with the leveling displacement estimates. The outliers we observe in the

differences between the leveling data and the data assimilation analysis show possible outliers and reveal measurement errors or other sources of errors, such as benchmark instability. In the following, the results with leveling data are used as a reference for the deep- and shallow subsidence analysis obtained with InSAR.

4.6.1. CORRELATION OF SUBSIDENCE WITH SOIL WATER CONTENT

After the test with leveling data, we explore the assimilation of actual InSAR estimates into a model for the Groningen region. In this exploration, I test the separation of deep- and shallow-driven subsidence using a subsidence model that combines a homogeneous reservoir and the SPAMS model. Background knowledge of gas production (Chapter 3) provides inputs to compute the deep-driven subsidence with the dynamical model. I consider hydrocarbon production for the period from 2015 to 2020. Production observations show that the gas extraction was reduced after 2014, and the average mean pressure variation in the reservoir had a rate of -0.01 MPa/year to less than -0.005 MPa/year in the period between 2015 to 2020. Values of the scale factors x_E , x_P , and x_I for the shallow-driven subsidence (Eq. 4.10) are chosen from a previous test at the station Nieuwolda (Chap. 1). In this test in Section 1.3.2, Figure 1.18, I showed that the modeled shallow-driven subsidence with the SPAMS model matches the time-varying subsidence signal in InSAR. In Figure 4.7, the time series of cumulative displacement shows a comparison of the InSAR displacement estimates (in grey) with the displacement analysis from data assimilation for the total subsidence (in blue). Maps of the displacement velocity show the data assimilation estimates of the shallow-driven displacement velocity associated with the subsidence over the Groningen region.

We assimilate InSAR displacement estimates until a given assimilation step t_k (vertical grey lines), and from t_k onward, we let the forward model produce a subsidence forecast without assimilating any further data. The resulting subsidence forecasts show good agreement with InSAR estimates of that period, as shown in Fig. 4.7, which were not included in the analysis. The subsidence forecast indicated in blue in Fig. 4.7 represents the total subsidence, which is the sum of the subsidence forecast for deep-driven and shallow-driven subsidence (i.e., indicated with red dotted lines).

I select two locations (Fig. 4.7, as indicated with purple stars) to illustrate the subsidence forecast. In this example, locations in the north and center of the gas field correspond to clay and peat areas because we expect peat and clay soils to be more sensitive to soil water content changes than sand. This allows to illustrate the seasonal variation in the subsidence forecasts. I detail the result first for the deep-driven subsidence and then for the shallow-driven subsidence.

The deep-driven subsidence component is updated at the end of each assimilation window based on the reservoir compaction analysis, ζ . Values of the reservoir compaction analysis, ζ , in Tab.4.1, show aligns with the trend in gas production in this period, of approximately 33 Bcm/year (NAM, 2016) with slightly larger magnitude of the reservoir compaction and with the compaction estimates from leveling (Fig. 4.6). The deep-driven subsidence analysis derived from the compaction analysis, ζ , gives a maximum of 20 mm subsidence in 4 years, which is larger but still consistent with the subsidence forecast of NAM, 2016 and van Elk et al., 2021. The model update and

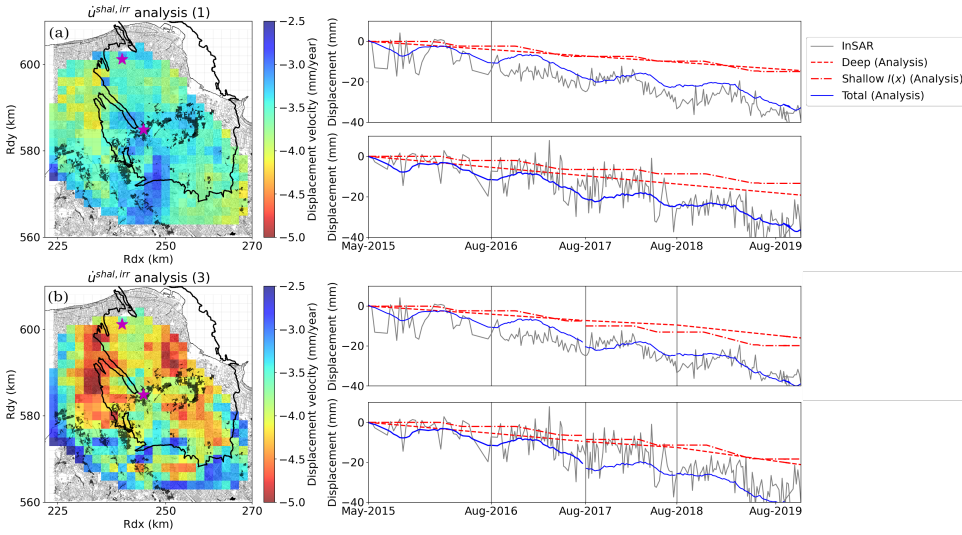


Figure 4.7: (Left panel) Map of modeled shallow-driven displacement velocity derived from the data-assimilation analysis. Purple stars indicate two observation points in clay (north) and peat areas (black-colored parcels). (Right panel) Time series of cumulative displacement at the indicated observation points: for map (a), the top subplot time series corresponds to the observation point in the north (in clay), and the bottom subplot corresponds to the observation point in peat. The same applies to map (b). Grey time series indicate the InSAR vertical cumulative displacement, and vertical grey solid lines indicate the date of the data-assimilation steps: for each assimilation window, only the InSAR displacement in that window is assimilated, and the other part of the InSAR time series is indicated to validate the data-assimilation analysis. The data-assimilation analysis is indicated in the red-dashed line for the deep-driven subsidence and in the dash-dot for the shallow-driven subsidence. A blue solid line indicates the data-assimilation analysis for the total subsidence. The map and time series in (a) show the data assimilation analysis after the first assimilation window in 2016, and the map and time series in (b) show the data assimilation analysis after the third assimilation step in 2018.

forecasts after the assimilation window show the total subsidence (Fig. 4.7, blue line) with a seasonal periodicity, which follows the general trend of the InSAR displacement estimates. However, after three assimilation windows of 1 year each, where we assimilated InSAR velocities and cumulative displacement with the approach described in Alg. 3, the subsidence forecast does not improve. The subsidence forecasts provide displacement velocities (i.e., subsidence rate) that follow the long-term trend of the InSAR time series but do not accurately match the seasonal signal in the InSAR time series. Moreover, the forecasts provide cumulative displacements with an amplitude of the seasonal variation smaller than expected in the actual InSAR time series. A possible explanation could be that the parameter x_I in the SPAMS model has not been correctly estimated, which is required to calculate the spatially averaged L2-norm, δ_0 (i.e., large-scale subsidence). Consequently, the error in the estimation of x_I propagates in the estimation of x_E and x_P , and underestimation of x_E and x_P results in low amplitude of the modeled vertical cumulative displacements.

The subsidence maps in Fig. 4.7 show the displacement velocity attributed to the long-term shallow-driven subsidence. After several assimilation steps, the subsidence

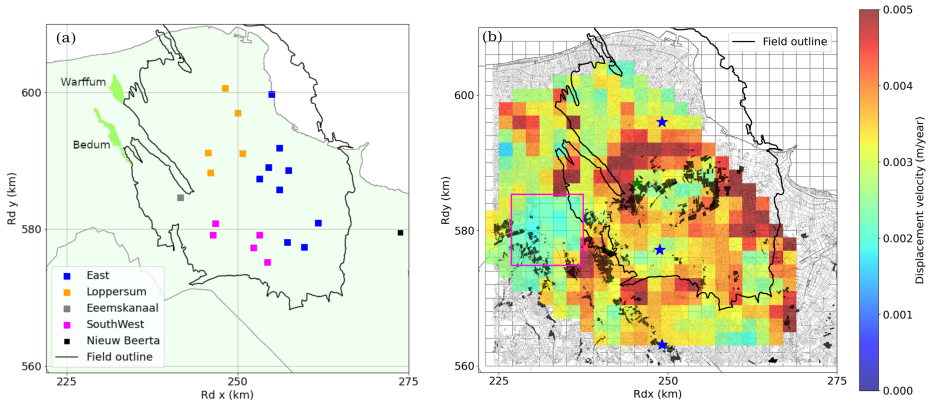


Figure 4.8: (a) Map of the Groningen region with the production clusters as defined by the producer in NAM, 2016. The gas fields of Bedum and Warffum that produce gas are indicated in green. (b) A map of the RMSE in the InSAR time series is computed with the difference at each epoch of the displacement and a running average of the time series. This RMSE shows the dispersion of the subsidence observation in time and thus relates to the quality of the InSAR Point Scatterer (i.e., reflection with good coherence in time). The magenta square indicates the city of Groningen, where point scatterers are reflected mainly on buildings, which gives a very coherent signal and low RMSE

map of the long-term shallow-driven subsidence shows a more defined pattern, highlighting areas with higher subsidence rates (Fig. 4.7). Interestingly, the subsiding areas outside the contour field of the reservoir are not observed in the leveling data. The locations with high displacement velocity on the map in Fig. 4.7 could correspond to production clusters outside the Groningen gas field, with other producing fields, Bedum and Warffum, and in the western, to urban regions, with, for example, the city of Groningen (Fig. 4.8). The subsidence pattern in the southeast of the reservoir, in Fig. 4.7, could be interpreted as deep-driven subsidence in agreement with the compaction field obtained with our assimilation of leveling in 2018 (Fig. 4.6) and with the inversion of the compaction field performed in Smith et al., 2019.

4.6.2. CORRELATION OF SUBSIDENCE WITH TEMPERATURE

In a second test, we apply the same methodology with a homogeneous reservoir, but instead of the SPAMS model, we model shallow-driven subsidence as a function of the averaged atmospheric temperature of the Netherlands. We assume, as explained in Section 4.2 that shallow-driven subsidence indirectly depends on the atmospheric temperature because of the soil water content seasonal variation.

In Figure 4.9, a map of displacement velocity shows the data assimilation analysis for the long-term shallow-driven subsidence. I chose locations in the north (with clay) and the south (with sand) of the gas field because I want to test whether the seasonal variation is correctly and better estimated than in the test with the SPAMS model, in which we suspected the parameter x_I to influence the amplitude of the seasonal signal in the

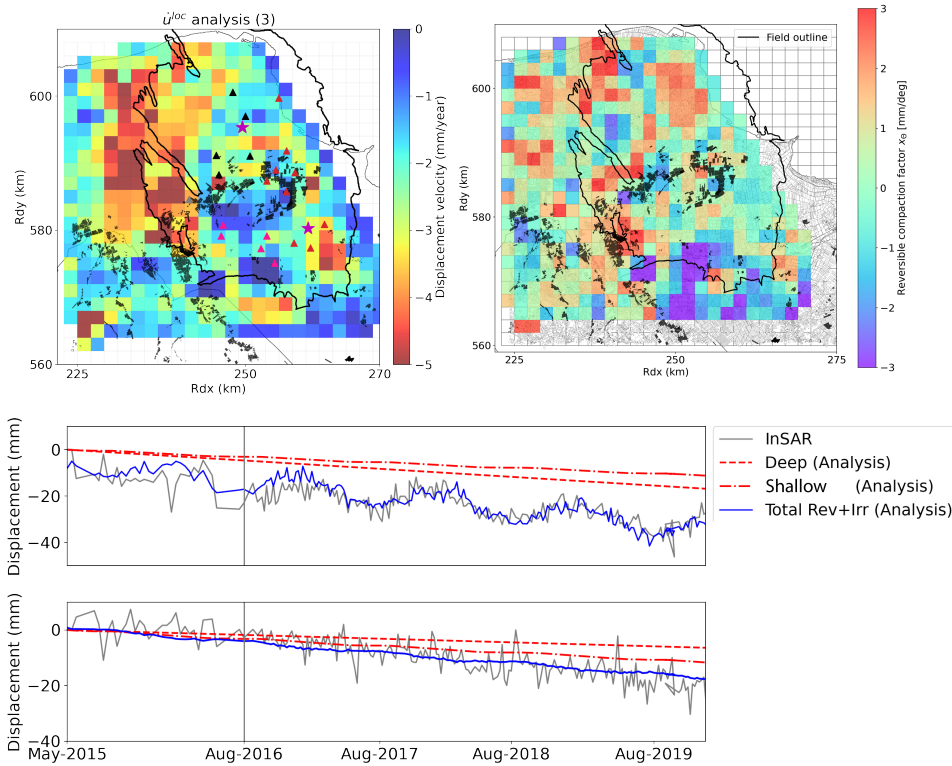


Figure 4.9: (Top left) Map of long-term subsidence analysis with displacement velocities over the period 2015-2020. (Top right) Map of the compaction factor x_θ for the period 2015-2020. (Bottom) Vertical cumulative displacement time series for the data assimilation analysis and the subsidence forecast are compared with the InSAR time series (grey time series), which shows the fit of the forecast to the data after the assimilation step (vertical grey line). Black-shaded areas in the maps indicate parcels in peat soils.

subsidence forecast. A soil composed of clay can have seasonal swelling, whereas there is no or little seasonal variation in a soil composed of settled sand. For these two locations, the data assimilation estimate and the subsidence forecast are compared to the vertical cumulative displacement of the InSAR time series in Fig. 4.9 bottom panel.

After the first assimilation step in 2016, the data assimilation analysis for the vertical cumulative displacement shows a better fit to the InSAR time series in Fig. 4.9 compared to the vertical displacement of the data assimilation analysis with the SPAMS model in Fig. 4.7. The map of displacement velocity attributed to the long-term shallow-driven subsidence in Fig. 4.9 shows vertical displacement velocity in the west part of the Groningen gas field, similarly to that in Fig. 4.7, and with a similar order of magnitude.

To interpret the map of displacement velocity in Fig. 4.9, we verify if the production clusters, with location illustrated in Fig. 4.8 could cause the subsidence estimated as long-term shallow-driven subsidence. The comparison of the location of the production

clusters with the map displacement velocity of shallow-driven subsidence does not show a correlation that could suggest that gas extraction causes the subsidence seen in Fig. 4.9. We also verify if the error in the InSAR estimates propagates in this long-term shallow-driven subsidence (Fig. 4.9). The map of the RMSE in the InSAR time series in Fig. 4.8, which represents the level of noise in the InSAR time series, shows in red the grid cells over the Groningen region where time series have a high level of noise, due to for example loss of coherence in time of the PS. The comparison of this RMSE with the map displacement velocity of shallow-driven subsidence does not show similarities that could explain the estimated subsidence in the western part of the Groningen region.

To further interpret the origin of the estimated long-term shallow-driven subsidence, the map of the so-called "reversible compaction factor" x_θ , as estimated by the data assimilation in Fig. 4.9 indicates if the vertical displacement of the subsidence forecast anti-correlates with atmospheric temperature, meaning uplift in winter and subsidence in summer, as observed in the InSAR time series of cumulative displacement in Fig. 4.9. In the case of anti-correlation, x_θ has a positive value. Areas where x_θ was estimated positive with data assimilation are illustrated with red color in Fig. 4.9 (top right map), showing that in the north, many locations have a seasonal variation that could be attributed to shallow processes. Still in Fig. 4.9 (top right map), purple areas are where the subsidence forecast correlates with atmospheric temperature, meaning uplift in summer and subsidence in winter. The locations correlating with temperature are more frequent in the south, which is expected with infrastructure founded on settled sand layers. Thus, the observed displacements are due to the thermal expansion of the building materials. Many locations do not show seasonal variation ($x_\theta \sim 0$). A comparison of the map of x_θ with the RMSE of the vertical displacement as estimated from InSAR time series (Fig. 4.8) suggests that x_θ is not biased by measurement errors.

Table 4.1: Data assimilation compaction analysis for the reservoir with InSAR displacement estimates relative to 2015.

	2016	2017	2018	2019
ζ with SPAMS (m/year)	-0.010	-0.0075	-0.016	-0.017
ζ with $u^T(\mathbf{x}, T(t))$ (m/year)	-0.0085	-0.0099	-0.010	-0.014

4.7. DISCUSSION

In this chapter, I use a particle filter approach to investigate subsidence-driving mechanisms in the Groningen Region. To do this, I assimilate the InSAR time series of cumulative displacement and displacement velocities from InSAR estimates. Our particle filter implementation effectively assimilates the InSAR time series with approximately 1000 PS spatially distributed over the Groningen region.

Synthetic experiments suggest that we can separate subsidence regimes in a conceptual subsidence model with only two subsidence-driving mechanisms: one deep subsidence driver and one shallow driver. Clay compaction and peat oxidation are likely to cause shallow subsidence in the Groningen region, similar to the subsidence observed in many other areas in the Netherlands that encounter subsidence in similar soil types

(Conroy et al., 2022; Koster et al., 2018; van Asselen et al., 2018). These processes exhibit short-scale and periodic behavior related to external factors such as the weather.

Tests of deep- and shallow-driven subsidence separation show the importance of a physics-based model to represent the driving mechanisms in the shallow subsurface. The main difficulty in the tests presented in this chapter is separating the deep-driven subsidence from the long-term shallow-driven subsidence because the resulting estimates of the subsidence contributions may not be unique. For example, when using the SPAMS model, the data assimilation estimation of the long-term shallow-driven subsidence appears to counterbalance the deep-driven subsidence estimates. Consequently, the estimate of the model parameters may be inaccurate, resulting in the seasonal variation in the vertical displacement of the subsidence forecast that may not fit the variation in the InSAR time series of cumulative displacement.

As an extension of the data assimilation test with the SPAMS model, I tested a simplified test using meteorological data on atmospheric temperature. Using daily temperature averages for the country of the Netherlands to model shallow-driven subsidence in conjunction with a compacting reservoir model to model deep-driven subsidence, I obtain better results in subsidence forecasts. This provides an approach that may give insights into identifying subsidence-driving mechanisms.

To improve subsidence forecasts, a refined model should include subsidence-driving mechanisms representing the large-scale subsidence signal from the deep subsurface and local shallow- and deep-driven subsidence, which can vary given season and production. As improvement in the reservoir model, heterogeneity in the reservoir compaction field, reservoir compartments, and geometry could be modeled. Physics-based shallow-driven subsidence should be considered to model shallow drivers of subsidence, and correlation of the vertical displacement with daily atmospheric temperature could be a good start since soil water content also depends on evapotranspiration and atmospheric temperature. Such a model would need to be calibrated with observations of the compaction in the shallow layers, for example, from extensometers. A combined physics-based and data-driven approach could then better represent the shallow drivers of subsidence than a purely data-driven approach from the SPAMS model used in this study. A focus for a shallow-subsurface model would be to use a dynamical model, which means setting the initial conditions and computing time evolution of the model instead of using a data-driven model where data are used as input at every time step.

4.8. CONCLUSIONS AND RECOMMENDATIONS

The InSAR technique provides estimates of subsidence that can be used for subsidence monitoring. It has the advantage of dense spatial coverage and high resolution over time. However, from the InSAR estimates alone, we can not attribute an origin to the observed subsidence. The data assimilation methodology proposed in this chapter provides an approach for identifying subsidence-driving mechanisms and forecasting long-term subsidence.

Applying data assimilation, we forecast a seasonal variation in subsidence by correlating

the variation of daily atmospheric temperature data with subsidence. In addition to the long-term subsidence trends that could be attributed to reservoir compaction or shallow long-term subsidence, we identify subsidence signals with seasonal patterns that could be attributed to shallow driving mechanisms.

Overall, this chapter tests applying the particle filter to the Groningen gas field with deep- and shallow subsidence-driving mechanisms and provides insights into the use of InSAR time series of cumulative displacement and InSAR displacement velocities to identify subsidence-driving mechanisms. The approach shows promising results in separating deep- and shallow-driven subsidence components in synthetic tests. However, the application with actual data shows that the method would require a better description of the modeled subsidence mechanism to perform efficiently. A possible way to improve the approach is to use a refined model, including, for example, prior information on soil geology, water management, precipitation data and temperature, variations, and possible secondary effects of the deep-driven subsidence on the shallow-driven subsidence.

5

CONCLUSIONS AND RECOMMENDATIONS

*Physicists like to think that all you have to do is say, these are the conditions,
now what happens next?*

Richard P. Feynman

5.1. CONCLUSIONS

In this thesis, I proposed to apply a particular data assimilation method, the importance sampling, to estimate subsidence and its causes based on a physical description of its driving mechanisms for the Groningen region and formulated the research question

How can importance sampling be efficiently applied for subsidence estimation in the Groningen region to identify its driving mechanisms better?

To answer this question, I explored three sub-questions:

1. How can we apply importance sampling in a subsidence estimation problem of the complexity of the Groningen gas field?
2. How can we effectively use InSAR data for subsidence estimation with data assimilation?
3. How can data assimilation identify subsidence-driving mechanisms given the spatial and temporal scales of geodetic displacement estimates?

I answered those questions by focusing on the data-assimilation methodology and its implementation.

Starting with a basic implementation of importance sampling, I combined geophysical modeling with geodetic estimates to estimate subsidence based on better estimating the underlying processes causing subsidence in the Groningen region. The displacement signal of the subsidence process above the Groningen gas field is an accumulated response of processes taking place in all subsurface layers at different locations. This makes the subsidence signal spatially correlated. This spatial correlation and the large number of observations in geodetic datasets cause weight collapse in the posterior PDF estimated with importance sampling: the posterior variance is smaller than the variance expected from Bayes' theorem.

The main objective of this study was to develop an efficient importance sampling strategy that avoids weight collapse while assimilating geodetic estimates and accounts for deep— and shallow subsidence-driving mechanisms. Using the so-called *optimal proposal importance sampling*, I demonstrated the use of a data-assimilation workflow that assimilates both averaged velocities and cumulative displacements from leveling and InSAR datasets in the Groningen region. This workflow can eventually be used to forecast subsidence. The following presents the conclusions for each chapter of his thesis, answering the research question and providing recommendations and insights for future research.

5

In Chapter 2, I introduced the method of importance sampling. In particular, I investigated how this method's performance for a given ensemble size (i.e., the number of model realizations) varies as a function of the spatial correlation in the displacement field. With synthetic tests, I showed that a subsidence model with 50 independent state variables requires a minimum ensemble size of 10^{13} to avoid weight collapse. Based on information theory, I demonstrated that information loss occurs in the posterior distribution because of the spatial correlations in the subsidence field, which makes it non-i.i.d. I derived an empirical relationship to estimate the minimal ensemble size required for efficient subsidence estimation with importance sampling.

In Chapter 3, I implemented importance sampling with the *optimal proposal* for a realistic subsidence estimation above the Groningen field. I showed that it is possible to estimate subsidence by assimilating averaged velocities from leveling and InSAR estimates: a leveling datasets (with an observation space dimension of $N_y = 500$) requires less than $N_e = 10^4$ ensemble members. An InSAR dataset of 1000 observation points requires 10^3 ensemble members. Surprisingly, the required ensemble size for the assimilation of InSAR estimates is lower than for the assimilation of a leveling dataset because of the difference in error characteristics between the two geodetic techniques. The maximal posterior weight of 0.4 in the assimilation of the InSAR dataset with an ensemble size of 1000 and 1032 PS underpins my conclusion that the optimal proposal avoids weight collapse in our application.

In Chapter 4, I further refined the optimal proposal importance sampling to assimilate InSAR time series of cumulative displacement instead of averaged velocity. The fact that several mechanisms contribute to the subsidence signal in the InSAR cumulative displacement increases the complexity of unambiguously identifying the subsidence-driving mechanisms with data assimilation because of the problem's non-uniqueness. To investigate how to estimate both the deep and shallow drivers of

subsidence, I combined models of compacting reservoirs with models of the shallow drivers of subsidence in data assimilation.

In addition to the compacting reservoir model for the deep-driven subsidence, I used two different models for the shallow subsurface compaction. The first shallow subsurface model (Conroy et al., 2023) provides a prediction of soil motion computed from meteorological data of precipitation and evapotranspiration; the second shallow subsurface model uses only the atmospheric temperature as input. The data assimilation estimate of shallow-driven subsidence using the second model, with only the atmospheric temperature as input, showed a better fit to the InSAR time series and more accurate subsidence forecasts than in the first shallow subsurface model.

By applying the particle filter using synthetically generated InSAR estimates, I showed that the data assimilation framework can accurately separate deep- and shallow-driven subsidence using the difference in variability of the spatial scales of the driving mechanisms. The displacement caused by shallow-driving mechanisms has small spatial correlation scales, while the compacting reservoir has large correlation scales. The data assimilation estimates the reservoir- and shallow-layer compaction and, based on that, the subsidence contribution of both driving mechanisms.

The assimilation of actual InSAR time series did not unambiguously identify the subsidence-driving mechanisms because of the non-uniqueness in representing subsidence processes in models. This requires further research.

5.2. RECOMMENDATIONS FOR FUTURE RESEARCH

5.2.1. ON THE USE OF IMPORTANCE SAMPLING FOR THE GRONINGEN REGION

In this thesis, I implemented importance sampling to estimate subsidence over the Groningen gas field. The optimal proposal particle filter (Doucet et al., 2000; Snyder, 2011; Snyder et al., 2015; van Leeuwen et al., 2015) showed good applicability to the estimation problem of subsidence in the Groningen region. Still, in this application, I reduced the number of observation points to limit the ensemble size and, thereby, the computational cost. To avoid reducing the number of observation points, the importance sampling method with the optimal proposal could be further enhanced by including localization, specifically for the spatially uncorrelated shallow-driven subsidence.

5.2.2. ON ALTERNATIVE DATA ASSIMILATION METHODS

In essence, the particle filter directly applies Bayes' theorem, which estimates the state vector and its uncertainty given observations. Thus, the particle filter is a straightforward approach to *exactly* estimate the target PDF. The advantage of the particle filter is its ability to estimate nonlinear processes. In this study, I did not model nonlinear subsidence-driving mechanisms; however, deep- and shallow-driven subsidence can be nonlinear. Since most subsidence models for the Groningen region are linear, data-assimilation methods such as (iterative) ensemble smoothers or the EnKF would be

more efficient than the particle filter in assimilating large geodetic datasets. A smoother method that estimates the initial conditions, such as 4DVar or specific implementations of ensemble smoothers, relates the evolution of a process over a data-assimilation window to the state at the start of the assimilation window. Since InSAR estimates provide the displacement relative to a moment in time, smoother techniques may be especially suitable.

5.2.3. ON THE USE OF InSAR IN DATA ASSIMILATION

InSAR data are processed from the radar signal to the displacement estimate, which implies various sources of errors. For example, the InSAR processing from phase difference to displacement introduces errors, and the atmospheric corrections will affect the InSAR estimate.

The data assimilation of InSAR data would benefit from better knowledge of the source of the error in the InSAR estimates, for example, the temporal coherence of a PS and the error in the InSAR processing. Without quantitative information on individual PS errors, a data assimilation practitioner cannot derive the exact observation error matrix (covariance matrix or observation operator), mainly because InSAR estimates (e.g., cumulative displacements or averaged velocities) have an error varying in space and time. To derive an error covariance matrix, we could attribute an error to each PS, given the so-called stochastic model, which is an error model used in the InSAR processing.

Moreover, InSAR estimates are sensitive to the surface on which the satellite signal reflects (e.g., a corner reflection on a building can be used to represent a different mechanism than a reflection on the ground), as explained in Section 1.2 and Ketelaar, 2009. Contextualizing information about each PS (e.g., PS elevation, soil type) could help define the observation operator in data assimilation.

5.2.4. ON MODEL REFINEMENT

In the case of subsidence in Groningen, the contribution of multiple subsidence-driving mechanisms complicates the data assimilation because it can lead to non-uniqueness of the estimation problem; for example, the shallow-driven subsidence could erroneously be attributed to the deep-driven subsidence. Without knowing what the InSAR estimates represent, we can misinterpret the mismatch between the model and the InSAR estimates.

Chapter 4 showed that the shallow subsurface contributes to the Groningen region's subsidence. The shallow subsurface models tested in this thesis do not represent the complete physics of the shallow-driving mechanisms. For example, a too-simplified model of the shallow subsurface, with compaction in the north and no compaction in the south, does not provide a realistic representation of the shallow-driven subsidence. Choosing a more realistic model for the shallow subsurface could result in a more realistic estimate of the shallow-driven subsidence and, hence, the total subsidence. For example, we could use the model of Koster et al., 2018 to obtain a more realistic model representation of the shallow subsurface.

Different drivers can give the same subsidence field; in other words, solutions to this estimation problem may not be unique. Synthetic experiments in this thesis suggested the ability of data assimilation to identify the subsidence-driving mechanisms. However, realistic experiments were not conclusive because models and data do not represent exactly the same processes, and different subsurface processes may give similar subsidence signals. A possible way to constrain this non-unique problem is by providing more prior information (e.g., a more detailed description of physical processes) or additional observations (e.g., from extensometers that measure soil compaction as a function of depth) at strategic locations.

5.3. FINAL THOUGHTS

WE know by now that using subsidence observations above the Groningen gas field to identify and quantify all processes contributing to subsidence is a complex problem. In this thesis, data assimilation has been studied to help understand the driving mechanisms better and provide long-term subsidence forecasts. “Physicists like to think that all you have to do is say, these are the conditions, now what happens next?” says Richard P. Feynman. “*What happens next*” in the estimation of subsidence-driving mechanisms in the Groningen region is uncertain, and the combined effort of geodetic monitoring with physical modeling through data assimilation offers a methodology to assemble available knowledge from observations and models to reduce this uncertainty. In this manner, data assimilation reduces the error in estimating the *hidden* physical processes by combining models and observations, which are difficult, if not impossible, to estimate from observations or modeling alone.

A

SUPPLEMENT INFORMATION FOR THE POSTERIOR ENTROPY CALCULATION

This appendix provides the expression of the conditional entropy used in Chapter 2 to compute the posterior entropy.

Starting from the definition of the entropy, H of a random variable x as a function of the probability $p(x)$

$$H(x) = -\sum_i p(x_i) \log(p(x_i)), \quad (\text{A.1})$$

where $0 < p(x), 1$. We define the posterior entropy in the particle filter, which is the conditional entropy $H(x|y)$

$$H(x|y) = -\int p(x|y)p(y) \log(p(x|y)) dx dy. \quad (\text{A.2})$$

The posterior probability can be expressed as a weighted Dirac sum

$$p(x|y) = \sum_{i=1}^{N_e} w_i \delta(x - x_i), \quad (\text{A.3})$$

with the particle weight

$$w_i = \frac{p(y|x_i)}{\sum_{i=1}^{N_e} p(y|x_i)}. \quad (\text{A.4})$$

We can then express the posterior entropy as a function of the likelihood probability $p(y|x)$ using that $\int f(x)\delta(x - x_i) dx = f(x_i)$

$$H(x|y) = -\int \left[\sum_{i=1}^{N_e} w_i \delta(x - x_i) \right] p(y) \log \left[\sum_{i=1}^{N_e} w_i \delta(x - x_i) \right] dx dy \quad (\text{A.5})$$

$$= -\sum_{i=1}^{N_e} w_i p(y) \log \left[\frac{p(y|x_i)p(x_i)}{p(y)} \right] \quad (\text{A.6})$$

$$= -\sum_{i=1}^{N_e} w_i p(y) \log[p(y|x_i)] + \sum_{i=1}^{N_e} w_i p(y) \log[p(y)] - \sum_{i=1}^{N_e} w_i \log[p(x_i)]. \quad (\text{A.7})$$

Using the expression of $p(y)$ and that the likelihood is normalized to one:

$$p(y) = \int p(x, y) dx = \int p(y|x)p(x) dx = \frac{1}{N_e} \sum_{i=1}^{N_e} p(y|x_i) = \frac{1}{N_e}, \quad (\text{A.8})$$

We obtain

$$H(x|y) = -\sum_{i=1}^{N_e} w_i \frac{1}{N_e} + \sum_{i=1}^{N_e} w_i \frac{1}{N_e} \log \left[\frac{1}{N_e} \right] - \sum_{i=1}^{N_e} w_i \log(p(x_i)) \quad (\text{A.9})$$

$$H(x|y) = -\sum_{i=1}^{N_e} \frac{w_i}{N_e} \log(w_i) - \sum_{i=1}^{N_e} \frac{w_i}{N_e} \log(N_e) - \sum_{i=1}^{N_e} w_i \log(p(x_i)). \quad (\text{A.10})$$

This expression can be implemented to evaluate the posterior entropy in the particle filter as in chapter 2, where the entropy was used to evaluate posterior weight collapse and information loss in the posterior distribution.

B

SENSITIVITY TESTS FOR THE ENTROPY ESTIMATION

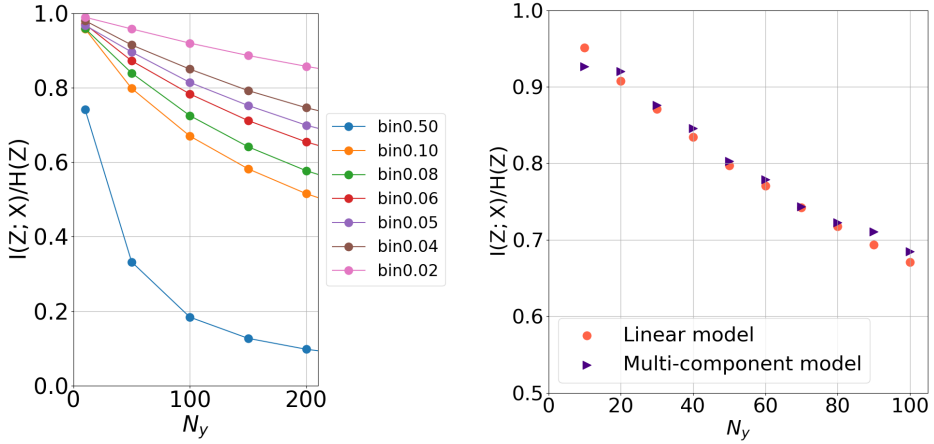


Figure B.1: (left) Convergence test of the information in the model as the function of the number of observations showing the convergence rate at difference bin width used in the empirical estimation of the mutual information. (Right) Convergence test of the information in the model as a function of the number of observations, N_y , or nuclei of strain, N_x since $N_y = N_x$. The linear model (i.e., one-component model) and the multi-component model are tested and show the exact same convergence rate.

Entropy and mutual information values are derived using histogram estimation. Consequently, entropy and mutual information are sensitive to a chosen histogram binwidth and the sample size. In the example in Chapter 2, we have a sample of observations or model parameters of dimension N_y and N_x , respectively. The result of the histogram estimation method is considered reproducible when the histogram statistically converges to the same density at each new experiment. In Chapter 2, testing the sensitivity of the entropy and mutual information values to N_y (or N_x) and the binwidth is important to not misinterpret weight collapse results.

Figure B.1 (left) shows the sensitivity test for the mutual information in the model as a function of the number of observations (or the number of model parameters): in this example, $N_y = N_x$. Sensitivity results show that the mutual information converges faster at a binwidth of 0.5. Convergence could be improved with a sample size larger than $N_y = N_x = 200$. However, to test the metric of entropy and mutual information in importance sampling, it is more practical in computation to use a sample size smaller than 100.

Then, in Fig. B.1 (right), we test the mutual information as a function of N_y for the linear (i.e., one-component) model and the multi-component model to ensure that there is no biased because of the sensitivity to the sample size. The test is performed on the mutual information before assimilation, so there is no weight collapse. We can see that we obtain the same mutual information in the two models at a given sample size. The same test was repeated several times and showed no deviation from Fig. B.1 (Right). For this reason, we chose in Chap. 2 the sample size $N_x = N_y = 50$, which is valid if all posterior entropy and mutual information quantities are computed at a similar sample size.

C

SUPPLEMENT ON THE RESERVOIR MODEL GEOMETRY

In Chapter 2, we tested the mathematical theory of Snyder et al., 2008 and included a spatial dimension to the data-assimilation problem. Indeed, model states and observations do not have spatial coordinates in the mathematical concept of the asymptotic theory (Bengtsson et al., 2008; Snyder et al., 2008). Then, we created a conceptual subsidence model based on the nuclei of strain approach. Figure C.1 shows the model geometry with the nuclei of strain distributed on a regular grid. The vertical displacement is calculated at observation points located at the vertical of the nuclei at the Earth's surface. The longitude and latitude of the area of interest remain unchanged in the three tests (Fig. C.1 top, center, and bottom), but the number of nuclei of strain increases, creating a varying spatial correlation in the modeled subsidence signal. The purpose of this model is to start with an example similar to the theoretical case, which does not include spatial coordinates, and gradually increase the model complexity (Chap. 3 and 4).

In Chapter 3 and 4, we used the nuclei of strain approach and modeled the reservoir as a disk. This geometry is a simplification that provides an approximation of the bowl-shaped subsidence. Figure C.2 (top) shows a model geometry with more than 900 nuclei of strain (black dots) creating a disk. Using a regular grid (gray dots) and the center of the gas field (red dot), all points within a certain radius from the field center are selected to define the location of the nuclei of strain. The resulting vertical displacement (Fig. C.2 bottom) provides a smooth bowl-shaped subsidence. In Figure C.2 (bottom), the vertical displacement is computed at the vertical of the nuclei of strain, but for the purpose of data assimilation, the modeled subsidence is, in this thesis, mainly computed as observation locations. Whereas this model geometry is highly simplistic, the reservoir compaction at the nuclei of strain position can also be estimated independently for each nuclei using data assimilation. For example, in Chap 4, Fig. 4.6, the reservoir compaction was estimated based on a regular square grid of nuclei of strain, similar to the gray dots in Fig. C.2. After the assimilation of leveling data, the nuclei of strain location where it was unlikely that compaction would occur were set to zero compaction, and a more realistic reservoir shape was estimated.

A finite element model was also tested during this thesis but not included in this manuscript (Fig. C.3). This model is still being developed at Utrecht University and could be used in future applications with data assimilation.

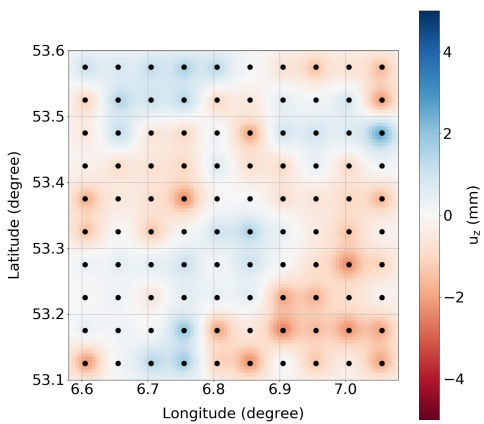
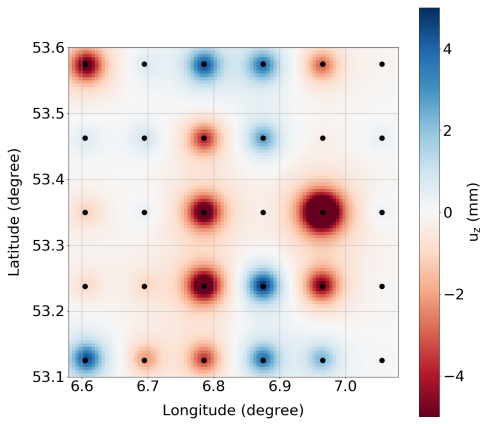
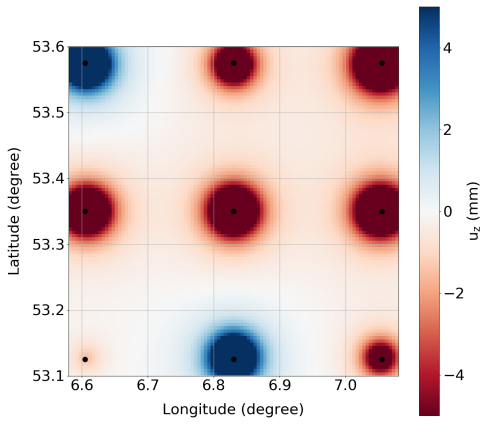


Figure C.1: Conceptual subsidence model with nuclei of strain spatially distributed on a regular grid (black dots). Nuclei of strain have a random compaction coefficient, causing a proportional compaction source and subsidence (vertical displacement u_z) at the surface.

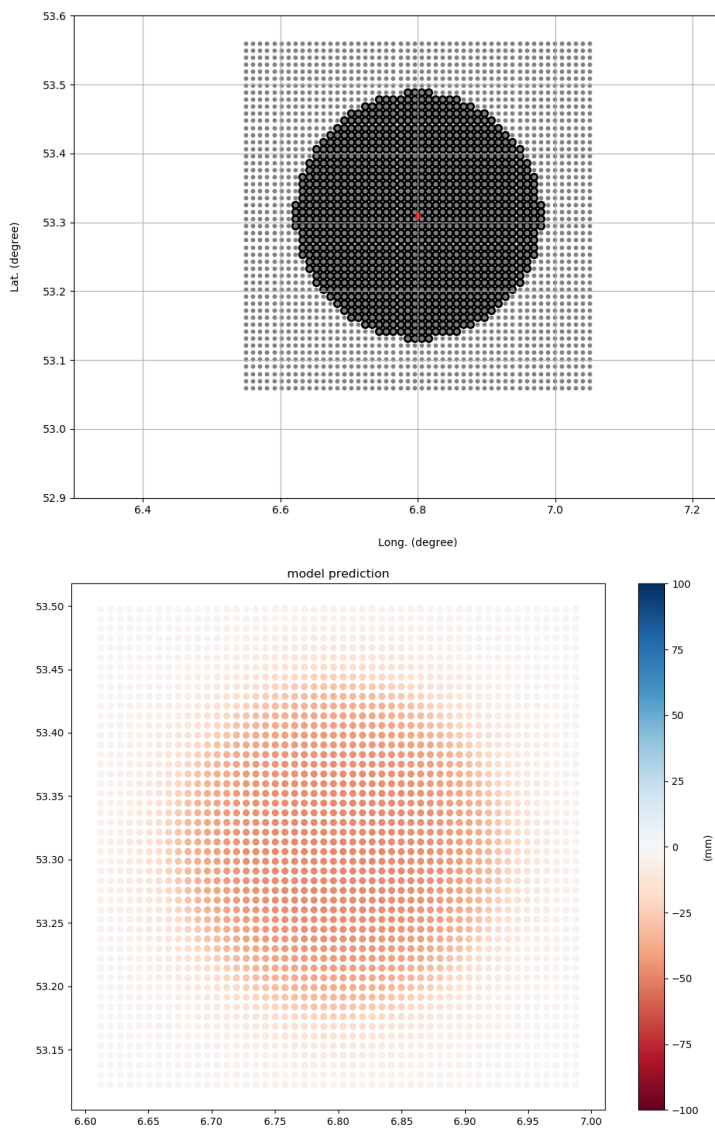


Figure C.2: (Top) Model geometry with the spatial distribution of the nuclei of strain, selected on a regular grid (light gray) to create a disk-shaped reservoir (black dots). (Bottom) The subsidence is modeled from a disk-shaped reservoir composed of nuclei of strain. The vertical displacement is calculated at synthetic observation points, located at the vertical of the nuclei of strain, and shows a bowl shape subsidence.

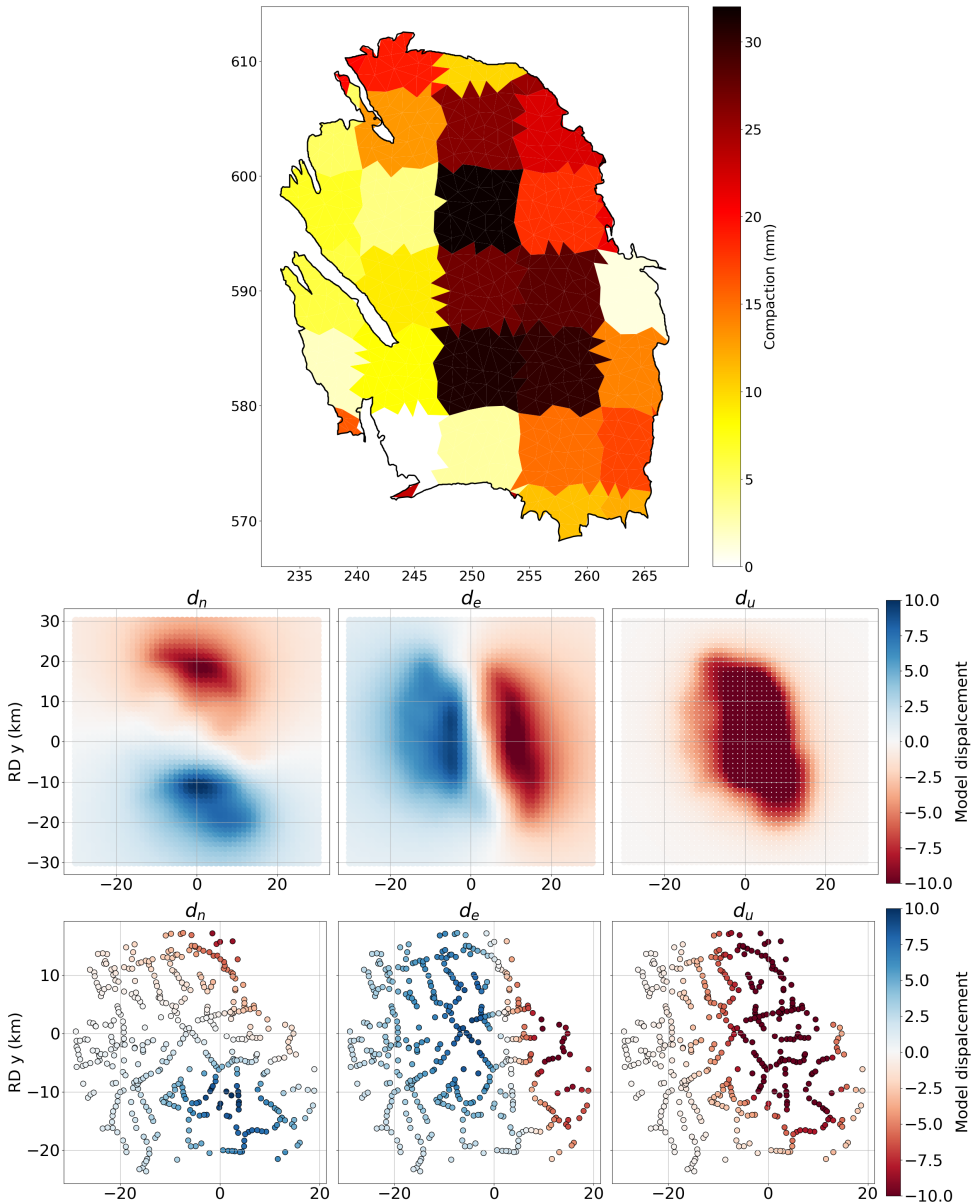


Figure C.3: Model geometry for a finite element model showing a “checkerboard” test with square compartments, to which random compactions are attributed into the boundary of the gas field. (Bottom) The resulting subsidence is calculated in the North, East, and vertical directions over a grid resolution of 1 km x 1 km over the area of interest (smooth subsidence signal) and at observation locations (dots).

D

SUPPLEMENT ON THE INSAR DATASET REDUCTION

Reducing the number of observation locations was important in this thesis to test importance sampling the identification of shallow-driven subsidence. PS were averaged per parcel to obtain a subsidence signal without filtering information about the shallow-driven subsidence (fig. D.1, gray background). The displacement time series of all PS is average in a radius of 250 m around each parcel centroid. An additional data reduction was necessary to test importance sampling with varying numbers of PS. To create InSAR datasets of different sizes (i.e., number of observation locations), the area is gridded to obtain a homogeneous spatial distribution of “averaged PS” (i.e., avoiding high density around infrastructures), and one observation location was at least selected in each grid. The grid size varies as a function of the necessary number of observation points.

D

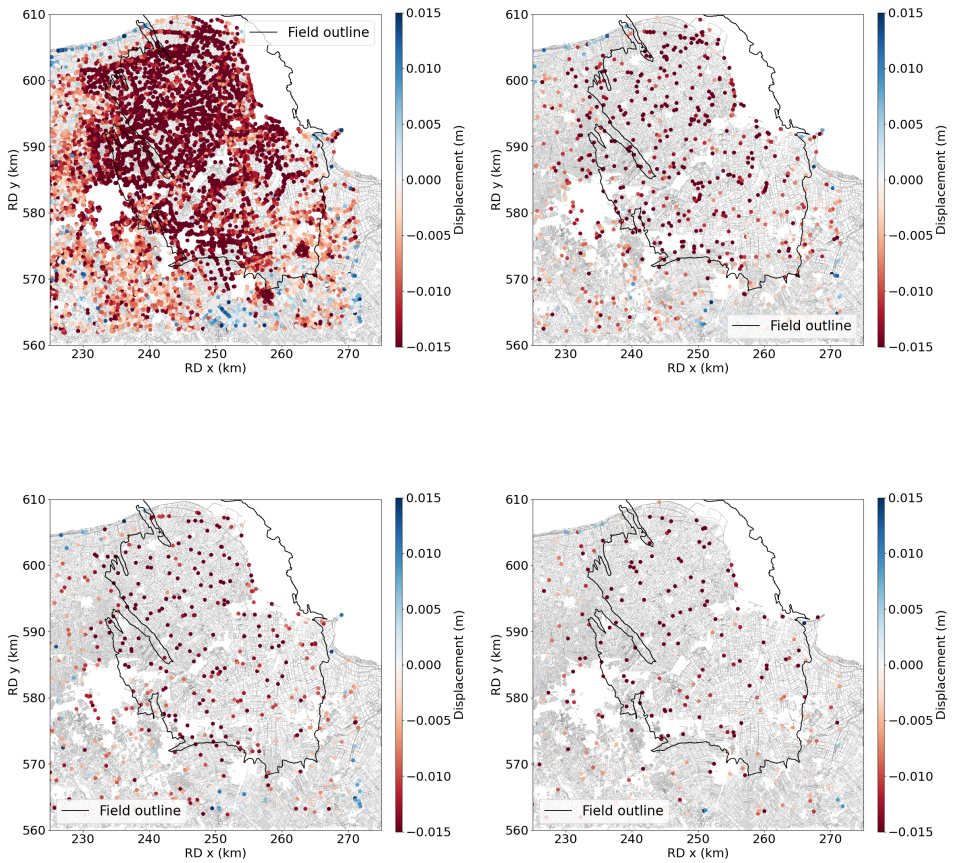


Figure D.1: PS-InSAR averaged per parcel showing (top left) the InSAR dataset after the parcel average (average of all InSAR time series within 250m radius to a parcel centroid) and several examples of reduced datasets created to be assimilated.

NOTATION

ΔP	Reservoir pressure variation
$\eta(t)$	stochastic term representing the shallow compaction
β	Stochastic part of the system evolution
ϵ	Observation error
σ	Stress
\mathbf{e}	Model error
\mathbf{x}	State vector
\mathbf{x}^{truth}	Synthetic true state vector
\mathbf{y}	Observation vector
\mathcal{E}_{DA}	Data assimilation efficiency
\mathcal{H}	Observation operator
\mathcal{M}	Model operator
μ	Statistical mean
ν	Poisson ratio
Φ	Phase difference
σ	Standard deviation
Σ_e	Covariance matrix of the model error
Σ_c	Covariance matrix of the observation error
$\tilde{\mathbf{y}}$	Synthetic observation vector
ζ	Reservoir compaction
C_m	Compaction coefficient
d_{ENU}	Displacement vector in Cartesian coordinates (E,N,U)
d_{LoS}	Displacement vector in Line of Sight

$E(t)$	Evapotranspiration from KNMI data
H	Entropy
I	Mutual information
I_d	Identity
I_{diff}	Differential mutual information
$N(t)$	Precipitation from KNMI data (Neerslag)
N_e	Ensemble size
N_x	State space dimension
N_y	Observation space dimension
P	Reservoir pressure
T	Temperature
V	Negative log-likelihood
w	Particle weight
w_{max}	Maximal posterior weight

ACRONYMS

- i.i.d.** independent and identically distributed. 34, 56, 100
- InSAR** Interferometric Synthetic Aperture Radar. xi, 3, 8, 80
- KNMI** Koninklijk Nederlands Meteorologisch Instituut. 20, 21
- LoS** Line-of-Sight. 10
- NAM** Nederlandse Aardolie Maatschappij. 3, 63
- NAP** Normaal Amsterdams Peil (Normal Amsterdam level). 6
- PDF** probability density function. xi, 24
- PFOP** particle filter with optimal proposal. 63
- PS** Point Scatterer. 9, 10, 12, 20, 21, 55, 68, 79, 80
- PSs** Point Scatterers. xii
- SPF** standard particle filter. 63

GLOSSARY

Bayes' theorem provides the probability of a random variable given its observation likelihood. 25, 57, 100

dynamical refers to a time-varying system which can be described with a dynamical model where model states vary in time.. 55

ensemble members is are the model realizations generated in a Monte Carlo sample. 100

ensemble size is the number of model realizations in a Monte Carlo-based method. 28, 100

Holocene is the geological era from 0.0117 Ma to nowadays. 5

importance sampling is a Monte Carlo-based method to estimate a target probability density function by sampling random variables from a particular PDF xi

information theory is a mathematical theory based on statistical mathematics to quantify information, initially in information systems. 100

maximal posterior weight is the weight of the posterior distribution (PDF obtained after applying Bayes' theorem), which has the largest probability. It is used in this thesis as criteria to verify weight collapse in the posterior PDF. 100

peat oxidation is an irreversible decomposition process of peat soils occurring after exposition to oxygen. 7

Pleistocene is a geological era from 2.58 Ma to 0.0117 Ma ago. 5

posterior distribution see posterior PDE 100

quasi-static refers to a system where the model states vary slowly in time and can be approximated as time-independent. Then, no dynamical model is involved in modeling the system.. 31

spatial correlation is the correlation of a certain quantity at one location in space with this quantity at other locations around this place. 100

static refers to a time-independent system where the model states do not vary.. 33

stochastic model is a mathematical model used in InSAR processing to predict statistical properties of the InSAR estimates, such as the variance. 102

transition density is a conditional PDF used to forward in time the prior ensemble, it usually represents the stochastic part of the model, *M*. 57

weight collapse is when the weights of a probability mass function (i.e., discrete probability density function) are mostly close to a value of zero except one weight with a value converging to one. 100

BIBLIOGRAPHY

- Ades, M., & van Leeuwen, P. J. (2015). The equivalent-weights particle filter in a high-dimensional system. *Quarterly Journal of the Royal Meteorological Society*, *141*(687), 484–503.
- Ades, M., & van Leeuwen, P. J. (2013). An exploration of the equivalent weights particle filter. *Quarterly Journal of the Royal Meteorological Society*, *139*(672), 820–840. <https://doi.org/10.1002/qj.1995>
- Alvenäs, G., & Jansson, P.-E. (1997). Model for evaporation, moisture and temperature of bare soil: Calibration and sensitivity analysis. *Agricultural and Forest Meteorology*, *88*(1-4), 47–56.
- Asch, M., Bocquet, M., & Nodet, M. (2016). *Data assimilation: Methods, algorithms, and applications*. SIAM.
- Auriac, A., Sigmundsson, F., Hooper, A., Spaans, K., Björnsson, H., Pálsson, F., Pinel, V., & Feigl, K. (2014). InSAR observations and models of crustal deformation due to a glacial surge in iceland. *Geophysical Journal International*, *198*(3), 1329–1341.
- Bain, A., & Crisan, D. (2009). *Fundamentals of stochastic filtering* (Vol. 3). Springer.
- Bengtsson, T., Bickel, P., Li, B., et al. (2008). Curse-of-dimensionality revisited: Collapse of the particle filter in very large scale systems. *Probability and statistics: Essays in honor of David A. Freedman*, *2*, 316–334. <https://doi.org/10.1214/193940307000000518>
- Beskos, A., Crisan, D., Jasra, A., et al. (2014). On the stability of sequential monte carlo methods in high dimensions. *Annals of Applied Probability*, *24*(4), 1396–1445. <https://doi.org/10.1214/13-AAP951>
- Beskos, A., Crisan, D., Jasra, A., Kamatani, K., & Zhou, Y. (2017). A stable particle filter for a class of high-dimensional state-space models. *Advances in Applied Probability*, *49*(1), 24–48. <https://doi.org/10.1017/apr.2016.77>
- Bierman, S., Kraaijeveld, F., & Bourne, S. (2015). Regularised direct inversion to compaction in the groningen reservoir using measurements from optical leveling campaigns. *NAM, SR15*, 11194.
- Bourne, S., Oates, S., van Elk, J., & Doornhof, D. (2014). A seismological model for earthquakes induced by fluid extraction from a subsurface reservoir. *Journal of Geophysical Research: Solid Earth*, *119*(12), 8991–9015.
- Brewer, B. J. (2017). Computing entropies with nested sampling. *Entropy*, *19*(8), 422. <https://doi.org/10.3390/e19080422>
- Brouwer, W. S., & Hanssen, R. F. (2023). A treatise on InSAR geometry and 3D displacement estimation. *IEEE transactions on geoscience and remote sensing*, *61*, 1–11. <https://doi.org/10.1109/TGRS.2023.3322595>
- Bruhat, G., & Kastler, A. (1965). *Optique: Cours de physique générale*.

- Bruna, M. F. (2020). *Analyzing subsidence in the Netherlands with attribute-enriched InSAR data* (Master's thesis). Delft University of Technology.
- Candela, T., Chitu, A., Peters, E., Pluymaekers, M., Hegen, D., Koster, K., & Fokker, P. (2021). A data assimilation framework to constrain the driving processes of anthropogenically induced subsidence.
- Candela, T., Osinga, S., Ampuero, J.-P., Wassing, B., Pluymaekers, M., Fokker, P., van Wees, J.-D., de Waal, H. A., & Muntendam-Bos, A. G. (2019). Depletion-induced seismicity at the groningen gas field: Coulomb rate-and-state models including differential compaction effect. *Journal of Geophysical Research: Solid Earth*, *124*(7), 7081–7104. <https://doi.org/10.1029/2018JB016670>
- Carrassi, A., Bocquet, M., Demaeyer, J., Grudzien, C., Raanes, P., & Vannitsem, S. (2022). Data assimilation for chaotic dynamics. *Data Assimilation for Atmospheric, Oceanic and Hydrologic Applications (Vol. IV)*, 1–42.
- CGG. (2022). Insar line of sight (los) explained [Accessed: 2024-03-25].
- Chang, L., & Hanssen, R. F. (2015). A probabilistic approach for InSAR time-series postprocessing. *IEEE transactions on geoscience and remote sensing*, *54*(1), 421–430.
- Chorin, A. J., & Morzfeld, M. (2013). Conditions for successful data assimilation. *Journal of Geophysical Research: Atmospheres*, *118*(20), 11–522. <https://doi.org/10.1002/2013JD019838>
- Conroy, Heikoop, J., Lathrop, E., Musa, D., Newman, B., Xu, C., McCaully, R., Arendt, C., Salmon, V., Breen, A., et al. (2022). Environmental controls on observed spatial variability of soil pore water geochemistry in small headwater catchments underlain with permafrost. *EGU sphere*, *2022*, 1–29.
- Conroy, van Diepen, S. A., & Hanssen, R. F. (2023). Spams: A new empirical model for soft soil surface displacement based on meteorological input data. *Available at SSRN 4500693*.
- Diab-Montero, H. A., Li, M., van Dinther, Y., & Vossepoel, F. C. (2023). Estimating the occurrence of slow slip events and earthquakes with an ensemble kalman filter. *Geophysical Journal International*, *234*(3), 1701–1721.
- Doucet, A., De Freitas, N., & Gordon, N. (2001). An introduction to sequential monte carlo methods. *Sequential Monte Carlo methods in practice*, 3–14.
- Doucet, A., Godsill, S., & Andrieu, C. (2000). On sequential monte carlo sampling methods for bayesian filtering. *Statistics and computing*, *10*(3), 197–208.
- Du, J., & Olson, J. E. (2001). A poroelastic reservoir model for predicting subsidence and mapping subsurface pressure fronts. *Journal of Petroleum Science and Engineering*, *30*(3-4), 181–197. [https://doi.org/10.1016/S0920-4105\(01\)00131-0](https://doi.org/10.1016/S0920-4105(01)00131-0)
- Emerick, A. A., & Reynolds, A. C. (2013). Ensemble smoother with multiple data assimilation. *Computers & Geosciences*, *55*, 3–15.
- Erkens, G., van der Meulen, M. J., & Middelkoop, H. (2016). Double trouble: Subsidence and co2 respiration due to 1,000 years of dutch coastal peatlands cultivation. *Hydrogeology Journal*, *24*(3), 551.
- Evensen, G., Raanes, P. N., Stordal, A. S., & Hove, J. (2019). Efficient implementation of an iterative ensemble smoother for data assimilation and reservoir history matching. *Frontiers in Applied Mathematics and Statistics*, *5*, 47.

- Evensen, G., & Van Leeuwen, P. J. (2000). An ensemble kalman smoother for nonlinear dynamics. *Monthly Weather Review*, *128*(6), 1852–1867.
- Evensen, G., Vossepoel, F. C., & van Leeuwen, P. J. (2022). Data assimilation fundamentals: A unified formulation of the state and parameter estimation problem. <https://doi.org/10.1007/978-3-030-96709-3>
- Farchi, A., & Bocquet, M. (2018). Comparison of local particle filters and new implementations. *Nonlinear Processes in Geophysics*, *25*(4), 765–807.
- Fjaer, E., Holt, R. M., Horsrud, P., & Raaen, A. M. (2008). *Petroleum related rock mechanics*. Elsevier.
- Fokker, P., Gunnink, J. L., Koster, K., & de Lange, G. (2019). Disentangling and parameterizing shallow sources of subsidence: Application to a reclaimed coastal area, flevoland, the netherlands. *Journal of Geophysical Research: Earth Surface*, *124*(5), 1099–1117.
- Fokker, P., Visser, K., Peters, E., Kunakbayeva, G., & Muntendam-Bos, A. (2012). Inversion of surface subsidence data to quantify reservoir compartmentalization: A field study. *Journal of Petroleum Science and Engineering*, *96*, 10–21. <https://doi.org/10.1016/j.petrol.2012.06.032>
- Fokker, P., Wassing, B., van Leijen, F., Hanssen, R., & Nieuwland, D. (2016). Application of an ensemble smoother with multiple data assimilation to the Bergermeer gas field, using PS-InSAR. *Geomechanics for Energy and the Environment*, *5*, 16–28. <https://doi.org/10.1016/j.gete.2015.11.003>
- Fowler, A., & van Leeuwen, P. (2012). Measures of observation impact in non-gaussian data assimilation. *Tellus A: Dynamic Meteorology and Oceanography*, *64*(1), 17192.
- Fowler, A., & van Leeuwen, P. (2013). Observation impact in data assimilation: The effect of non-Gaussian observation error. *Tellus A: Dynamic Meteorology and Oceanography*, *65*(1), 20035.
- Gazzola, L., Ferronato, M., Frigo, M., Janna, C., Teatini, P., Zoccarato, C., Antonelli, M., Corradi, A., Dacome, M. C., & Mantica, S. (2021). A novel methodological approach for land subsidence prediction through data assimilation techniques. *Computational Geosciences*, *25*(5), 1731–1750. <https://doi.org/10.1007/s10596-021-10062-1>
- Geertsma, J. (1966). Problems of rock mechanics in petroleum production engineering. *1st ISRM Congress*.
- Geertsma, J. (1973). Land subsidence above compacting oil and gas reservoirs. *Journal of petroleum technology*, *25*(06), 734–744. <https://doi.org/10.2118/3730-PA>
- Geertsma, J., & van Opstal. (1973). A numerical technique for predicting subsidence above compacting reservoirs, based on the nucleus of strain concept. *30*, 53–78.
- Gharekhani, M., Nadiri, A. A., Khatibi, R., & Sadeghfam, S. (2021). An investigation into time-variant subsidence potentials using inclusive multiple modeling strategies. *Journal of Environmental Management*, *294*, 112949.
- Gussinklo, H., Haak, H., Quadvlieg, R., Schutjens, P., & Vogelaar, L. (2001). Subsidence, tremors and society. *Netherlands Journal of Geosciences*, *80*(1), 121–136.
- Hanssen, R. F. (2001). *Radar interferometry: Data interpretation and error analysis*. Kluwer Academic Publishers. <https://doi.org/10.1007/0-306-47633-9>

- Hanssen, R. F. (2015). Bodemdalingsvariabiliteit uit InSAR data. *Report for Dutch Parliament*.
- Hettema, M., Schutjens, P., Verboom, B., & Gussinklo, H. (2000). Production-induced compaction of a sandstone reservoir: The strong influence of stress path. *SPE Reservoir Evaluation & Engineering*, 3(04), 342–347.
- Hupkes, S., Adams, W., Busscher, N., & Postmes, T. (2021). *Inzicht in impact: De gevolgen van de gaswinning voor de bewoners van groningen*. Kennisplatform Leefbaar en Kansrijk Groningen.
- Iglesias, M. A., Law, K. J., & Stuart, A. M. (2013). Ensemble kalman methods for inverse problems. *Inverse Problems*, 29(4), 045001.
- Jansson, P.-E. (1998). Simulating model for soil water and heat conditions. *Avdelningsmeddelande/Sveriges lantbruksuniversitet, Institutionen för markvetenskap, Avdelningen för lantbrukets hydroteknik*.
- Jost, J. (2005). Dynamical systems: Examples of complex behaviour. <https://doi.org/10.1007/3-540-28889-9>
- Kampes, B. M. (2006). *Radar interferometry* (Vol. 12). Springer.
- Ketelaar, V. G. (2009). *Satellite radar interferometry: Subsidence monitoring techniques* (Vol. 14). Springer Science & Business Media.
- Kim, S. S., & Vossepoul, F. C. (2024). On spatially correlated observations in importance sampling methods for subsidence estimation. *Computational Geosciences*, 28(1), 91–106.
- Koster, K., Stafleu, J., & Stouthamer, E. (2018). Differential subsidence in the urbanised coastal-deltaic plain of the netherlands. *Netherlands Journal of Geosciences*, 97(4), 215–227.
- Kroon, I., Nguyen, B.-L., Fokker, Muntendam-Bos, A., & de Lange, G. (2009). Disentangling shallow and deep processes causing surface movement. *Mathematical Geosciences*, 41, 571–584.
- Kruiver, P. P., van Dedem, E., Romijn, R., de Lange, G., Korff, M., Stafleu, J., Gunnink, J. L., Rodriguez-Marek, A., Bommer, J. J., van Elk, J., et al. (2017). An integrated shear-wave velocity model for the groningen gas field, the netherlands. *Bulletin of Earthquake Engineering*, 15, 3555–3580.
- Li, T., Bolic, M., & Djuric, P. M. (2015). Resampling methods for particle filtering: Classification, implementation, and strategies. *IEEE Signal processing magazine*, 32(3), 70–86.
- Li, T., Sun, S., Sattar, T. P., & Corchado, J. M. (2014). Fight sample degeneracy and impoverishment in particle filters: A review of intelligent approaches. *Expert Systems with applications*, 41(8), 3944–3954. <https://doi.org/10.1016/j.eswa.2013.12.031>
- Luo, X., Lorentzen, R. J., Valestrand, R., & Evensen, G. (2019). Correlation-based adaptive localization for ensemble-based history matching: Applied to the norne field case study. *SPE Reservoir Evaluation & Engineering*, 22(03), 1084–1109.
- Martino, L., Elvira, V., & Louzada, F. (2017). Effective sample size for importance sampling based on discrepancy measures. *Signal Processing*, 131, 386–401. <https://doi.org/10.1016/j.sigpro.2016.08.025>
- Mijnbouwwet. (2003). *Mijnbouwwet (mining act of the netherlands)*. NLOG.

- Mindlin, R. D., & Cheng, D. H. (1950). Thermoelastic stress in the semi-infinite solid. *Journal of Applied Physics*, 21(9), 931–933.
- Morzfeld, M., Day, M. S., Grout, R. W., Heng Pau, G. S., Finsterle, S. A., & Bell, J. B. (2018). Iterative importance sampling algorithms for parameter estimation. *SIAM Journal on Scientific Computing*, 40(2), B329–B352.
- Muñoz, L. F. P., & Roehl, D. (2017). An analytical solution for displacements due to reservoir compaction under arbitrary pressure changes. *Applied Mathematical Modelling*, 52, 145–159. <https://doi.org/10.1016/j.apm.2017.06.023>
- NAM. (2016). Technical addendum to the winningsplan groningen 2016: Production, subsidence, induced earthquakes and seismic hazard and risk assessment in the groningen field. part i summary and production.
- NAM. (2017). Ensemble based subsidence application to the ameland gas field - long term subsidence study part two (Its-ii) continued study.
- NAM. (2019). Stabiliteitsanalyse van waterpaspeilmerken 2019: Toelichting methodiek en toepassing op de meetregisters “noord nederland, groningen en waddenzee 2018” en “zuid-holland 2017”. *NAM*.
- NAM. (2020). Statusrapport 2020 en prognose tot het jaar 2080: Bodemdaling door aardgaswinning, nam-gasveld in groningen, friesland en het noorden van drenthe. *NAM*.
- Nearing, G., Gupta, H. V., Crow, W. T., & Gong, W. (2013). An approach to quantifying the efficiency of a bayesian filter. *Water Resources Research*, 49(4), 2164–2173. <https://doi.org/10.1002/wrcr.20177>
- Nearing, G., Yatheendradas, S., Crow, W., Zhan, X., Liu, J., & Chen, F. (2018). The efficiency of data assimilation. *Water resources research*, 54(9), 6374–6392. <https://doi.org/10.1029/2017WR020991>
- Paninski, L. (2003). Estimation of entropy and mutual information. *Neural computation*, 15(6), 1191–1253. <https://doi.org/10.1162/089976603321780272>
- Poterjoy, J. (2016). A localized particle filter for high-dimensional nonlinear systems. *Monthly Weather Review*, 144(1), 59–76.
- Shannon, C. (1945). *A mathematical theory of cryptography*.
- Simonin, D., Waller, J. A., Ballard, S. P., Dance, S. L., & Nichols, N. K. (2019). A pragmatic strategy for implementing spatially correlated observation errors in an operational system: An application to doppler radial winds. *Quarterly Journal of the Royal Meteorological Society*, 145(723), 2772–2790. <https://doi.org/10.1002/qj.3592>
- Slivinski, L., & Snyder, C. (2016). Exploring practical estimates of the ensemble size necessary for particle filters. *Monthly Weather Review*, 144(3), 861–875. <https://doi.org/10.1175/MWR-D-14-00303.1>
- Smith, J. D., Avouac, J.-P., White, R. S., Copley, A., Gualandi, A., & Bourne, S. (2019). Reconciling the long-term relationship between reservoir pore pressure depletion and compaction in the groningen region. *Journal of Geophysical Research: Solid Earth*, 124(6), 6165–6178.
- Snyder, C. (2011). Particle filters, the “optimal” proposal and high-dimensional systems, 1–10.

- Snyder, C., Bengtsson, T., Bickel, P., & Anderson, J. (2008). Obstacles to high-dimensional particle filtering. *Monthly Weather Review*, 136(12), 4629–4640. <https://doi.org/10.1175/2008MWR2529.1>
- Snyder, C., Bengtsson, T., & Morzfeld, M. (2015). Performance bounds for particle filters using the optimal proposal. *Monthly Weather Review*, 143(11), 4750–4761.
- Stordal, A. S., & Elsheikh, A. H. (2015). Iterative ensemble smoothers in the annealed importance sampling framework. *Advances in Water Resources*, 86, 231–239. <https://doi.org/https://doi.org/10.1016/j.advwatres.2015.09.030>
- Tarantola, A. (2005). *Inverse problem theory and methods for model parameter estimation*. SIAM.
- Tempone, P., Fjær, E., & Landrø, M. (2010). Improved solution of displacements due to a compacting reservoir over a rigid basement. *Applied Mathematical Modelling*, 34(11), 3352–3362. <https://doi.org/10.1016/j.apm.2010.02.025>
- Tong, Y. L., & Tong, Y. (1990). *Fundamental properties and sampling distributions of the multivariate normal distribution*. Springer.
- van Asselen, S., Erkens, G., & de Graaf, F. (2020). Monitoring shallow subsidence in cultivated peatlands. *Proceedings of the International Association of Hydrological Sciences*, 382, 189–194.
- van Asselen, S., Erkens, G., Stouthamer, E., Woolderink, H. A., Geeraert, R. E., & Hefting, M. M. (2018). The relative contribution of peat compaction and oxidation to subsidence in built-up areas in the rhine-meuse delta, the netherlands. *Science of the Total Environment*, 636, 177–191.
- van Elk, Anke Jannie, L., & Rob, v. E. (2021). Reservoir pressure and subsidence groningen field update for production profile gts - raming 2021. *NAM*.
- van Elk, Landman, A., Visser, C., & Uilenreef, J. (2022). Study plan for induced seismicity in groningen during the pressure equilibration period. *NAM*.
- van Leeuwen, P. J. (2003). A variance-minimizing filter for large-scale applications. *Monthly Weather Review*, 131(9), 2071–2084. [https://doi.org/10.1175/1520-0493\(2003\)131<2071:AVFFLA>2.0.CO;2](https://doi.org/10.1175/1520-0493(2003)131<2071:AVFFLA>2.0.CO;2)
- van Leeuwen, P. J. (2009). Particle filtering in geophysical systems. *Monthly Weather Review*, 137(12), 4089–4114. <https://doi.org/10.1175/2009MWR2835.1>
- van Leeuwen, P. J. (2010). Nonlinear data assimilation in geosciences: An extremely efficient particle filter. *Quarterly Journal of the Royal Meteorological Society*, 136(653), 1991–1999.
- van Leeuwen, P. J., & Ades, M. (2013). Efficient fully nonlinear data assimilation for geophysical fluid dynamics. *Computers & Geosciences*, 55, 16–27.
- van Leeuwen, P. J., Cheng, Y., & Reich, S. (2015). *Nonlinear data assimilation for high-dimensional systems: -with geophysical applications*. Springer.
- van Leeuwen, P. J., Künsch, H. R., Nerger, L., Potthast, R., & Reich, S. (2019). Particle filters for high-dimensional geoscience applications: A review. *Quarterly Journal of the Royal Meteorological Society*, 145(723), 2335–2365. <https://doi.org/10.1002/qj.3551>
- van Thienen-Visser, K., & Fokker, P. (2017). The future of subsidence modelling: Compaction and subsidence due to gas depletion of the groningen gas field in the netherlands. *Netherlands Journal of Geosciences*, 96(5), s105–s116.

- Vossepoel, F. C., & van Leeuwen, P. J. (2007). Parameter estimation using a particle method: Inferring mixing coefficients from sea level observations. *Monthly weather review*, *135*(3), 1006–1020. <https://doi.org/doi.org/10.1175/MWR3328.1>
- Wikle, C. K., & Berliner, L. M. (2007). A bayesian tutorial for data assimilation. *Physica D: Nonlinear Phenomena*, *230*(1-2), 1–16. <https://doi.org/10.1016/j.physd.2006.09.017>
- Yustres, Á., Asensio, L., Alonso, J., & Navarro, V. (2012). A review of markov chain monte carlo and information theory tools for inverse problems in subsurface flow. *Computational Geosciences*, *16*(1), 1–20. <https://doi.org/10.1007/s10596-011-9249-z>
- Zoccarato, C., Baù, D., Ferronato, M., Gambolati, G., Alzraiee, A., & Teatini, P. (2016). Data assimilation of surface displacements to improve geomechanical parameters of gas storage reservoirs. *Journal of Geophysical Research: Solid Earth*, *121*(3), 1441–1461. <https://doi.org/10.1002/2015JB012090>

ACKNOWLEDGEMENTS

Completing a doctorate is a journey that brings personal and intellectual growth. During this journey, I met more people than I could thank; you all brought me great joy, knowledge, help, and motivation, and you also knew how to challenge me to bring out the best in me.

Thank you for unconditionally being with me despite the distance;

Thank you for always believing in me and finding the right words in any situation;

Thank you for brightening up my daily routine;

Thank you for your kindness and friendship.

CURRICULUM VITÆ

Samantha S.R. KIM

25-02-1992 Born in Nancy, France.

EDUCATION

2010–2013 Bachelor of Science in Physics and Engineering
UFR de physique, Strasbourg

2013–2015 Master of Science in Condensed Matter Physics
UFR de physique, Strasbourg

2016–2017 Master in Educational Science
University of Lorraine, Nancy-Metz

2018–2019 Master of Science in Earth Physics
School and Observatory of Earth Sciences (EOST), Strasbourg-Uppsala

2019–2024 PhD. Geosciences
Technische Universiteit Delft

Thesis: DATA ASSIMILATION FOR SUBSIDENCE ANALYSIS OF
 THE GRONINGEN REGION: A MULTI-SCALE STUDY
 WITH IMPORTANCE SAMPLING

Promotor: Prof. dr. ir. F.C. Vossepoel

Promotor: Prof. dr. ir. R.F. Hanssen

LIST OF PUBLICATIONS

JOURNALS

1. **S. S.R. Kim**, F. C. Vossepoel (2023) *On spatially correlated observations in importance sampling methods for subsidence estimation*, Computational Geosciences, 28(1), 91-106, <https://doi.org/10.1007/s10596-023-10264-9>.

CONFERENCES

5. **S. S.R. Kim**, F. C. Vossepoel, R. F. Hanssen, M. Wouters, R. Govers, E. Stouthamer *A particle method strategy to estimate subsidence induced by a high-dimensional disc-strain model for reservoir compaction*, EGU-22117 EGU (2020), Vienna.
4. **S. S.R. Kim**, F. C. Vossepoel, R. F. Hanssen *Exploring high-dimensional applicability of the particle filter in increasingly complex systems – a case study for compacting reservoir and subsidence*, agu-fm20-745128-9781-4672-6454-3099 AGU (2020).
3. **S. S.R. Kim**, R. F. Hanssen, F. C. Vossepoel *On the applicability of a particle method in models of increasing complexity: a case study for modeling subsidence*, agu-fm21-978743-3347-8849-8044-7730 AGU (2021), New Orleans.
2. **S. S.R. Kim**, W. S. Brouwer, R. F. Hanssen, F. C. Vossepoel *Optimizing the use of InSAR observations in data assimilation problems to estimate reservoir*, EGU22-11879 EGU (2022), Vienna.
1. **S. S.R. Kim**, W. S. Brouwer, R. F. Hanssen, F. C. Vossepoel *On the use of InSAR observations for drivers of subsidence estimation: an application to compacting reservoirs*, TISOLS (2023), Delft.

FUNDING

This project is funded by NWO project DEEP.NL.2018.052, “Monitoring and Modelling the Groningen Subsurface based on integrated Geodesy and Geophysics: improving the space-time dimension”.